Transmission Electron Microscopy Study on Local Structural Transformations by Interatomic Interaction in Layered Materials

Na Yeon Kim

Department of Materials Science and Engineering

Graduate School of UNIST

2019

Transmission Electron Microscopy Study on Local Structural Transformations by Interatomic Interaction in Layered Materials

Na Yeon Kim

Department of Materials Science and Engineering
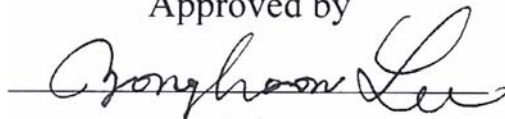
Graduate School of UNIST

Transmission Electron Microscopy Study on Local Structural Transformations by Interatomic Interaction in Layered Materials

A thesis/dissertation

submitted to the Graduate School of UNIST

in partial fulfillment of the

requirements for the degree of

Doctor of Philosophy

Na Yeon Kim

12.10.2018 of submission

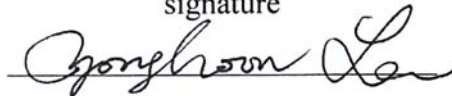Approved by

_____

Advisor

Zonghoon Lee

Transmission Electron Microscopy Study on Local Structural Transformations by Interatomic Interaction in Layered Materials

Na Yeon Kim

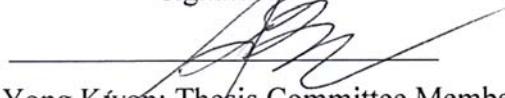This certifies that the thesis/dissertation of Na Yeon Kim is approved.
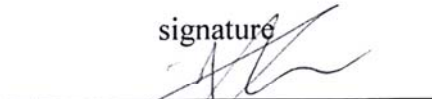
12/10/2018

signature

Advisor: Zonghoon Lee

signature

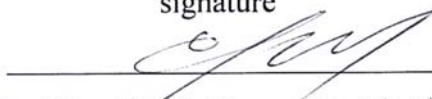Soon-Yong Kwon: Thesis Committee Member #1

signature

Jung-Woo Yoo: Thesis Committee Member #2

signature

Hyung-Joon Shin: Thesis Committee Member #3

signature

Eui-Tae Kim: Thesis Committee Member #4;

Abstracts

Structural transformation in materials has a potential to surpass materials' intrinsic properties and gives rise to peculiar properties by doping, functionalization, heat treatment and so on. The material assembled into layered architectures is susceptible to interaction with other elements owing to weak van der Waals interaction between the layers. In addition, it is superior in an investigation on localized structural variations caused by interactions with other elements in not only two-dimensional and but bulk materials. Although the structural transformation could have a huge impact on materials' properties, in general, it occurs just in few micro-regions, which makes it difficult to do characterization accurately with analysis tools.

Transmission electron microscopy (TEM) is indispensable for materials science, in particular, nanotechnology research. Dark-field TEM (DF-TEM) specializes in the structural transformation because it allows the area of specimen out of the Bragg condition only to light up like dislocations and bending regions in single crystal specimens. Development of aberration-corrected TEM with monochromator enables us to image single atoms in two-dimensional materials and atomic columns in bulk materials and, by extension, to determine the structural transformation such as lattice distortion and interatomic exchange interaction. The structural transformation accompanies a change in chemical state, which can be also explored by spectroscopic analysis of electron energy loss spectroscopy (EELS) in TEM.

This thesis aims to deeply understand the structural transformation in layered materials: carbon-based low dimensional materials and layered cathode materials in lithium-ion batteries, using several TEM analysis techniques such as DF-TEM, atomic-resolution TEM (AR-TEM) and EELS. DF-TEM analysis was extensively carried out to reveal the structural evolution in carbon-based low dimensional materials during a subsequent heat treatment process and local lattice relaxation of graphene/hBN superstructure. It was also applied to cycling – induced local phase transformation at the outermost areas of cathode materials in lithium-ion battery. The local structural transformation was successfully determined by AR-TEM and high-resolution scanning TEM imaging analyses in combination with image simulation. A comprehensive EELS study, conducted in a wide range of energy losses of carbon and transition metals, was able to reveal changes of chemical states caused by the structural transformation. Therefore, the present study provides a framework for the fundamental understanding of structural and chemical transformation in a wide range of layered materials through TEM analysis. It also provides insight into an intimate correlation between structural transformation and materials' peculiar properties.

CONTENTS

PART 2. DEGRADATION MECHANISM OF LAYERED CATHODE MATERIALS IN LITHIUM ION BATTERIES

Chapter 4: Cycling-Induced Microstructural Degradation on Cathode Materials

Chapter 5: Reaction Between Electrode Materials and Electrolytes

Chapter 6: Concluding Remarks

CURRICULUM VITAE

REFERENCES

LISTS OF FIGURES

Chapter 1: Introduction

1.1| Overview

Developing precise control over a composition in materials has attracted considerable attention in modern technology. An investigation on microstructural properties is a prerequisite to find out the origins of unusual physical properties, and thereby making it possible to engineer the materials' properties.

This thesis provides two main research topics that require deeper understanding of structural properties in layered materials with an introduction part containing a brief review of the layered materials, transmission electron microscopy and scanning transmission electron microscopy (TEM/STEM) and my research objectives; Part 1 for low-dimensional materials of carbon-based materials and two-dimensional (2D) heterostructures of graphene on hBN and Part 2 for researches on the microstructural degradation of nickel-rich layered cathode materials in lithium-ion batteries.

The introduction part contains my research backgrounds and research objectives, how to study the structural transformation. Part 1 provides studies aimed to explore the transformation on lattice and stacking structures of low-dimensional materials such as pristine graphene, graphene oxide and multilayer-graphene-stacked system, moreover, 2D superstructures of artificially stacked bilayer graphene and heterostructure of graphene on hBN. Annealing at the high temperature over 2500 ℃ improves texturizing into well-ordered hexagonal lattices and decreasing interlayer distances by removing functional groups attached on carbon precursors and trapped things between layers. The changed chemical states by the structural transformation is investigated by electron energy loss spectroscopy (EELS). Moreover, dark-field TEM (DF-TEM) imaging analysis in 2D heterostructure reveals interlayer relation such as twist angle and superlattice domains, moreover, the local structural transformation at specific orientation. Those studies in low-dimensional materials provide direct evidences of a relation between structures and their peculiar properties and shed light on an importance of TEM analysis on the understanding of structural transformation.

Part 2 provides studies on the microstructural degradation induced by repeated electrochemical cycling in company with a side reaction with electrolytes. Electrochemical performance of lithium-ion batteries is associated with structural and chemical stability of electrode materials. However, inevitable lattice distortions and chemical evolution have not been investigated intensively. I report the structural evolution localized in the outermost regions of cathode materials through electron diffraction and high-resolution imaging analyses with aberration-corrected TEM/STEM. Repetition of volumetric changes generates cracks and voids, which is associated with deterioration of electrochemical performance. The

structural change is closely related to (003) intensity in electron diffraction, and it can be presented by DF-TEM imaging at a glance. EELS analysis elucidates the structural evolution accompanying chemical modification. Moreover, additive types in electrolytes make a difference in cycling-induced morphological change of cathode materials. Those studies provide an insight into correlating the structural and chemical evolution with the degradation mechanism on battery performances of $LiNi_xCo_yMn_{1-x-y}O_2$ cathode materials.

1.2| Layered Materials: A Brief Review

Layered materials are composed of inherently two-dimensional layers of atoms such as graphene with interplanar forces of van der Waals interaction or assembled into layered architectures by processes.[1, 2] They are generally classified into three groups depending on the composition and the forces to hold the layers together. (**Figure 1**) The first type of layered materials is composed of atomically thin layers with weak van der Waals interaction such as graphite and hexagonal boron nitride. Recently, it has been attracted intensely after separated as an individual layer by mechanical exfoliation and it leads to a new research field in two-dimensional materials. The second one has layers composed of two or three distinct planes of strongly bonded atoms held together by van der Waals interaction such as transition metal dichalcogenides (MoS_2, $MoSe_2$, WS_2, WSe_2, WTe_2, etc.) and lithium transition metal oxides ($LiCoO_2$). The third one has layers made up of dense assemblies of strongly bonded atoms with van der Waals interaction and/or electrostatic interactions such as silicate clays and layer double hydroxides.

The layered materials compacted by weak van der Waals interaction are susceptible to the structural transformation through interaction with other elements and separation into individual sheets by intercalation and mechanical exfoliation.
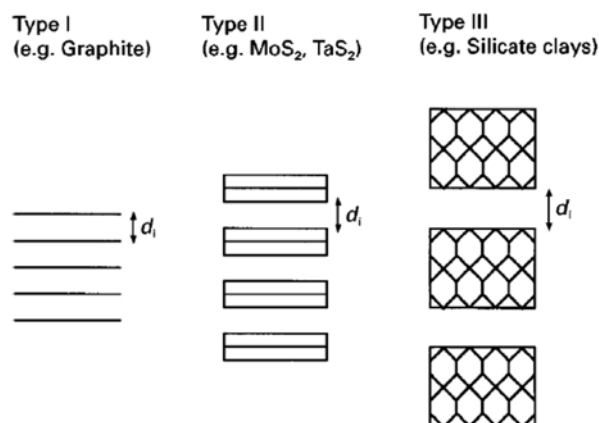
Figure 1. A schematic classification of layered materials. (d_i = interlayer distance)[1]

2

1.3| Advanced Aberration-corrected TEM/STEM: A Brief Review

Rising desire to manipulate the materials' properties at the level of single atoms needs to qualify and quantify the materials with imaging analysis at atomic resolution. As shown in **Figure 2(a)**, the wavelength of electrons needs to be decreased to improve the resolution by increasing the accelerating voltage of microscopes up to 1 MeV or higher.[3] The increased voltage also increases the penetration depth of electrons and it enables to analyze much thicker specimens. Nowadays, with the increased interest in beam-sensitive nanostructured materials, the tendency is towards lower voltages to reduce the electron irradiation damage. Recent advances in the control of lens aberrations through the successful development of multipole-based aberration correctors open a new level of sub-Å resolution and rapid, atomic-resolution compositional imaging even at low acceleration voltages up to 30 keV.[4]
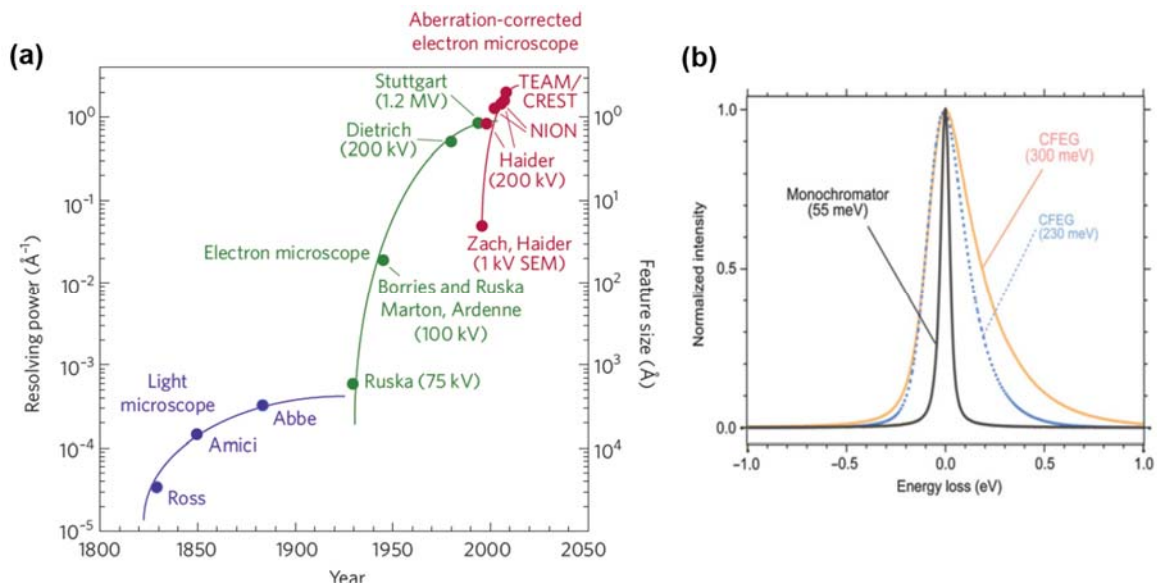
Figure 2. Advances of spatial resolution in imaging microscopies and enhancement of energy resolution in EELS by development of monochromator.[4, 5]

The energy resolution depends on an aberration of the electron spectrometer, energy distribution, and collection angle. The energy spread of incident electrons should be narrower than the natural Fermi edge of a specimen to reveal the energy-loss near-edge structure of the specimen. For a study on such features in *low loss* as vibrational modes, inter/intra band excitation, the tunneling tail of the *zero loss* is problematic in the observation of the fine structure and it is necessary to attain better energy resolution. Development of the monochromators with aberration correctors decreases the full width at half maximum (FWHM) significantly below 100 meV (**Figure 2(b)**), which enables to detect a motion of the weakly bound conduction and valence-band electrons.

1.3.1| Electron Diffraction & Dark Field TEM
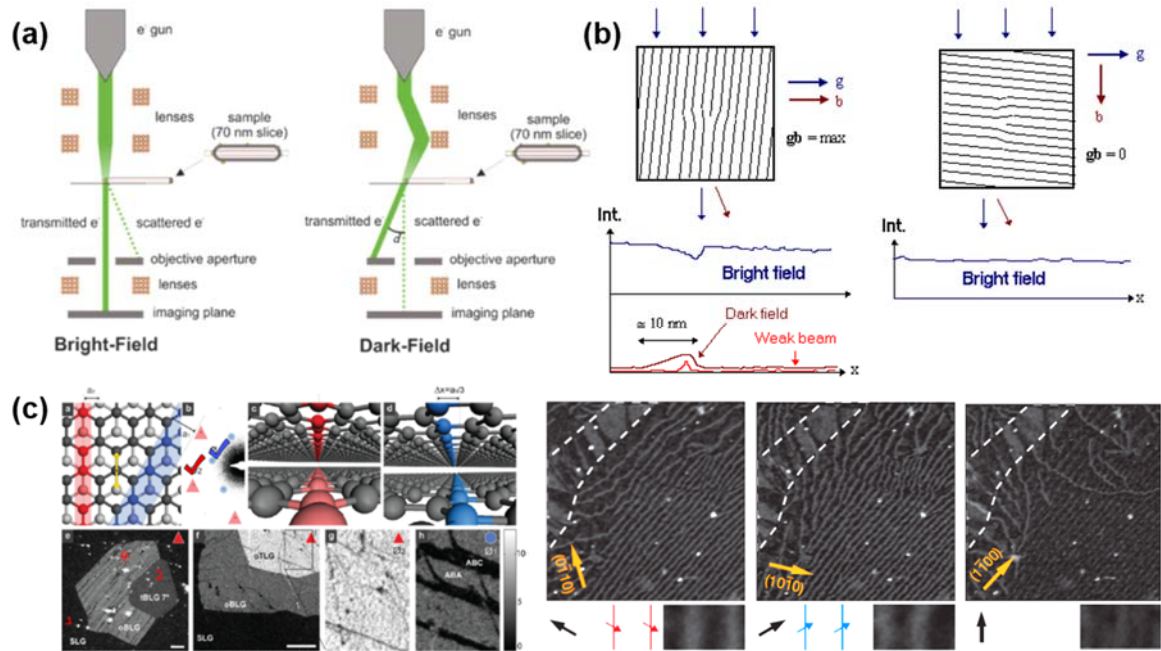
Figure 3. (a) Ray diagrams of bright-field and dark-field imaging mode. (b) Contrast of dislocation in dark-field TEM. (c) Applications of dark-field TEM imaging in 2D materials.[6-8]

DF-TEM imaging involves the diffracted beam from the specimen by placing an objective lens aperture on the back focal plane, so it displays structure information only at the selected diffraction. The ray diagrams (**Figure 3**) display how to be imaged by the diffracted beam and comparison between bright-field TEM imaging. It allows only selected diffraction to light up in single crystal specimens. This is appropriate for the microstructure of epitaxial growth materials and defect analysis such as dislocation and grain boundaries.[9] If Burgers vector for dislocation is aligned along the same orientation with diffraction vector, it looks much brighter in DF-TEM (**Figure 3(b)**). Recently, as growing the interest in the research of 2D materials, DF-TEM has been attracted to distinguish the stacking configuration and dislocation. It is difficult to determine the stacking configuration clearly with atomic resolution image and another characterization tools like Raman spectroscopy and X-ray diffraction. The change in stacking configuration makes phase shift and generates contrast difference in DF-TEM. Therefore, DF-TEM analysis is effectively applied to investigate the defect analysis not only to bulk materials, but also 2D materials.

1.3.2| Atomic Resolution TEM/STEM Imaging

High-resolution TEM (HR-TEM) is an important aspect of microstructure analysis. Phase contrast, which is a primary factor on the HR-TEM image, arises due to the difference in phase of the electron waves by interaction with a thin specimen. Two or more electron beams are incorporated, so there are many factors on the contrast mechanism; thickness, orientation, scattering factor, variations in the focus, and astigmatism of the lens.

The resolution in TEM is simply expressed as $d = AC_s^{1/4}\lambda^{3/4}$ where Cs is the spherical aberration coefficient of the objective lens, λ is the electron wavelength, and the constant A. Although an accelerating voltage has increased up to 2 MeV to decrease λ, an image resolution has been restricted by the unavoidable spherical aberration of the objective lens, which makes additional phase shifts in the back focal plane.[10] The recent development in aberration-correctors enables to observe single atoms even at the low accelerating voltage below 80 kV.
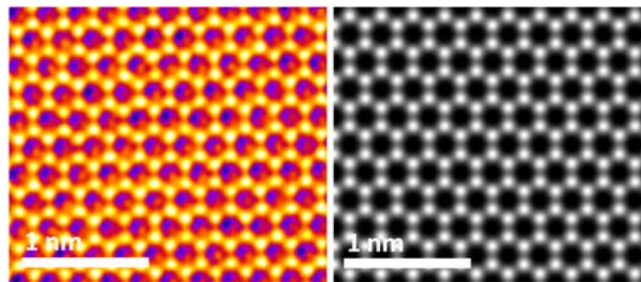
Figure 4. Experimental and simulated AR-TEM images of graphene.

Figure 4 well matches with simulated one by representing clearly resolved single carbon atoms in graphene. The contrast is so sensitive to various factors that it is necessary to conduct HR-TEM image simulation to understand and interpret the contrast in the experimental image.

1.3.3| Electron Energy Loss Spectroscopy (EELS)

EELS is to analyze the energy distribution after the incident electrons interact with the ground state of each nucleus and undergo characteristic scattering as a result of Coulomb interaction with atomic nuclei (elastic scattering) and the atomic electrons surrounding each nucleus (inelastic scattering).[11] The characteristic energy loss provides a tremendous structural and chemical information on constituent atoms such as bonding and valence states, dielectric constants, plasmonic response, the bandgap, electron density, etc. EELS spectrum is divided as *low loss* with plasmon (< 50 eV) and *core loss* (inner-shell ionization) region (> 50 eV) with the most intensive *zero loss* or elastic peak (**Figure 5**). The *zero-*

loss peak includes electrons transmitted with no measurable energy loss and those with local vibration as phonon mode. It is hard to resolve the spectrum close to *zero loss*, so it is used to specify energy resolution through its FWHM. The *low loss* EELS spectrum contains information from the weakly bound conduction and valence-band electrons. The weakly bound electrons are important because it enable us to modify electronic properties of the specimen. A plasmon is a longitudinal wave-like oscillation of 'free' electrons in the range from 5 to 30 eV.[12] Plasmon peaks are generally broad, with no specific ionization edges for element-characteristic features, so it has been used to determine the thickness of specimen and detect changes in composition with small energy shifts.[13] The *core loss* EELS spectrum results from Inner-shell electron excitation and provides ionization edges for elemental information such as bonding states and atomic composition. The characteristic edge shapes and intensities enable qualitative and quantitative analysis. In particular, fine edge structure are electronic fingerprints on coordination and density of states; energy-loss near-edge structure (ELNES) and extended energy-loss fine structure (EXELFS) (**Figure 6**). ELNES arises from the no escaped excited electrons residing in any of the empty electronic states above the Fermi level, which provides information on the local bonding configuration.
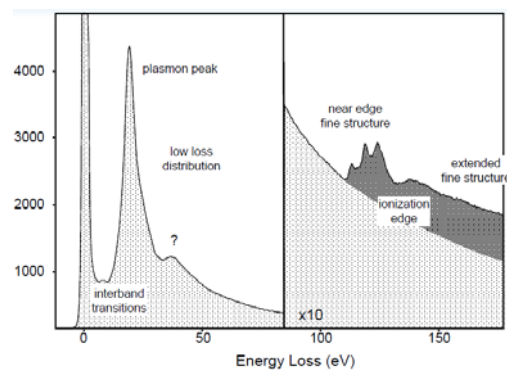
Figure 5. Electron energy loss spectrometry (EELS) spectrum.[14]
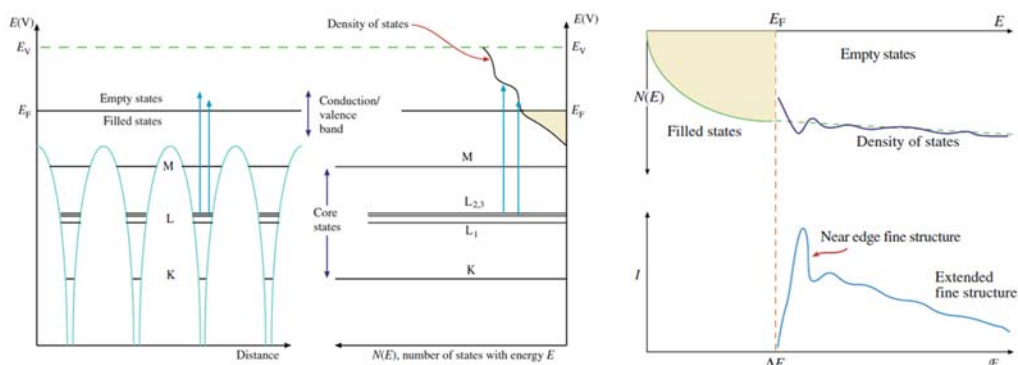
Figure 6. Energy diagram and a schematic of a relation between density of states and energy-loss near-edge structure (ELNES). [14]

6

1.4| Research Objectives

Recent development of TEM instruments has facilitated the investigation on structural transformation of low-dimensional materials, even by single-atom manipulation through AR-TEM imaging with single atom spectroscopy. Two dimensional materials are great specimen to interpret AR-TEM image and EELS because few scattering occurs to develop an image and a spectrum. If the plural scattering is significant, there are so many factors affecting on the interference between e-beam for imaging. The EELS spectrum also becomes more and more difficult to interpret, especially for *low loss* EELS and other problems arise.

In this thesis, I have studied on DF-TEM, AR-TEM and HR-STEM imaging analyses in combination with a comprehensive EELS study. I have applied this framework on layered materials which is superior in the investigation on structural variations in not only two-dimensional and but bulk layered materials. DF-TEM analysis has been applied for a study on defects such as grain boundaries and local lattice strain. It also proves improved crystallinity using distinct stacking boundaries and the local structural transformation by interlayer and interatom interaction from two dimensional hetero layered structures to bulk layered materials in combination with simulations of the electron diffraction. AR-TEM and HR-STEM analyses are essential to investigate the local structural transformation, so they are one of the primary studies on my research.

I have studied on EELS in the range of energy loss from not only *low loss* but *core loss*. *Core loss* EELS has been studied to examine the transitions of the carbon K-edges on multilayer graphene system and transition metal L-edges on nickel-rich bulk materials because it shows significant peak shifts and change in edge shape. *Low loss* EELS study has been conducted especially low dimensional carbon materials for systematic analysis related to how to enhance stacking in structures initially composed of artificially stacked and overlapped graphene oxide flakes and also the crystallinity of such materials, depending on the temperatures and pressures they have been exposed to.

PART 1. TWO-DIMENSIONAL MATERIALS

Chapter 2: Low Dimensional Carbon Materials

Carbon is the fourth most abundant element in the universe by mass after hydrogen, helium, and oxygen. and widely applied in various industry. The carbon atom has six electrons $[1s^2 2p^4]$ – two tightly bound close to the nucleus, and the remaining four as valence electrons that incorporates covalent chemical bonds. Depending on carbon-carbon bond nature and varieties in structures and textures, the carbon materials are classified as graphite, diamond, fullerene, carbon nanotubes and so on. In graphite, two of the three 2p orbitals participate in hybridization (sp^2 orbitals). The sp^2 carbon atoms have in-plane bonds, which affects the planar structure of graphite. On the other hand, all 2p orbitals forms sp^3 orbitals with tetrahedral structure in diamond (**Figure 7**).
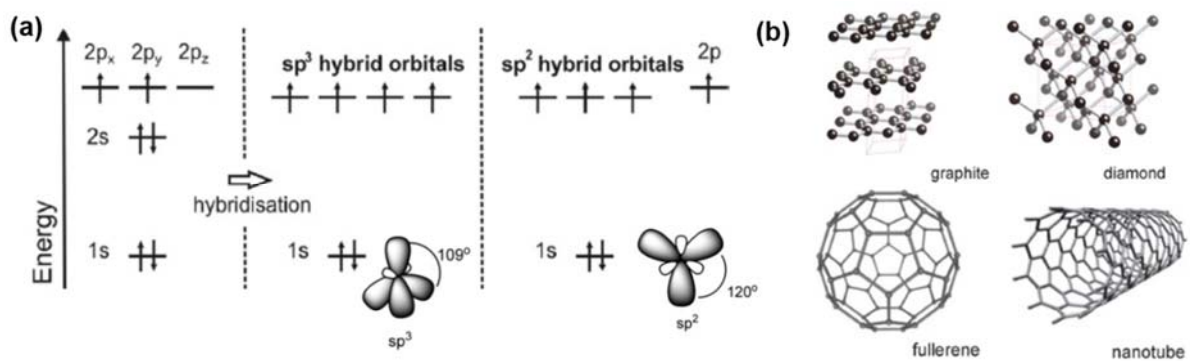
Figure 7. (a) A diagram of atomic orbitals of carbon with sp^2 and sp^3 hybrid orbitals and (b) its allotropes.[15, 16]

Among the various carbon materials, low dimensional carbon nanomaterials such as graphene, carbon nanotubes (CNTs), and fullerene (C_{60}) have been attracted as novel materials owing to their peculiar properties and an opportunity to tune them through a reaction with other elements such as hydrogen, oxygen, and fluorine. Discovery of the monolayer graphene using exfoliation and chemical vapor deposition (CVD) synthesis attracts researches on not only pure graphene but graphene-related 2D materials such as functionalized graphene and graphene oxides. In this chapter, studies on a lattice and stacking structures of graphene and structural transformation on graphene-based carbon materials by annealing under high temperature over 2500 ℃ and by chemical functionalization with hydrogen.

2.2| Graphene

2.2.1| Lattices and Stacking Structures

Graphene is the thinnest building block for graphitic materials of all dimensionalities. Its honeycomb lattice structures consist of strong σ bonds and freely moving π bonds that give extremely high electronic and thermal conductivity due to sp^2 hybridization of carbon. The unit cell of graphene is a two-dimensional rhombus with a basis of two nonequivalent carbon atoms (A and B) and a lattice parameter as 2.46 Å (**Figure 8**).

The freely moving π bonds are worth because the linear dispersion relation of π-band around K point at Fermi energy makes electrons behave as massless particles described by the Dirac equation. The electrons are so-called Dirac Fermions, which can travel through the graphene lattices with a velocity of 300 times smaller than the speed of light.[17]
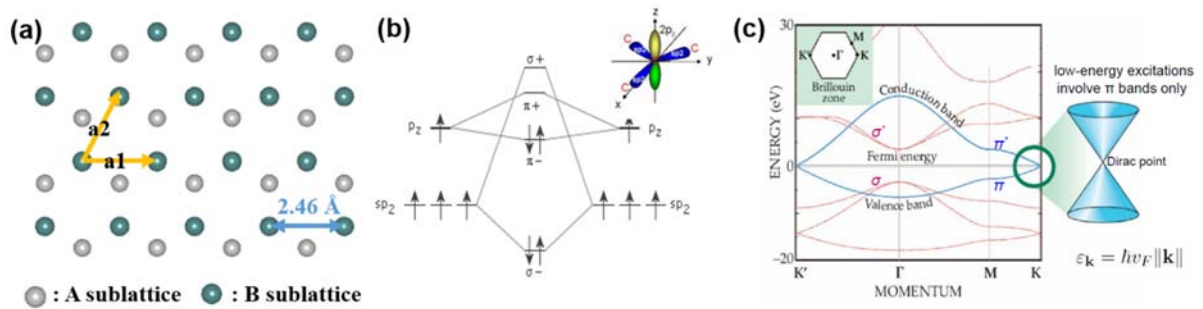
Figure 8. Structures of graphene; (a) hexagonal lattice structure (b) atomic and electronic orbitals of carbon (c) energy band structure of graphene.[18]

The most favorable stacking configuration of graphite is Bernal stacking; the upper layer (B) is stacked on the below layer (A) in the center of the hexagonal carbon lattices, in other words, it is displaced by (2/3, 1/3) along a1 and a2 axes from the first layer with ABAB stacking regularity with $P6_3$/mmc space group (**Figure 9**).

If third layer is displaced by (2/3, 1/3) from the second layer, it is not either the first layer (A) or the second layer (B), so it is denoted as another carbon layer (C). When repeating the displacement (2/3, 1/3) in the fourth layer, it coincides to the first layer (A), so the corresponding stacking structure is ABC with rhombohedral crystal system as R3m space group. It appears that the rhombohedral structure is generated by insertion of stacking fault by applying shear force, which changes diffraction pattern.

   If the second layer is stacked on the first layer at the same position, it is AA stacking. This stacking configuration is unstable energetically in nature. AA stacked graphite can appear only when Li intercalates into graphene layers of AB graphite with larger interplanar spacing about 3.53 Å. Recently, AA' stacking of graphene was reported whose interlayer distance is larger as 3.44 Å than AB stacking as 3.35 Å.[19] The (h01), (0kl) and (hkl) reflections are absent in AA' graphite, due to the insertion of additional atoms from the A' graphene layers into the eclipsed AA form.

   In addition to regular stacking configuration, random stacking is also possible, which is composed of rotated and/or translated carbon layers and called as turbostratic stacking.
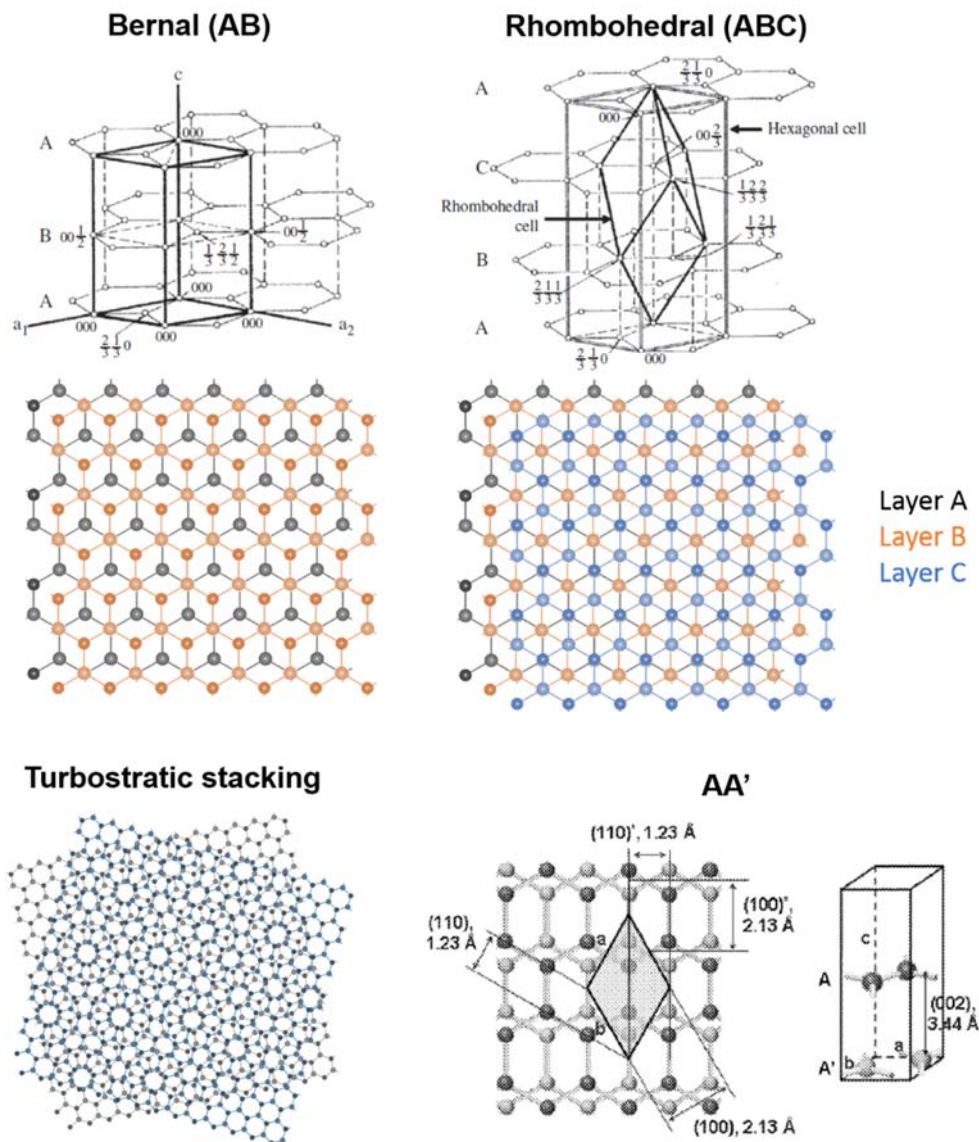
Figure 9. Stacking configurations of graphite; Bernal (AB), Rhombohedral (ABC), Turbostratic and AA' stacking.[19]

2.2.2| Synthesis and Fabrication

Graphene growth system by CVD is expected generally as three steps: decomposition and adsorption, diffusion and desorption, nucleation and growth toward graphene sheets (**Figure 10**).[20] The dissociated hydrocarbon species such as $(CH_3)_x$, $(CH_2)_x$, $(CH)_x$ or C_x diffuse on the copper surfaces as nucleation seeds, then, they incorporate into the graphene lattices. The hydrogen takes a role as an etching and a catalyst agent by removing the unstable activated carbon species to control the shape and size of the graphene grains or by forming active hydrogen atoms by reaction with copper surfaces, which makes dehydrogenation of hydrocarbon thermodynamically favorable.
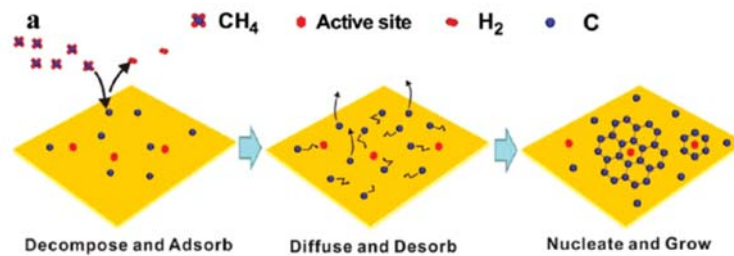
Figure 10. A schematic of growth mechanism of CVD graphene. [20]

Direct transfer method was mostly applied for fabrication for TEM analysis in my research.[21] TEM grid (Quantifoil holey carbon TEM grids (SPI Supplies, 300 mesh, 1.2 & 2-μm hole size)) is put onto the synthesized graphene on copper foil and solution (isopropyl alcohol, IPA) is dropped onto the TEM grid for better adhesion between the TEM grid and synthesized graphene on the copper foil. And then, the copper foil is etched by acid solution for 24 h. This process is appropriate for small pieces of clean graphene surfaces for TEM characterization.

2.3| Structural Transformation on Low Dimensional Carbon Materials

2.3.1| Graphitization and Carbonization

The degree of the crystallinity in carbon materials affects thermal conductivity, electrical resistivity and magnetoresistance significantly. Thermal treatment is favorable both for adjusting the degree of decomposition and towards recover the sp^2 carbon lattice. As temperature increases, carbon materials release the functional groups as gas attached on the precursor of carbon such as oxygen, nitrogen and hydrogen. When heated and annealed at 1300 ºC, almost foreign atoms go out and the carbon precursor become texturized as periodic hexagonal lattices. This is carbonization. However, the texturized carbon structure is still short-range order and they are randomly stacked. Over 2000 ºC, the carbon matrix is grown as well ordered hexagonal lattice structure and finally become perfect graphite by reducing

structural defects and enhancement of interlayer interaction with decrease in interlayer distances. This is graphitization. Their structural transformation is related with their electronic band structure, in other words, it enables us to tune the electronic properties of carbon with temperature (**Figure 11**).[22] In this chapter, I will introduce two experiments; GO for carbonization and graphitization and artificially stacked multilayer graphene just for graphitization.
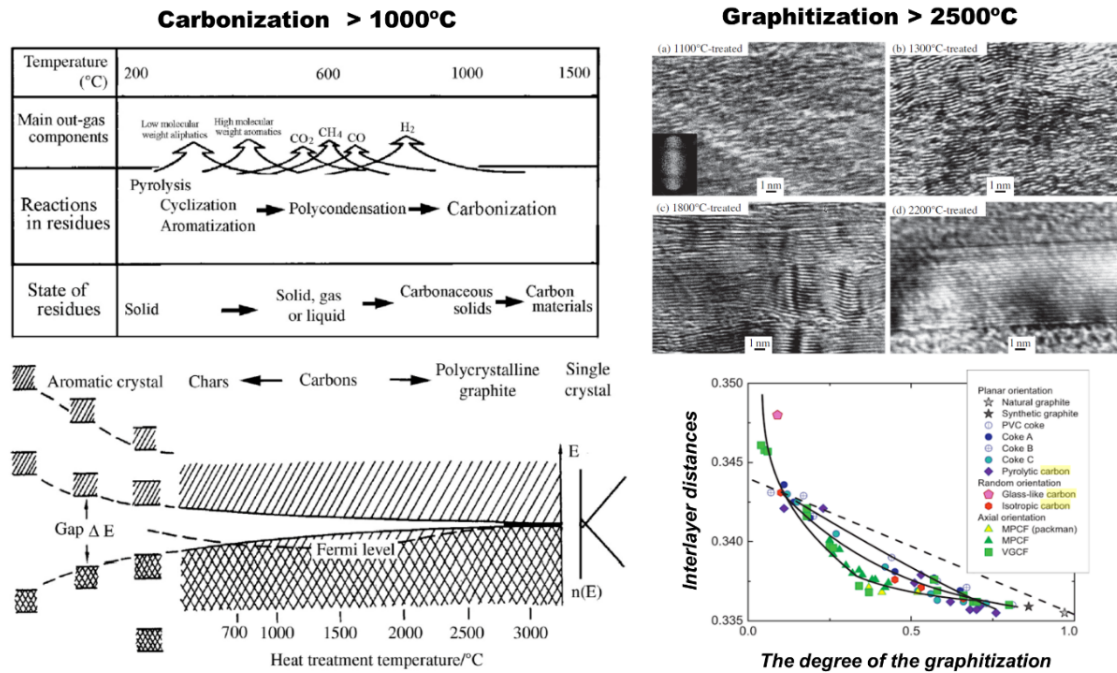
Figure 11. Carbonization and graphitization and corresponding energy band structures depending on the heat treatment temperature with interlayer distances.[23]

2.3.1.1| Graphene Oxide

Graphite foils are lightweight, flexible, chemically inert, high-temperature resistant, and highly electrically and thermally conductive. Thermally transforming graphene oxide films are desirable to maintain a densely packed film structure at high heating rates as well as to lower the decomposition and graphitizing temperatures. This work provides a discussion of the pressure-assisted thermal decomposition of graphene oxide films by hot pressing at different temperatures. The pressed films were subsequently heated at 2750 ºC to achieve a higher degree of graphitization. The combination of heating and pressing promotes the simultaneous carbonization by thermal decomposition and graphitization of GO films by reorganizing stacking configuration. Comprehensive TEM analysis with EELS demonstrates a controllable transformation of GO from random stacked and oriented GO to AB stacked multilayer graphene.[24]
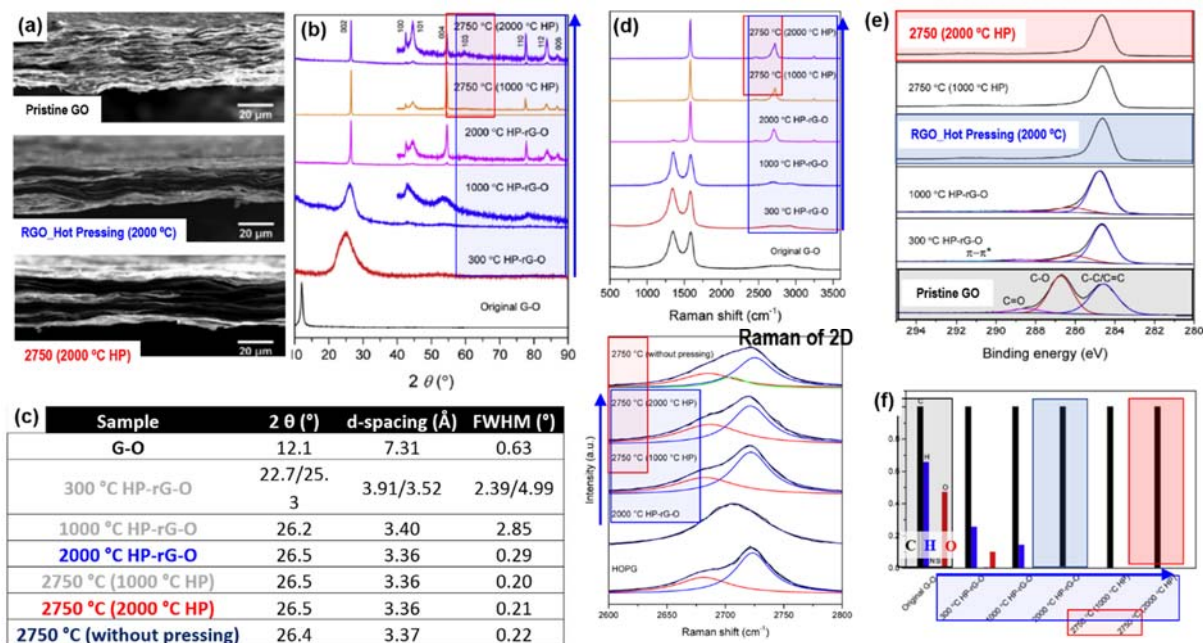
Figure 12. Improvement of the structure ordering in GO as increasing the temperature of hot pressing with further annealing. (a) Cross-sectional SEM images of the pristine GO, reduced GO by hot pressing under 2000 ºC with or without subsequent annealing at 2750 ºC. (b), (c) XRD patterns and corresponding results of (002) reflections. (d) Raman spectra. (e) XPS spectra from the C1s regions. (f) The molar ratios of C, H, and O. The blue and red box indicates an increase in temperature of hot pressing, and annealing at 2750 'C, respectively.[24]

Figure 12 represent the improvement of the structure ordering in GO depending on the temperature of hot pressing and annealing. As increasing the temperature of hot pressing, the pressed GO films appears to be compact in the cross-section SEM images. The XRD patterns present increase in intensity and decrease in FWHM of (002) and (101) reflections, which indicates transformation to AB-stacking order with hot pressing. The Raman spectra in the 2D peak are close to HOPG's spectrum. The XPS and mass fraction results indicate that this structural transition is associated with the removal of intercalated water and oxygen-containing functional groups when increasing the temperature of hot pressing. But, it is hard to distinguish the effect of hot pressing from one of annealing at the high temperature (> 2000 ºC) through Raman and XRD results.
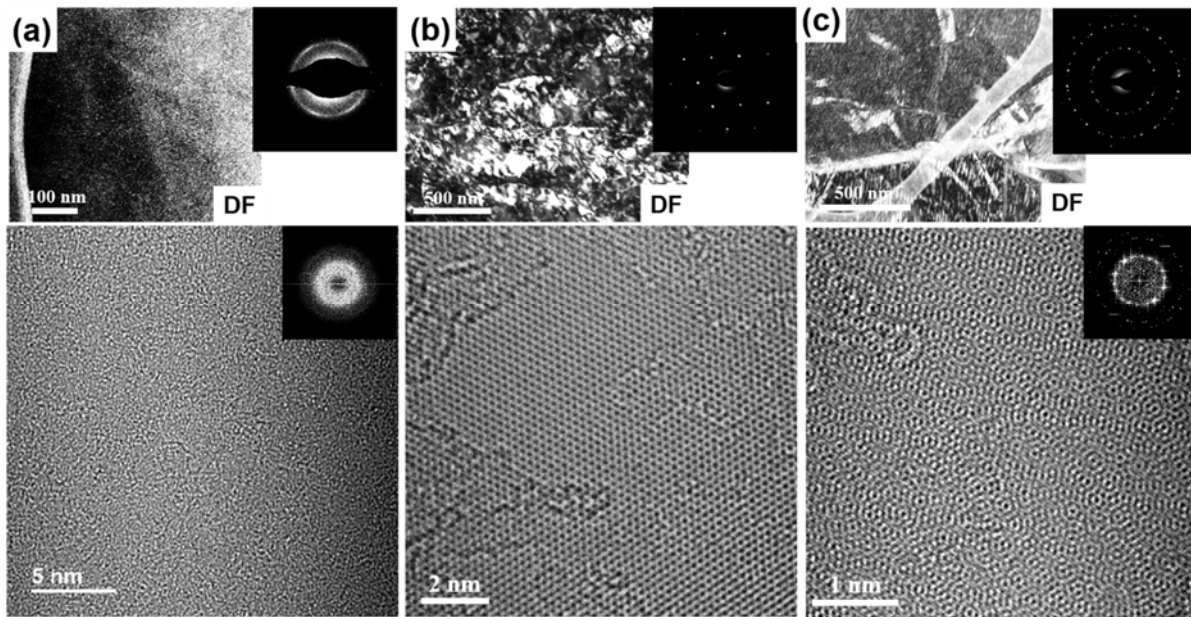
Figure 13. DF-TEM and HRTEM images of (a) GO, reduced GO (b) by hot pressing under 2000 ºC and (c) by annealing at 2750 ºC.[24]

Figure 13-14 represent DF-TEM images at the $\{10\bar{1}0\}$ diffracted spot in the diffraction mode with an objective aperture and AR-TEM images with corresponding fast Fourier transform (FFT) pattern. In the GO film (**Figure 13(a)**), there are no distinct stacking boundaries in the DF-TEM and no long-range order of hexagonal lattices in the AR-TEM with the FFT, which lets us know a highly defective and disordered structure due to random stacking of GO platelets. In the GO film hot pressed at 2000 ºC in **Figure 13(b)**, there appear short distinct lines from wrinkles, stacking boundaries and moiré fringes and one set of hexagonal $\{10\bar{1}0\}$ diffraction spots in the selected area electron diffraction (SAED) patterns indicating crystallographic ordering; this is also confirmed by the an AR-TEM image with FFT patterns where it appears that AB-stacked structure has developed in few regions. It lets us pressure-induced accelerated transformation toward graphite at relatively lower graphitization temperatures. On the other hand, the GO film annealed at 2750 ºC without pressing in **Figure 13(c)** displays random stacking from multiple sets of hexagonal SAED patterns and moiré patterns in an AR-TEM image even though well-texturized hexagonal lattices. On the other hand, the GO film annealed at 2750 ºC without pressing in **Figure 13(c)** displays random stacking from multiple sets of hexagonal SAED patterns and moiré patterns in an AR-TEM image even though well-texturized hexagonal lattices.
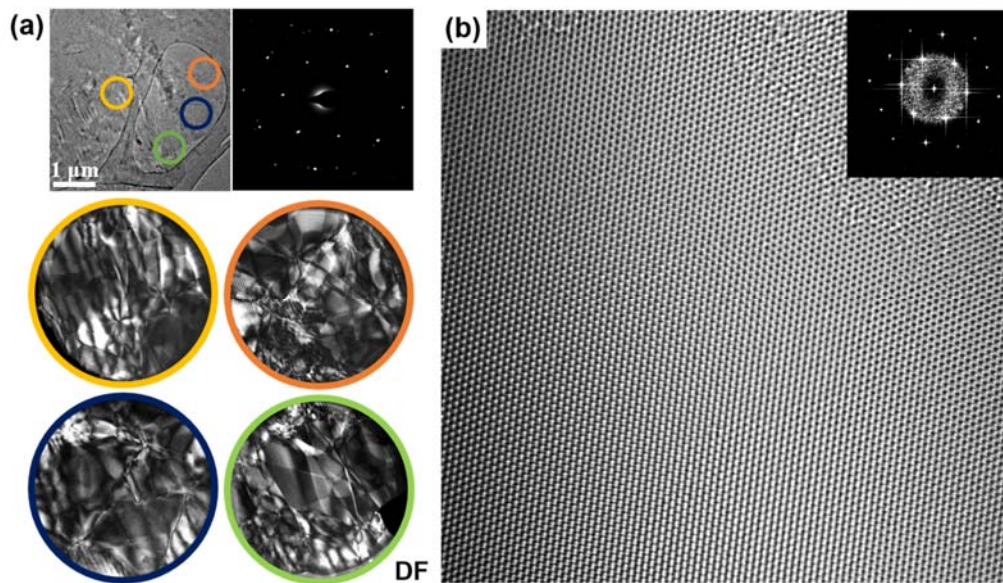
Figure 14. DF-TEM images and an ARTEM image with subsequent annealing at 2750 ºC after hot pressing at 2000 ºC on the graphene oxide film.[24]

Hot pressing of GO films at 2000 ºC followed by heating the films at 2750 ºC (**Figure 14**) significantly improves the degree of graphitization of the films, as demonstrated by the presence of only one set of $\{10\bar{1}0\}$ diffraction spots in SAED patterns at the large areas over 25 μm^2, suggesting closely perfect AB-stacked structure. DF-TEM images from different regions show a high degree of graphitization and larger areas of AB-stacking. An AR-TEM image also indicates an AB-stacked structure in multiple layers.

From the DF-TEM imaging analysis, improved crystallinity was proved by generation of distinct stacking boundaries resulting from high temperature annealing, which was because graphene oxides were converted to multilayer-graphene. High pressure lowers the graphitization temperature significantly and can substantially enhance the degree of graphitization toward AB-stacking by accelerating the kinetics of structural transformation of non-crystalline graphene domains.

2.3.1.2| Multilayer Graphene

Artificially stacked 2D materials create van der Waals structures. It has attracted great attention as the resulting properties are both unique from their individual 2D components and can create materials not found in nature. In this section, I provide structural evolution as a function of heat treatment temperature in the multilayer graphene system obtained from repeated wet transfer and artificial stacking.
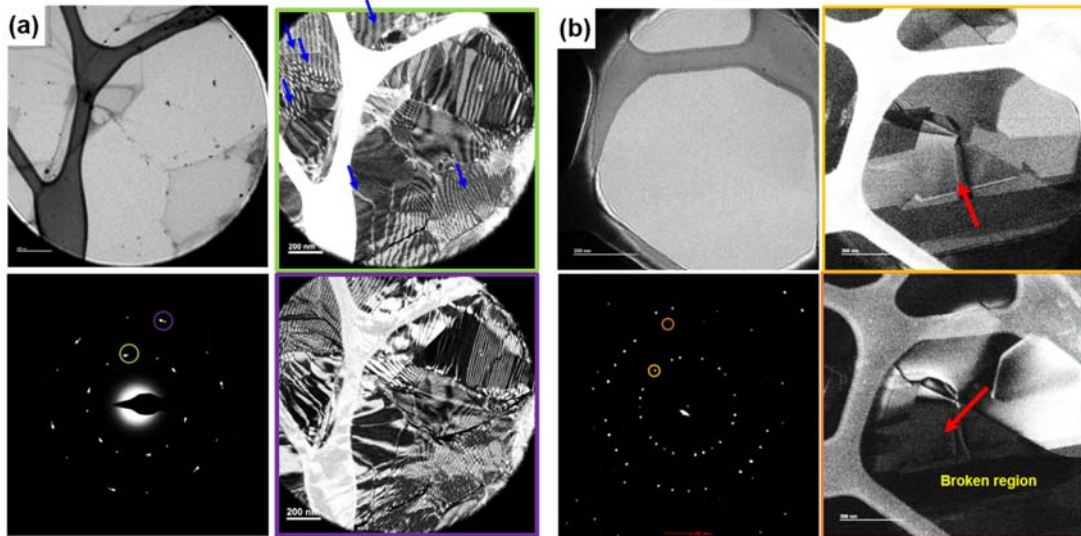
Figure 15. DF-TEM images of artificially stacked multilayer graphene (a) annealed at 400 ℃ and (b) at 2800 ℃.

5 layers of single crystal graphene deliberately stacked present multiple sets of electron diffraction patterns. The DF-TEM images at the 1st order diffracted reflections show that there are many moiré fringes with blue arrows has inevitably random stacking structure in artificial stacked multilayer graphene with trapped thing. After annealing at 2800 ℃, it appears to expand regions where the graphene layers are aligned along same orientation at the specific orientation, even though there are larger sets of the hexagonal SAED patterns due to not same specimen and different region for TEM characterization. The DF-TEM analysis is appropriate to present structural evolution toward perfect AB-stacking, on the other hand, it is hard to detect the trapped thins between the stacked layers.
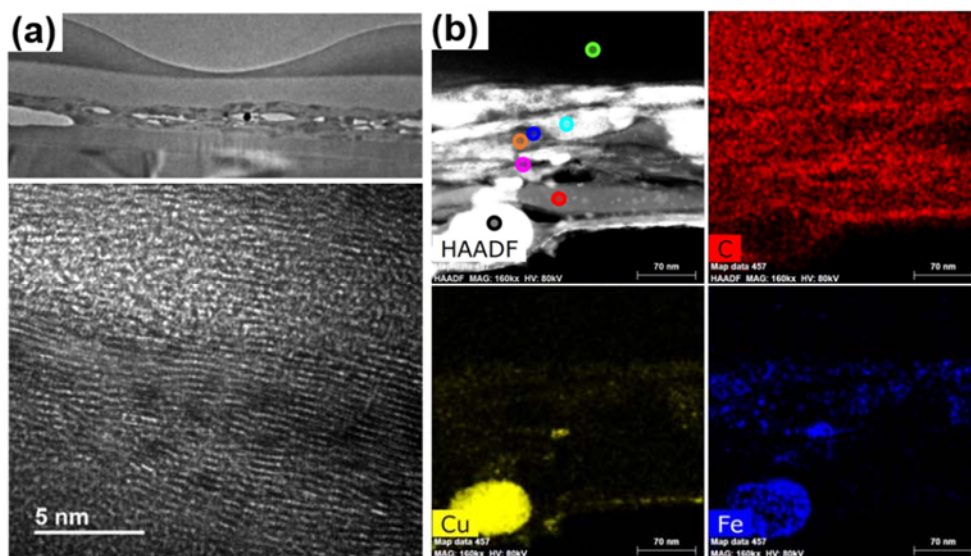
Figure 16. Characterization of the stacked graphene sample treated at 400 ℃.

The cross section TEM images of 100 layers-stacked graphene show that there are large variations of contrast due to the presence of both voids and metallic nanoparticles throughout the film in both BF and HAADF imaging (**Figure 16(a) and (b)**). The metallic particles were characterized by EDX in STEM energy dispersive X-ray images revealing them to be a mixture of Cu and Fe. They result from metal salts trapped between the layers that originated from the growth substrate and the etching solution ($FeCl_3$). From the cross-section TEM images with EDX, it is clear that the pristine stacked multilayer graphene taken by repeated wet transfer contain a lot of defects and contamination from interstitial hydrocarbon residues and metal nanoparticles. They have an effect on the larger averaged interlayer distance as 3.504 ± 0.134 Å measured from a total of 25 fringes.
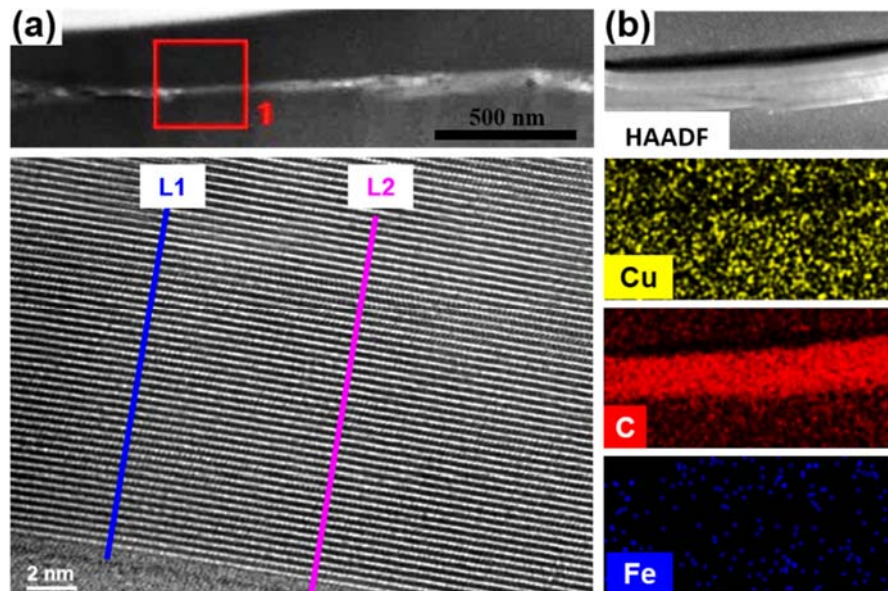
Figure 17. Characterization of the stacked graphene sample after annealed at 2800 ºC.

In an attempt to remove the contamination and basal plane defects, the SG400 film was subjected to further annealing at 2800 ºC, which is close to the temperature for perfect single crystal by graphitization. When the multilayer graphene was heated to 2800 ºC for 2 h in **Figure 17**, TEM cross section images and elemental mapping show that all the interstitial contamination and all the voids in the structure were removed, and the graphene layers were now closely stacked with a decrease in interlayer distances due to removal of trapped impurities between the layers throughout the entire cross-section. The averaged interlayer distance was 3.361 ± 0.126 Å measured from a total of 150 fringes of L1, L2 and another one. From the result, it is clear that the annealing at 2800 ºC evokes structural transformation at some regions by rearrangement and thermal decomposition to form AB stacking.

17

2.3.2| Functionalization with Hydrogen
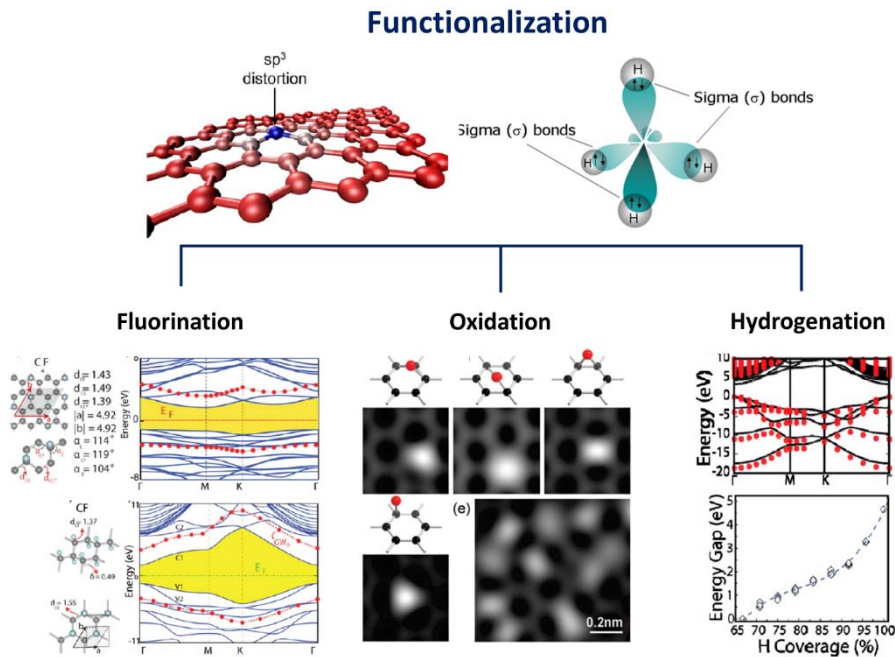
Figure 18. Chemical functionalization on graphene.[25-27]

Gr is zero band gap semiconductor. It is necessary to control and open the bandgap for wide application on device industries. Several approaches have been introduced by structural transformation such as mechanical modification and chemical modification by doping and functionalization. Research on the mechanical modification has conducted on the graphene nanoribbon[28] and nanomesh, but it is hard to control their sizes and capability on the large sized graphene sheet. On the other hand, chemical modification is widely applied by placing foreign atoms on the surface of graphene to change bonding state of the graphene from sp^2 to sp^3 hybridized bonding.[27] Hydrogen and fluorine[25, 29] are prevalent foreign atoms. If graphene is fully hydrogenated, it is called as graphane which is a predicted stoichiometric derivative of graphene.[30, 31] But it has severally compressed crystal lattice and make roughness on graphenic sheet.[32] The functionalization of graphene perturbs both its physical and chemical properties. Fully hydrogenated graphene – often referred to as graphane – is a wide band gap material according to theoretical calculations.[33, 34]
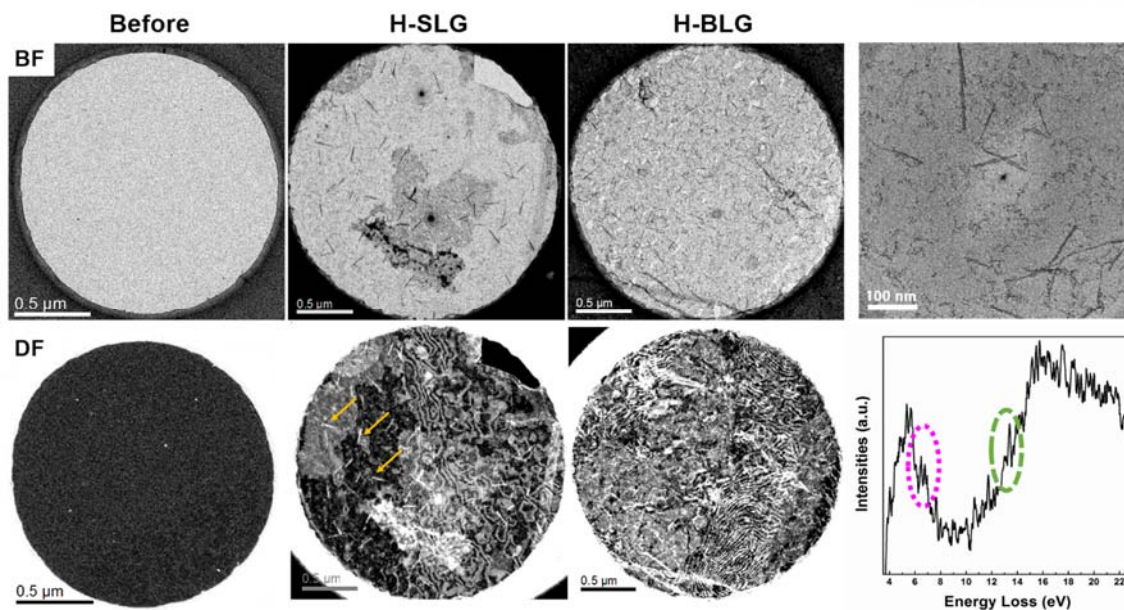
Figure 19. Hydrogenated graphene with serious roughness and wrinkles and corresponding low loss EELS spectrum.[35]

The presence of strain in hydrogenated mono- (H-SLG) and bilayer graphene (H-BLG) obtained by the Birch-type reduction of CVD-grown SLG and BLG is to be expected as the newly formed sp^3-hybridized C sites should elongate C–C bonds. The strain leads to generation of wrinkles depending on the degree of hydrogenation of graphene and also structural deformation,[36] as dark and bright field TEM analyses reveal wrinkles in H-SLG and H-BLG, whose structure is distinct with the flat and deformation-free morphology of pristine graphene. The formation of sp^3-hybridized C sites was investigated by TEM with low-loss EELS for change in the bonding states at 80 kV. Specific edges were observed at 13.4 and 7.6 eV in the EELS in H-SLG. The former signal is assigned to the ground state excitation of bonded hydrogen,[37] whereas the latter is similar in energy to that reported for unpassivated diamond surfaces, in which transformation of dangling bonds into π-bonded chains induces partial graphitization.[37] These results, combined with the observations of a π-plasmon at ~5 eV, suggest to us that some of the carbon atoms present in the product were not bonded to at least one hydrogen atom.

2.4| EELS Analysis on Change in Bonding States Induced by Structural Transformation

The structural transformation inevitably accompanies change in bonding states, which can be examined by EELS. The carbon K-edge shows a transition to perfect graphite from carbon precursor as increasing temperature through the discrete sharp edges of π* and σ* and appearance of other edges over σ* (295 ~ 310 eV), which represents the improved crystallinity.[26] (**Figure 20(a)**)
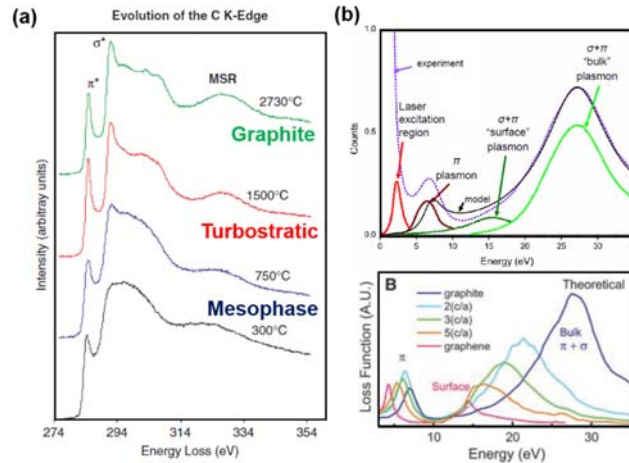
Figure 20. (a) Core loss EELS of carbon depending on structural evolution by annealing (b) Low loss EELS of graphene.[22, 42]

Low loss EELS spectrum provides information about inter- and intra-band transition, which depends on bond fraction and specimen thickness. For example, π plasmon and π+σ plasmon of graphene is at 4.7~4.9 eV and 14.7 ~ 15.4 eV, respectively.[38, 39] In the case of graphite, the π plasmon is 6~7 eV, π+σ plasmon 26 eV, which results from the increase in interlayer interactions.[40] The larger peak shift in bulk plasmon can take a role of measuring the degree of graphitic character.
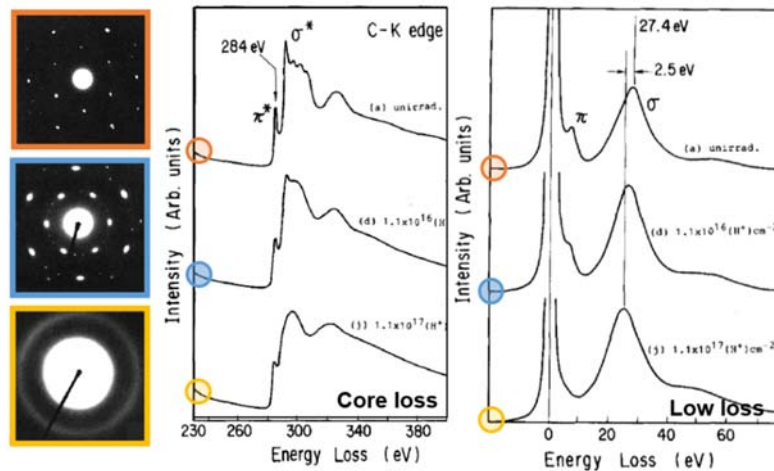
Figure 21. EELS spectra of structural disordering in graphite by hydrogen plasma treatment.[43]

20

When functionalized by hydrogen, there are a significant difference in the onset energy and intensity of π^*, σ^*, π plasmon and bulk plasmon owing to the changed C-C bond lengths and an appearance of a new edge by C-H bonds, depending on the transformed structures of hydrogenated graphene; chair, triclinic and the degree of the hydrogenation.[41]
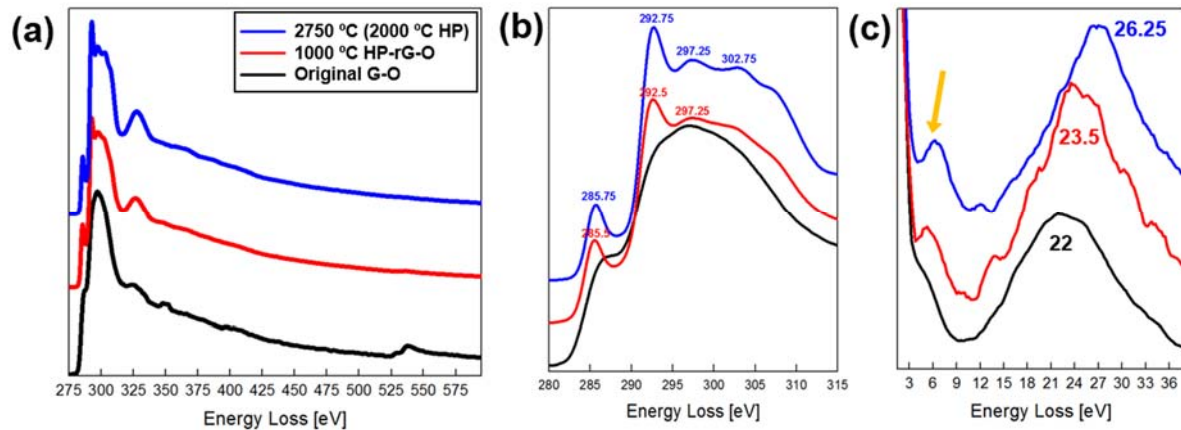
Figure 22. EELS spectra related with structural disordering in graphene oxide depending on the annealing temperature (a) (b) C-K edge (c) Low loss C region.[24]

Core-level EELS spectra of C and O K-edges were measured from the three specimens of GO film. There is a significant decrease in intensity of the O-K edge at 525 eV after annealing (**Figure 22 (a)**). It means the GO film is reduced by removing the oxygen-containing functional groups by thermal decomposition. The ELNES of the C K-edge shows considerable differences (**Figure 22 (b)**). The GO film (black) is typical of amorphous carbon judged from no fine structure of the C K-edge. For RGO film (red), the π^* and σ^* peaks are observed at 285.5 eV and 292.5 eV, respectively. Hot pressing of GO films at 2000 ºC followed by heating the films at 2750 ºC (2750 ºC (2000 ºC HP)) (blue) shows much sharper edges of π^* peak at 285.8 eV and a σ^* peak at 292.8 eV along with much sharper edge structures over the σ^* peak (~ 297, 303, and 307 eV), which was an indication of high degree of graphitization with increased stacking order. The energy difference between the π^* and σ^* peaks is 7.0 eV, which is in good agreement with the corresponding value for graphite (7.1 eV).

The low loss EELS spectra in **Figure 22(c)** indicate improved stacking in the GO film by annealing and hot pressing: The π-plasmon peak is barely visible for the GO film while it appears at 5.0 eV for RGO film and it is slightly blueshifted toward 6.0 eV for 2750 ºC (2000 ºC HP) film. The emergence of π-plasmon should indicate improved texturizing toward hexagonal lattice structures. Moreover, the peaks corresponding to the bulk plasmon in the GO film, RGO film, and 2750 ºC (2000 ºC HP) film are at 22.0 eV, 23.5 eV, and 26.25 eV, respectively.

The blue shift of the bulk-plasmon peak accompanying with the appearance of the π-plasmon peak is well consistent with the results in **Figure 21,** which is attributed to the transition from GO to highly graphitic structures by annealing and hot pressing. In addition, EELS spectra reveal the effect of hot pressing and annealing on chemical states obviously. The increase in temperature is effective to improve carbonization by promoting thermal decomposition to release oxygen functional groups, and if hot pressuring is applied, the GO films experience graphitization from incommensurate to a higher degree of compact layered stacking.
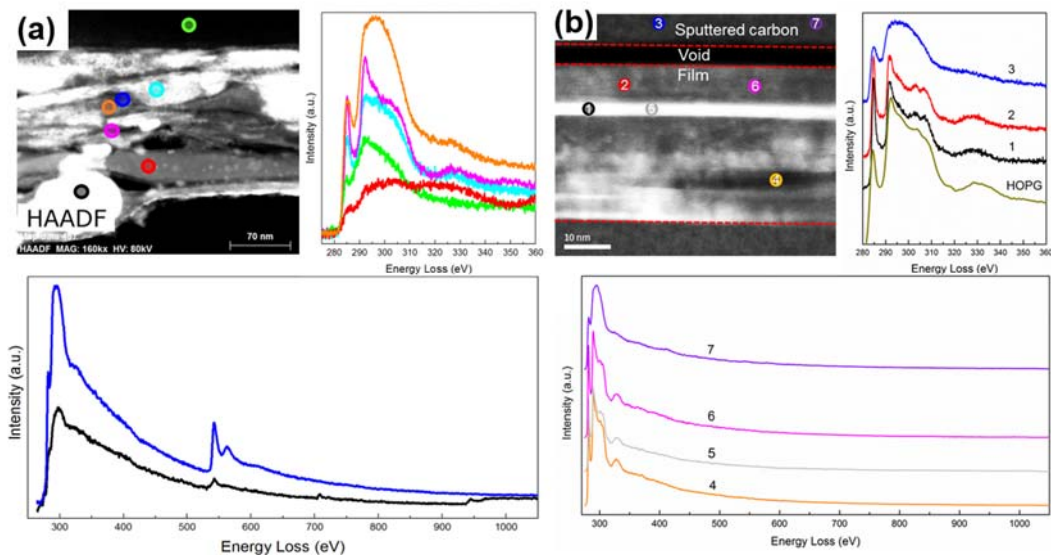
Figure 23. EELS spectra representing enhancement of the stacking in 100 layers-graphene systems annealed at (a) 400 ºC and (b) 2800 ºC.

The annealing effect only on graphitization was examined by the carbon K-edge EELS spectra taken from the cross-section TEM specimens. The multilayer graphene annealed at 400 ºC in **Figure 23(a)** shows mixed amorphous regions where there is weak split between π* and σ*(red, light blue and orange) in C-K edges and graphitic regions where discrete sharp π* and σ* edges with higher intensities (magenta and blue) with metal particles of Cu (~ 950 eV) and Fe (~ 700 eV) (black). The amorphous carbon seems to be from 'adventitious carbon' in the atmosphere adsorbing on the graphene surface rapidly after removed from the CVD reactor.

The multilayer graphene annealed at 2800 ºC shows a graphitic signature at all spectra with sharper edges over the σ* peak (~ 297, 303, and 307 eV) (**Figure 23(b)**). The carbon EELS spectra are similar to that of high-oriented pyrolytic graphite (HOPG)[44] and that of graphite, which suggests that the interstitial amorphous carbon observed in the above specimen had been clearly removed by thermal decomposition or become graphitized. The metal particle of Cu and Fe was also removed and so do O-K edge, which lets us know the specimen is only composed of well-graphitized carbon. The annealing

22

temperature of 2800 ºC exceeds the boiling points of Cu and Fe are 2567 ºC and 2750 ºC respectively, and so metal particles appear to be likely converted to small clusters and then to be driven out of the film and/or they take a role of catalyst for graphene layers to more closely stack.

2.5| Conclusion

Carbon materials reorganizes their structures depending on temperature through carbonization and graphitization, which gives an opportunity to tune the electronic band structure through changes in interlayer distances and stacking configurations. This is the reason why I have been interested in this research.

Other characterization tools do not provide an obvious difference in the degree of compact layer stacking over the high temperature (> 2000 ºC), such as XRD, XPS, and Raman spectroscopy. On the other hand, TEM clearly distinguish the effect of annealing from one of hot pressing on reorganization of GO structures at the high temperature (> 2000 ºC) through DF-TEM and AR-TEM imaging analyses; GO is transformed into polycrystalline graphite when just annealing at 2750 ºC. On the other hand, it is transformed into large-sized single-orientated graphite when pressed at 2000 ºC and subsequently annealed at 2750 ºC. In addition, the change in chemical states was obviously confirmed by discrete C K-edge and low loss carbon EELS.

Recently, we can get the single layer graphene experimentally from CVD synthesis and mechanical exfoliation. Furthermore, we can create van der Waals structures by artificial stacking of 2D materials as a synthetic crystal not found in nature. If the synthetic crystal is annealed at the high temperature (~ 2800 ºC), it is transformed into compact layered stacking by thermal decomposition of trapped things. It has partial Bernal stacking configurations from 20 to 50 %, which contrasts with general graphite. It leads to extraordinary properties such as a low sheet resistance and extremely high Young's modulus. Thus, it sheds light on new research fields of the synthetic crystals by artificial stacking.

To sum up, the heating is effective to improve carbonization and graphitization by promoting thermal decomposition from incommensurate to a higher degree of compact layered stacking, and if hot pressuring is applied, the carbon experiences further graphitization to perfect AB stacking. DF-TEM and EELS analyses determine the structural evolution obviously from incommensurate to regular compact stacking structure.

In addition, DF-TEM and EELS analyses reveal the locally transformed structures such as serious wrinkles and irregular dislocations by functionalization with hydrogen. Low loss EELS is appropriate for a study of the low degree of the functionalization and the weak C-H bonds.

Chapter 3: Interatomic Interaction on Two-Dimensional Graphene Superstructure

3.1| Introduction

The production of 2D materials has advanced in recent years, which further triggers intensive research on the van der Waals (vdW) heterostructures of 2D materials (**Figure 24**).[45] Stacked vdW heterostructure provides extraordinary properties from their individual components and different interatomic interaction between stacked layers. Replacement of SiO_2 substrates with hexagonal boron nitride (hBN) has improved the charge carrier mobility of graphene by more than 2 orders of magnitude.[46-49] The commensurate state of vdW heterostructures of 2D materials promises to overcome the inherent drawbacks of graphene on pure 2D crystals such as MoS_2 and WSe_2.[50, 51] The crystalline mismatch between the layers changes the periodicity of the superlattice, leading to a spontaneous alternation of the periodicity in each layer of 2D materials. These spontaneous changes, which arise from the van der Waals adhesion potential (according to the Frenkel–Kontorova model[52, 53]) induce interesting characteristics not observed in a multilayer superstructure.[54-58]

In this chapter, moiré superstructures are identified through DF-TEM with SAED, in particular, for a heterostructure of graphene on hBN. Analyses were performed on freestanding specimens, which was free from substrate effects. The distribution of the moiré fringes under DF-TEM immediately provides the interlayer relation through twist angle between stacked layers.
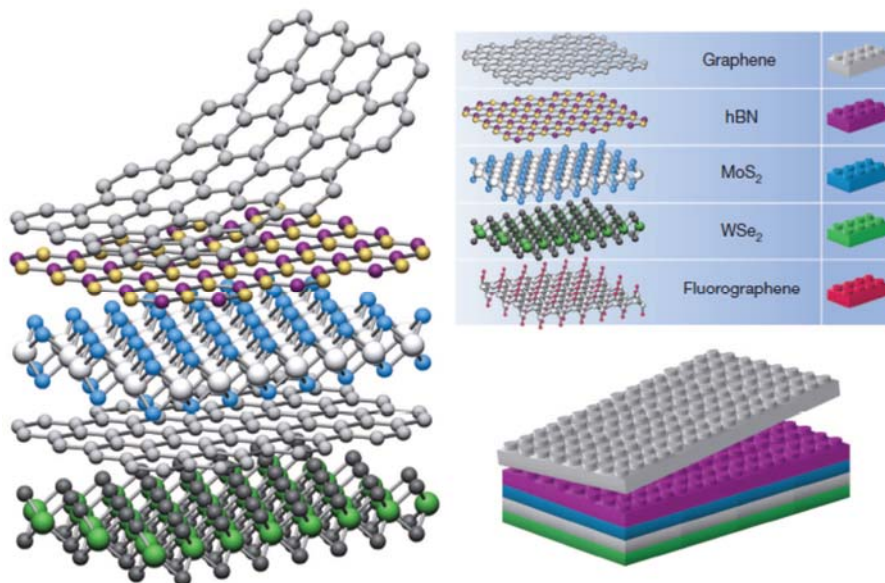
Figure 24. Van der Waals heterostructures.[45]

3.2| Experimental Section

3.2.1| Preparation of a Heterostructure of Graphene on hBN

Graphene film was synthesized by CVD on 25-μm-thick copper foil (99.8 % Alfa Aesar, Ward Hill, MA, USA). For synthesizing large-sized grains of graphene, the vapor pressure of hydrogen and methane was controlled as previously described.[59] The working pressure of hydrogen was 1.5×10^{-2} Torr, increasing to 1.3×10^{-1} Torr after inputting methane. The synthesized graphene was transferred to Quantifoil TEM grids by the direct transfer method.[21] The copper substrate was etched away in $Na_2S_2O_8$ solution (0.2 mg $Na_2S_2O_8$/ mL water) for 12 h. The average grain size of the graphene exceeded 2 μm; consequently, the grains covered the whole area of a 2-μm-diameter hole in the Quantifoil TEM grid.

The synthesis and transfer process of the hBN film are described in a previous paper.[60] The hBN films were synthesized under low-pressure CVD on platinum foil of thickness 125 μm (99.95%, Goodfellow) with ammonia borane precursor, and transferred onto a graphene/Quantifoil TEM grid by the electrochemical bubbling method.

3.2.2| Structural Characterization

TEM characterization was conducted in a Cs image aberration-corrected FEI Titan Cube TEM with an electron monochromator operated at 80 kV. The moiré fringes were acquired along the $\{10\bar{1}0\}$ diffraction reflections of graphene and hBN by DF-TEM imaging. The diameter of the objective aperture was approximately 1.2 nm^{-1} in electron diffraction mode. The acquisition times of the DF-TEM images and atomic resolution TEM images were 5 and 0.3 s, respectively.

3.2.3| Image Simulation

The atomic model simulation images were generated in Photoshop and Jmol, an open-source Java viewer for three-dimensional chemical structures that reads a variety of file types and generates output from quantum chemistry programs. Jmol animates multiframe files and computes the normal modes from the quantum programs. The mainframe of the model was constructed by VESTA. Atomic resolution TEM image simulation were conducted by the multislice method in MacTempas package.

3.3| Moiré Patterns by Interference Between Stacked Layers

Moiré superstructures can be topologically analyzed under a scanning tunneling microscope (STM) and TEM.[61, 62] Mismatches of crystals from different lattice constants and relative orientations produce periodic new superstructures with larger periodicity than the lattice constants themselves[14], which

25

emphasizes the local configurational changes induced by defects and strain even though the individual lattice structures cannot be resolved.[63-65] Moreover, DF-TEM analysis with SAED reveals structural information along a selected orientation with an appropriate objective aperture, so it has been widely applied in analyses of structural defects such as stacking boundaries,[7, 66] distribution of grains,[67, 68] and dislocations and stain field (**Figure 25**).[69]
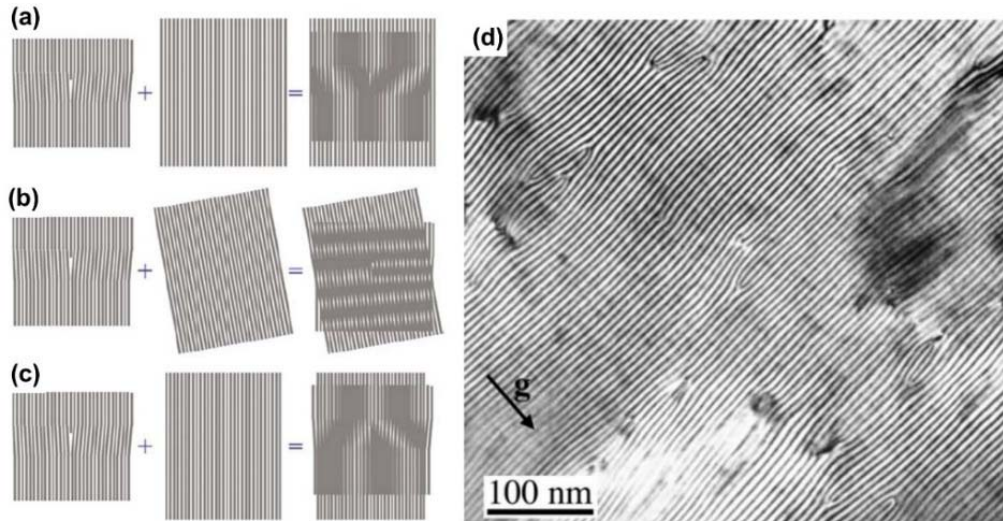
Figure 25. Application of moiré patterns for study on defects.[14]

3.3.1| Rotational Moiré Patterns of Bilayer Graphene

Artificially stacked bilayer graphene as an example of rotational moiré superstructure shows periodic hexagonal patterns and moiré fringes just in one orientation when rotated (**Figure 23**). The periodicity of moiré patterns and the spacings between the moiré fringes depend on the twist angle between two layers. In other words, the periodicity and the spacings let us know the twist angle between layers.

$$d_{rm} = \frac{1}{g_{rm}} = \frac{1}{g_2 - g_1} = \frac{1}{2g \sin{\theta_{inter}/2}} = \frac{d}{2 \sin{\theta_{inter}/2}}$$
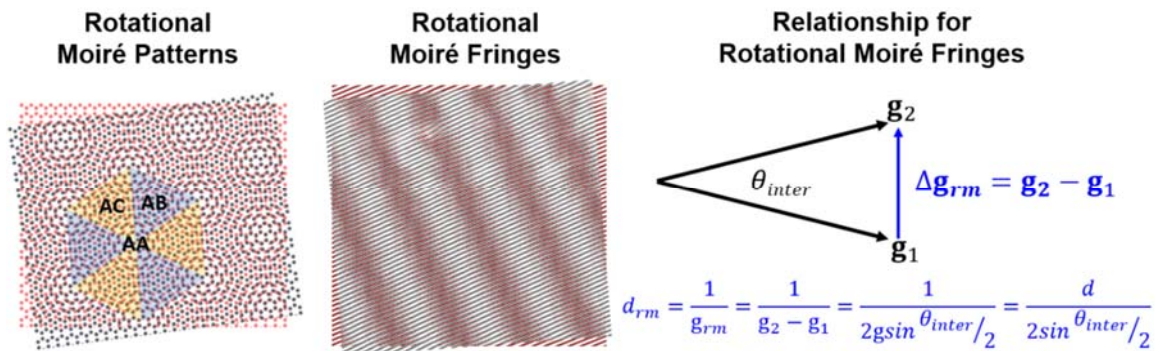
Figure 26. A schematic of moiré superstructures in bilayer graphene.

DF-TEM imaging visualizes moiré fringes and determine twist angles of graphene sheets at a resolution less than degree (**Figure 27**). It enables mapping of twist angle variations between stacked layers and superlattice domain sizes and let us know intra-misorientation angles at the grain boundaries.[70] Furthermore, it reveals discrete nanosized superlattice domains and wrinkles inevitably generated during the fabrication of artificially stacked bilayer graphene, which should have a detrimental effect on the properties of materials.
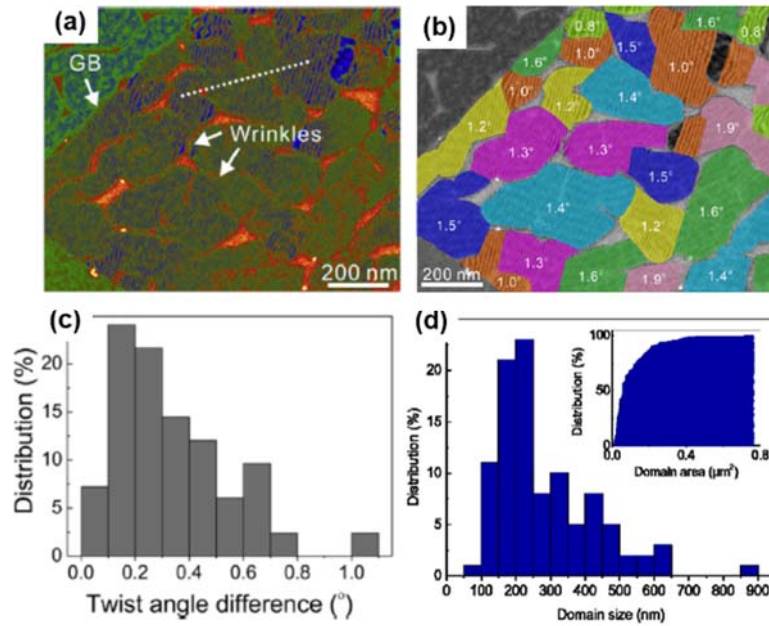
Figure 27. Superlattice domains generated by wrinkles in stacked bilayer graphene.[71]
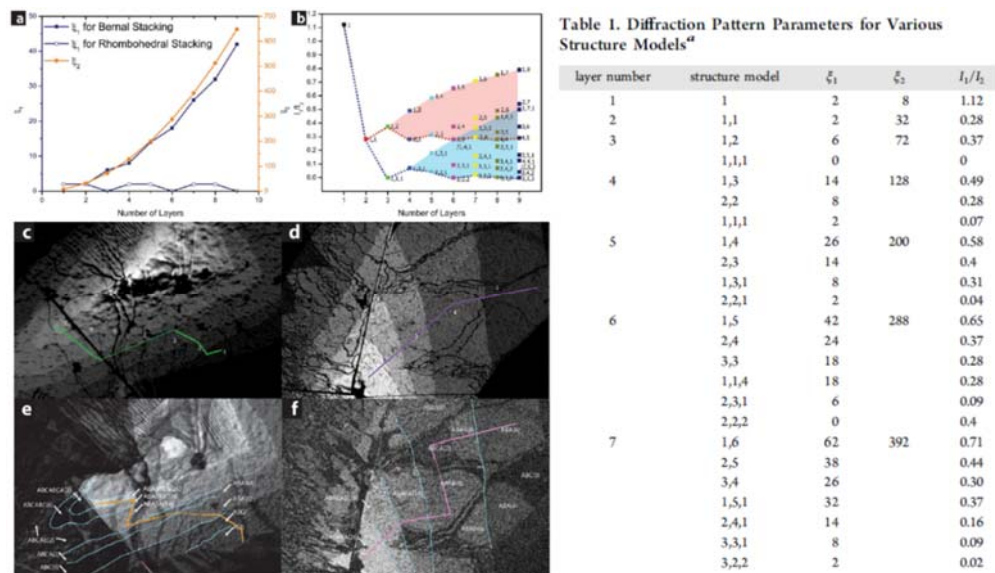
Figure 28. Intensity variation depending on the stacking structure and the number of layers in the DF-TEM image of multilayer graphene.[72]

When graphene is stacked along the same orientation or has regular stacking structure, there is just contrast difference in a DF-TEM image depending on the stacking configuration. As increasing the number of graphene layers, the intensity of the DF-TEM image in the 2nd order diffracted reflection (I_2) increases regardless of the stacking configuration (**Figure 28**). On the other hand, one in the 1st order diffracted reflection (I_1) shows strong dependence on stacking configuration. The ratio of I_1/I_2 let us assume the stacking configuration in the multilayer graphene.

3.3.2| General Moiré Patterns of Graphene on hBN

When graphene is stacked on hBN, the general moiré superstructures show unperiodic hexagonal-like moiré patterns and diverse spacings and directions on the moiré fringes when rotated, which depends on the twist angle and a difference in lattice constants (**Figure 29**). There are two factors affecting on the general moiré superstructures, so it could give more information about interlayer relationship like twist angle and distribution of the grain boundaries on 2D materials.[73]
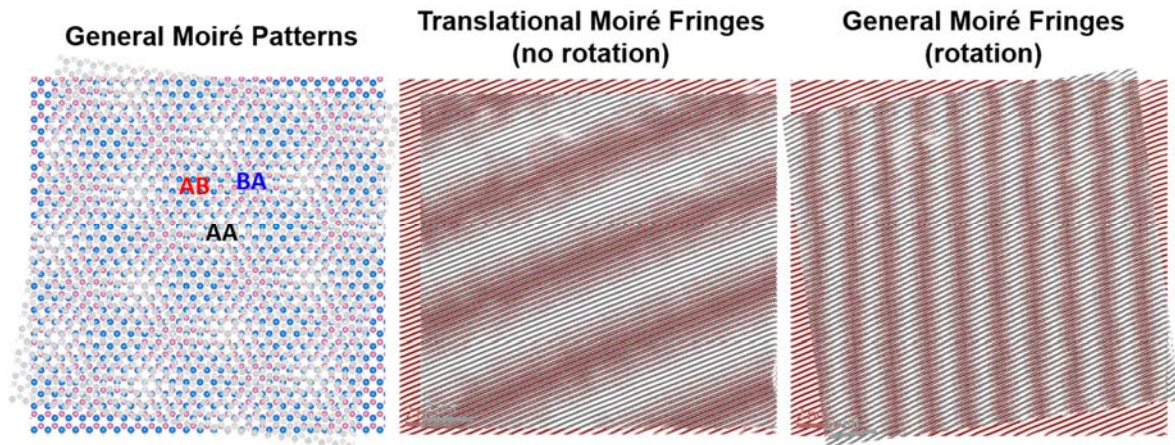
Figure 29. A schematic of moiré superstructures in graphene on hBN.

In particular, the direction of moiré fringes let us do mapping of grain boundary on the single layer system. **Figure 30** shows the comparison between rotational and general moiré fringes in terms of direction in the fringes. The general moiré fringes show the different direction whereas the rotational moiré fringes show the same direction when rotating clockwise and counterclockwise as 4°. The direction-dependence in the general moiré fringes could resolve intra-misorienation angle at the grain boundaries clearly as shown in **Figure 31**.

Rotational Moiré Fringes **General Moiré Fringes**

Counterclockwise 4°   Clockwise 4°   Counterclockwise 4°   Clockwise 4°
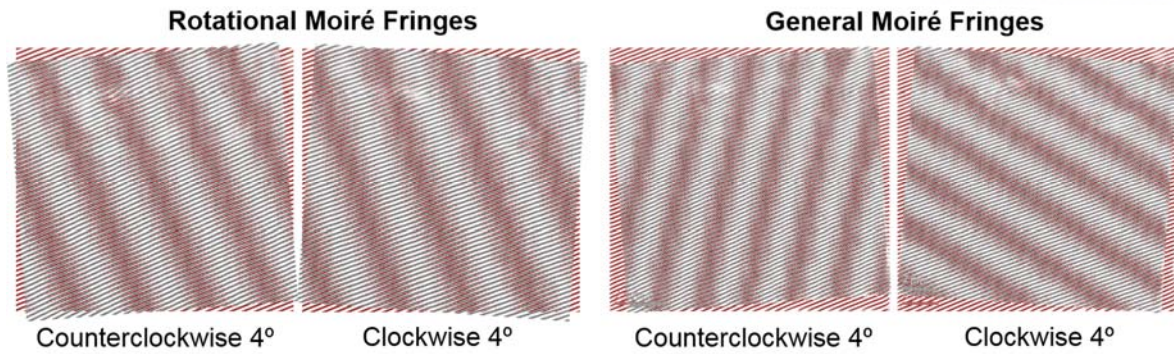
Figure 30. Comparison of moiré fringes in terms of direction.
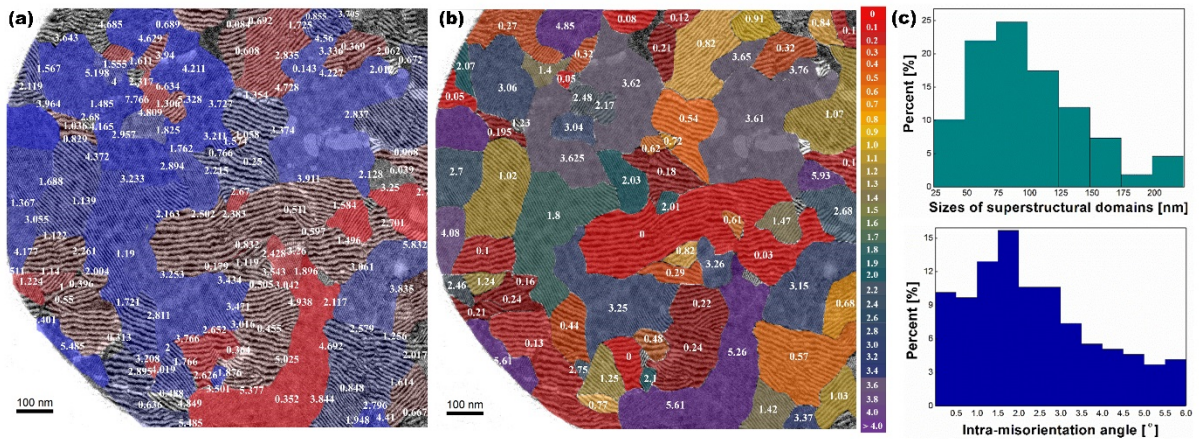
Figure 31. Colored DF-TEM images showing relative misoriented angles between hBN domains with distribution superstructural domain sizes and intra-misorientation angles between hBN domains.

Figure 31(a) represent that the domains of red color are rotated clockwise and ones of blue color are rotated counterclockwise relative to the graphene's orientation (the diffraction vector of graphene). When a domain is rotated clockwise as 1 degree (red domains) and the other one is rotated counterclockwise as 1 degree (blue domains), there is no difference in the case of rotational moiré fringes. On the other hand, the general moiré fringes show the direction-dependence in the moiré fringes, which reveals the intra-misorienation angles as 2 degrees at the boundaries between red and blue domains. Therefore, the general moiré fringes can analyze the real distribution of the superlattice domains and grain boundaries in the single 2D system.
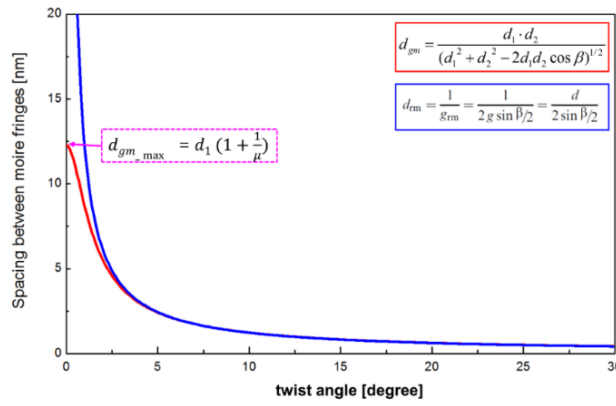
Figure 32. Spacing between moiré fringes *versus* the twist angle between stacked two layers.

Figure 32 shows that the spacing moiré fringes has reciprocal relation with the twist angle between layers and an analysis on moiré fringes is appropriate to investigate the interlayer relation at the small twist angle. The spacing d_{rm} of rotational moiré fringes (such as bilayer graphene and bilayer hBN) becomes infinitely large as the twist angle between stacked layers approaches zero without dependence of the lattice constants. That's why there is just a difference in intensity in a DF-TEM image when two layers are stacked along the same orientation or has regular stacking structure. On the other hand, the general moiré fringes show that their spacing d_{gm} is constrained by lattice mismatch (μ). Consequently, moiré fringes are always observed in the DF-TEM image when there is lattice mismatch between two layers.

3.4| Interfacial Relation of Graphene on hBN: Study on Moiré Fringes in DF-TEM

For investigation on the interfacial relation and interlayer interaction between graphene and hBN, the twist angle between layers ($\theta_{\text{G-BN}}$) was measured precisely from the general moiré fringes of G/hBN ($\mathbf{g}_{gm}$) which are the difference between the diffraction vectors of graphene ($\mathbf{g}_G$) and hBN ($\mathbf{g}_{BN}$).

The schematic in **Figure 33** illustrates how to get $\theta_{G\text{-}BN}$. $\mathbf{g}_{BN}$ and $\mathbf{g}_G$ are the diffraction vectors in a reciprocal space of hBN and graphene, respectively. In Method 1, the diffraction vector of the general moiré fringe ($\mathbf{g}_{gm}$) is perpendicular to the moiré fringes in real space. The length of the diffraction vector is reciprocally related to the interplanar spacing of the diffracted reflections, so the length of $\mathbf{g}_{gm}$ ($1/d_{gm}$) is determined by one of $\mathbf{g}_G$ and $\mathbf{g}_{BN}$ which expressed as $d_{gm} = \dfrac{d_G \times d_{BN}}{(d_G{}^2 + d_{BN}{}^2 - 2d_G \cdot d_{BN} \cdot \cos(\theta_{\text{G-BN}}))^{1/2}}$. From the lengths of moiré fringes, graphene and hBN, $\theta_{G\text{-}BN}$ can be calculated. In Method 2, the diffraction vectors form a triangle with their lengths and angles. From these lengths and the angle of moiré fringes relative to graphene and hBN, $\theta_{G\text{-}BN}$ is calculated by *the sine law* as follows: $\dfrac{a}{\sin A} = \dfrac{b}{\sin B} = \dfrac{c}{\sin C} = 2R$.

Methods for twist angle between graphene and hBN ($\theta_{G\text{-}BN}$)

General moiré fringe

$$g_{BN} = \frac{1}{d_{BN}} \qquad 90°+\beta$$

$$g_{gm} = \frac{1}{d_{gm}}$$

$$\theta_{G\text{-}BN} \qquad 90°-\alpha$$

$$g_{G} = \frac{1}{d_{G}} \qquad \alpha$$

α: angle between moiré fringes and the diffraction vector of graphene (g_G)
β: angle between moiré fringes and the diffraction vector of BN (g_{BN})
$\theta_{G\text{-}BN}$: angle between g_G and g_{BN}

Method 1_spacing between moiré fringes

$$d_{gm} = \frac{d_G \cdot d_{BN}}{(d_G^2 + d_{BN}^2 - 2d_G d_{BN} \cos\theta_{G\text{-}BN})^{1/2}}$$

$$\theta_{G-BN} = \arccos\left(\frac{d_G^2 + d_{BN}^2 - \left(\dfrac{d_G d_{BN}}{d_{gm}}\right)^2}{2 \cdot d_G d_{BN}} \right)$$

Method 2_The law of sine

$$\frac{\sin(90°-\alpha)}{\dfrac{1}{d_{BN}}} = \frac{\sin(90°+\beta)}{\dfrac{1}{d_G}} = \frac{\sin(\theta_{G\text{-}BN})}{\dfrac{1}{d_{gm}}}$$

$$\beta = 90° - \arcsin\left(\frac{d_{BN} \cdot \sin(90°-\alpha)}{d_G}\right)$$

$$\theta_{G\text{-}BN} = \alpha - \beta$$
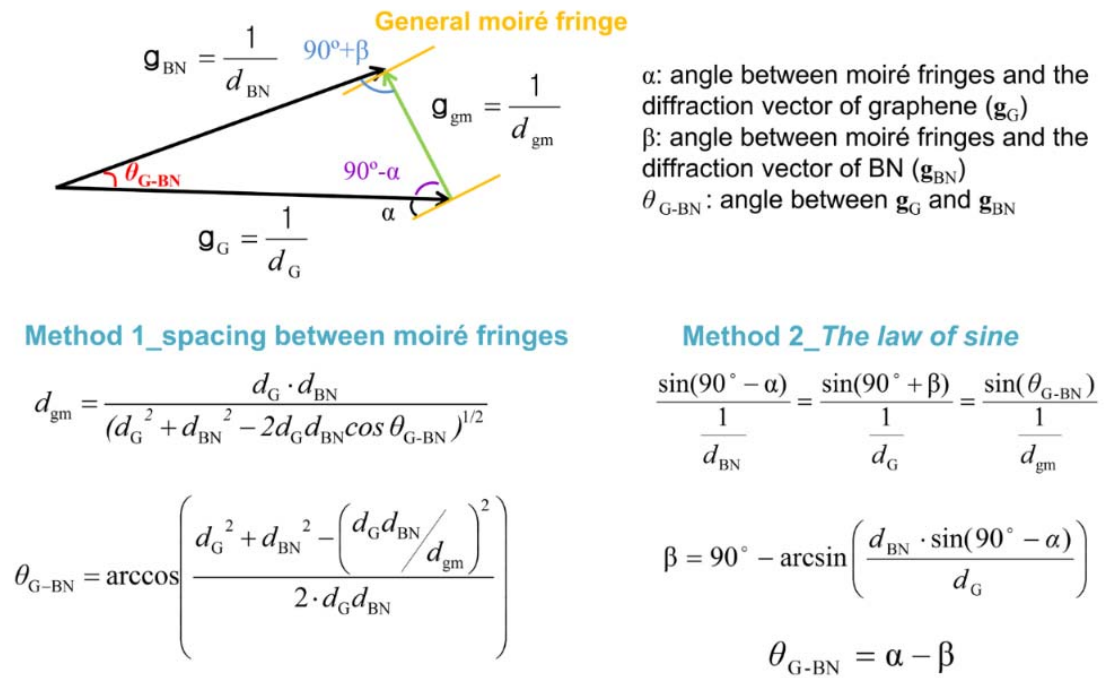
Figure 33. A schematic how to get the twist angle between graphene and hBN ($\theta_{G\text{-}BN}$) from the moiré fringes.[73]

Monolayer graphene

Spot #	d-spacing (nm)
1	0.2131
2	0.2095
3	0.2119
4	0.2123
5	0.2098
6	0.213

Monolayer h-BN

Spot #	d-spacing (nm)
1	0.22
2	0.2134
3	0.2152
4	0.2187
5	0.2132
6	0.2169

Statistical results

	h-BN (Å)	Graphene (Å)
Average (M)	2.169	2.130
Standard deviation (SD)	0.020	0.019
Standard error (SE)	0.002	0.002
M+SE	2.170	2.132
M-SE	2.167	2.128

Lattice mismatch between avg [%]	1.801
Lattice mismatch_max [%]	1.983
Lattice mismatch_min [%]	1.619

Figure 34. A schematic how to take the interplanar spacing between $\{10\bar{1}0\}$ of graphene and hBN (d_G and d_{BN}) from the AR-TEM images.[73]

It is essential to get the d_G and d_{BN} experimentally at first to get the d_{gm}. **Figure 34** delineates the process how to get the d_G and d_{BN} experimentally from the AR-TEM images with the corresponding FFTs. Many images (over 30) were collected from clean large-area monolayer graphene and hBN under the same TEM condition. Then, d_G and d_{BN} were taken from the corresponding FFTs, and their statistics were computed. The average d_G and d_{BN} were 2.130 Å and 2.169 Å with low standard deviation of 0.02 Å, respectively. μ between graphene and hBN ranged from 1.619% to 1.983%. Therefore, it appears that the suggested process for d_G and d_{BN} is reasonable to deduce $\theta_{G\text{-}BN}$ exactly.
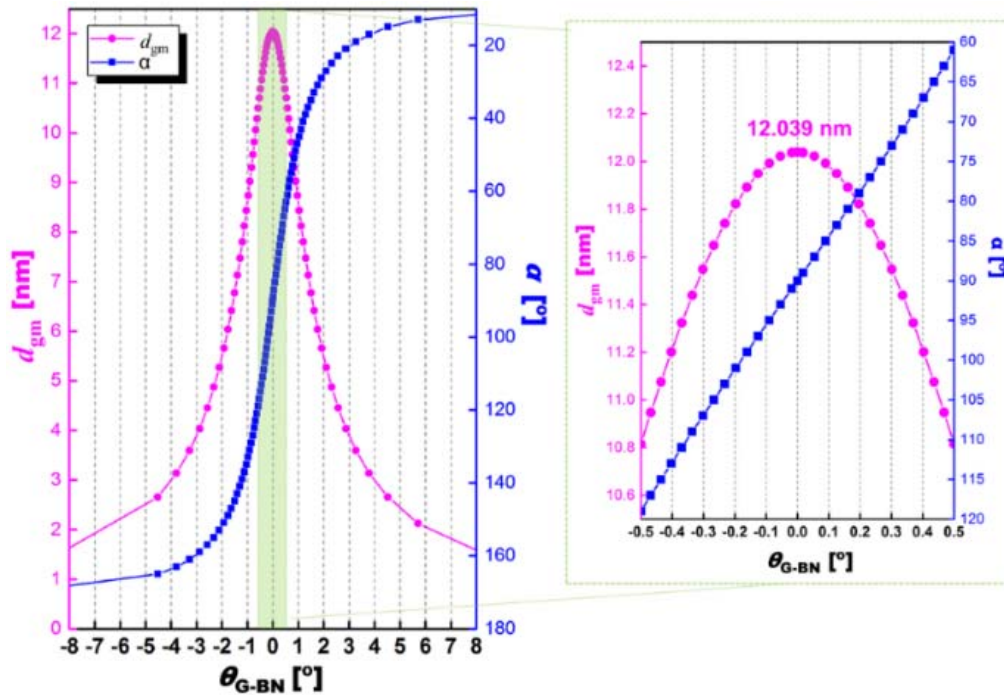
Figure 35. Sensitivity of general moiré fringes at the low twist angle.[73]

The suggested methods also let us recognize sensitivity of general moiré fringes on small $\theta_{G\text{-}BN}$ by plotting the $\theta_{G\text{-}BN}$ as a function of d_{gm} (left column) and as a function of the angle between moiré fringes $\mathbf{g}_G$ (α) (right column) determined by three factors: $\theta_{G\text{-}BN}$, d_G, and d_{BN}. (**Figure 35**) Magenta and blue lines indicate the distributions of $\theta_{G\text{-}BN}$ and d_{gm} in Method 1 and the distribution of $\theta_{G\text{-}BN}$ and α in Method 2, respectively. There is a difference in α around 3° which is enough to be resolved when $\theta_{G\text{-}BN}$ is just 0.1 degree and the difference becomes larger as increasing the $\theta_{G\text{-}BN}$, which could investigate the interlayer relation on $\theta_{G\text{-}BN}$ accurately, in particular, at small $\theta_{G\text{-}BN}$.

For G/hBN, μ is assumed that around 1.8%. It constrains the maximum spacing of the general moiré fringes as 12.039 nm when $\theta_{G\text{-}BN} = 0°$.
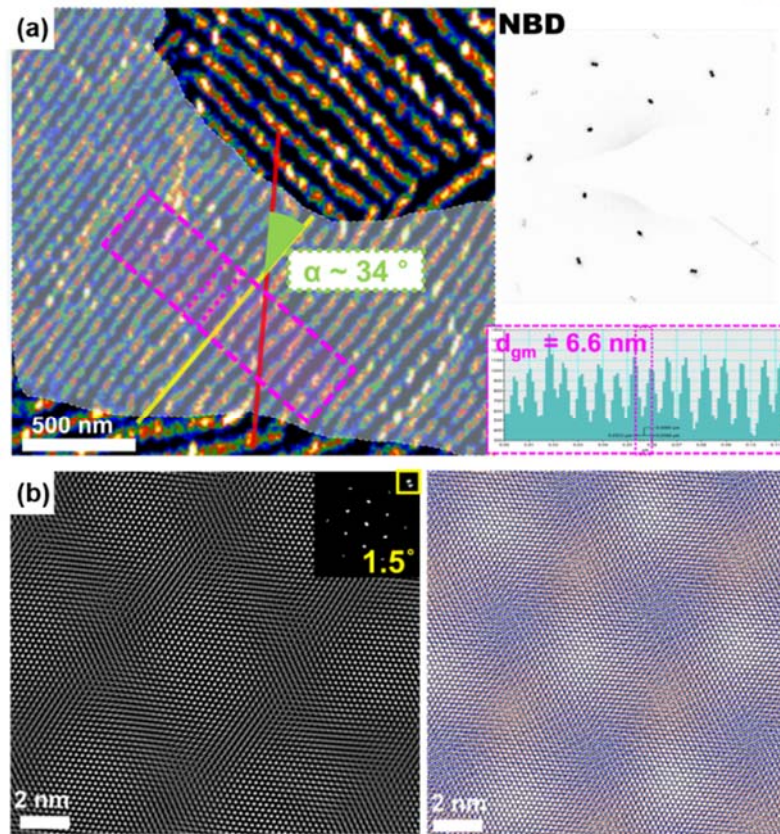
Figure 36. Reliability of the suggested methods for $\theta_{\text{G-BN}}$.[73]

The above figure represents high reliability of the suggest methods to get $\theta_{\text{G-BN}}$ from d_{gm} and the angle between $\mathbf{g}_G$ and the moiré fringes (α). The orientation of the moiré fringes and distribution of d_{gm} are highlighted by the yellow line and magenta box, respectively. The corresponding nanobeam diffraction (NBD) patterns reveal the orientation of $\mathbf{g}_G$ (marked by red line) and the $\theta_{\text{G-BN}}$.

For the method 1, d_{gm} = 6.6 nm (**Figure 36(a)**) and the experimental d_G (2.130 Å) and d_{BN} (2.169 Å) are inserted into the equation in method 1 (**Figure 33**) and the $\theta_{\text{G-BN}}$ is estimated as 1.56º. For the method 2 based on the sine law, the measured α as 34º (**Figure 36(a)**) is substituted into the equation in method 2 (**Figure 33**) and it results in $\theta_{\text{G-BN}}$ around 1.56º. It appears very similar calculated angles from the two methods (approximately 1.5º).

The consistency of the calculated $\theta_{\text{G-BN}}$ with real lattices was examined by NBD patterns and AR-TEM imaging. The NBD pattern and the digital diffractogram (FFT) corresponding to an AR-TEM image are presented in **Figure 36(a) and (b)**, respectively. The FFT distinguishes two sets of diffracted reflections with a $\theta_{\text{G-BN}}$ of approximately 1.5º. Moreover, the experimental AR-TEM image is consistent with the schematic atomic model of G/hBN (**Figure 36(b)**). Therefore, the moiré fringe analysis with DF-TEM imaging can reliably resolve $\theta_{\text{G-BN}}$.

3.5| Transition to Commensurate States of Graphene on hBN

When the twist angle of G/hBN ($\theta_{\text{G-BN}}$) is less than 2º, G/hBN exhibits a distinctive Hofstadter's butterfly structure with additional satellite resistance peaks and the maximum band gap appears at $\theta_{\text{G-BN}} = 0$º.[74] As $\theta_{\text{G-BN}}$ decreases, the in-plane elastic energy weakens and approaches the vdW energy. Under this condition, the graphene lattice can relax toward an hBN lattice at the cost of graphene layer distortion.[75, 76] The interlayer interaction depends on the stacking configurations, which results in inhomogeneous strains and corrugation on the G/hBN heterostructure.
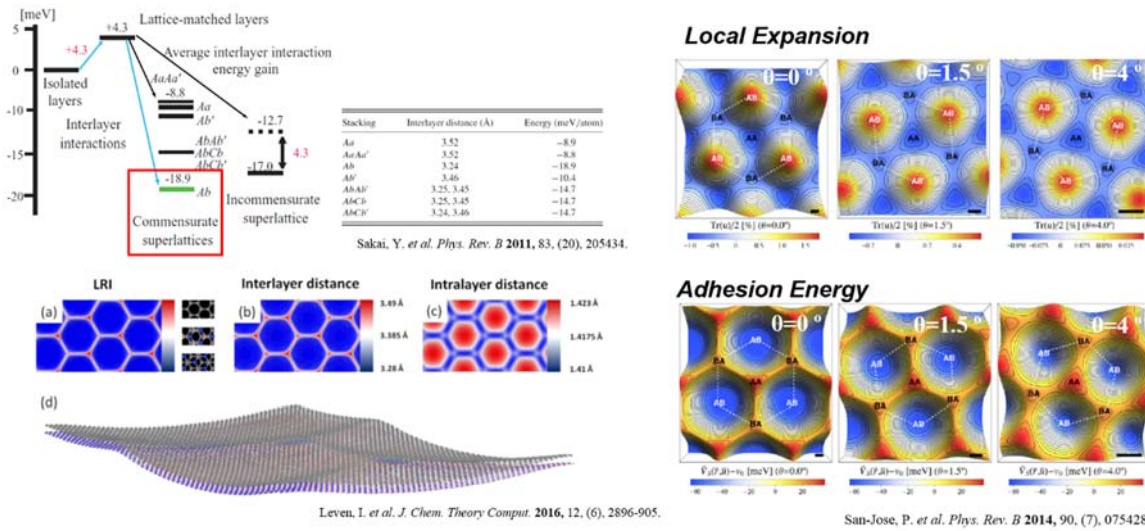
Figure 37. Theoretical researches on the local transition to a commensurate state of G/hBN depending on the stacking configurations.[54, 76, 77]

The graphene lattice primarily relaxes around the AB-stacked regions, wherein carbon (C) atoms are located above the boron (B) atoms. Lattice relaxation changes the electronic structures by opening a small band gap at the Dirac point of graphene.[75, 78]

3.5.1| Dependence of Twisted Angle Between Graphene and hBN
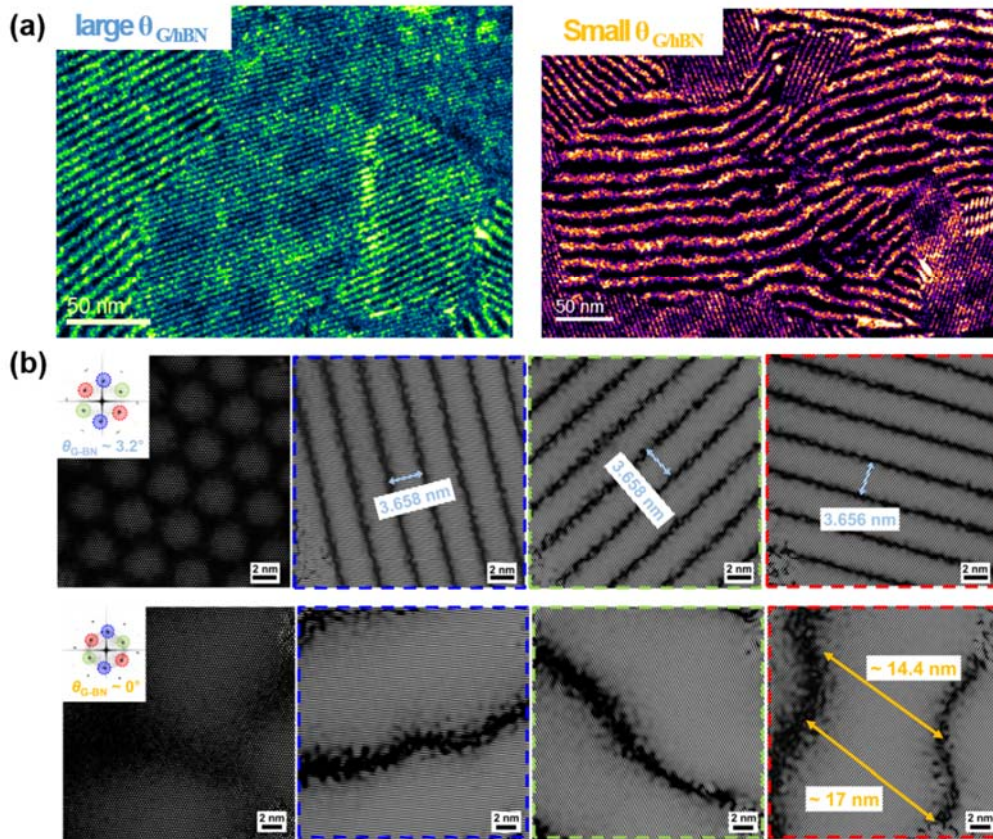
Figure 38. Widening and bending of the moiré fringes of G/hBN only at low $\theta_{G\text{-}BN}$ in (a) DF-TEM and (b) AR-TEM images.[73]

As $\theta_{G\text{-}BN}$ decreases, the general moiré fringes in the DF-TEM images are unevenly distributed and periodically bent (**Figure 38(a)**). To account for the unique feature, the AR-TEM image was subjected to lattice fringe imaging analysis by masking on the selected orientations on the FFT in order to correlate with the DF-TEM image (**Figure 38(b)**). The moiré fringes in the masked AR-TEM image of G/hBN show same features depending on $\theta_{G\text{-}BN}$. At large $\theta_{G\text{-}BN}$ ($\theta_{G\text{-}BN} = 3.2°$), the moiré fringes are evenly distributed at all orientations, in other words, the all d_{gm} at three orientations are consistent and equal to 3.66 nm. At this $\theta_{G\text{-}BN}$, the moiré fringes appear quite straight and parallel and are noncorrugated and constant in width. When graphene and hBN are aligned along the same orientation ($\theta_{G\text{-}BN} \approx 0°$), the moiré fringes are largely corrugated at all orientations, and some d_{gm} exceeds its maximum of 12.039 nm when μ is 1.8% between graphene and hBN.

To investigate the unique feature in moiré fringes depending on $\theta_{G\text{-}BN}$, it is essential to correlate between the moiré fringes in the DF-TEM images and ones in the masked AR-TEM image.

The lattice fringe images in the **Figure 39** were acquired by applying the masking technique implemented by a digital micrograph. Monolayer graphene and hBN images were converted to lattice fringe images in each orientation. The lattice fringes have uniform widths (except in low-intensity regions) and the area of the adsorbates varied under the inhomogeneous distribution of the electron beam intensity and adsorbate disturbance.

The intensity of the fringes follows the Howie–Whelan equations; that is, it sinusoidally oscillates normal to the diffraction vector g. The period of the oscillation depends on the excitation error and the thickness of the specimen. If the specimen is not exactly flat, the fringes will shift in succeeding images; however, the periodicity will not noticeably change.
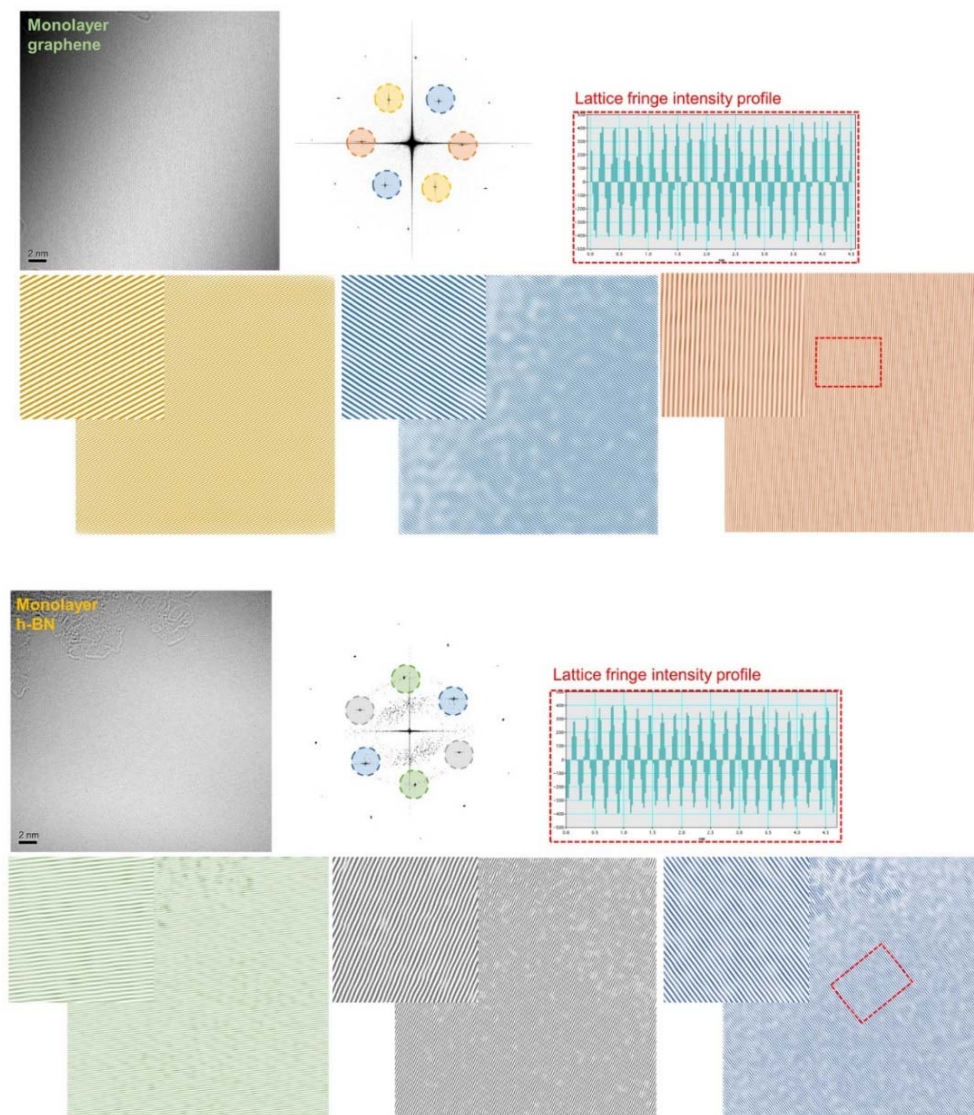
Figure 39. Lattice fringe analysis by masking on the FFTs corresponding to the AR-TEM image along the $\{10\bar{1}0\}$ diffraction reflections on the monolayer graphene and hBN.[73]
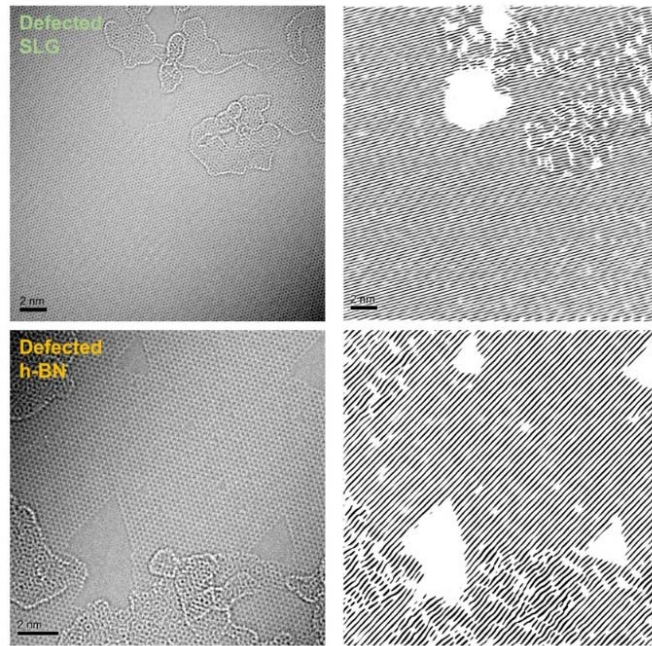
Figure 40. The real AR-TEM images and corresponding lattice fringes images of defective monolayer graphene and hBN.[73]

The lattice fringes images (right) are well matched with AR-TEM images (left) in **Figure 40**, which indicates high reliability of masking technique to study 2D materials. The lattice fringe images highlight the defective regions of hole defects and hydrocarbon residues even few $Å^2$ area.
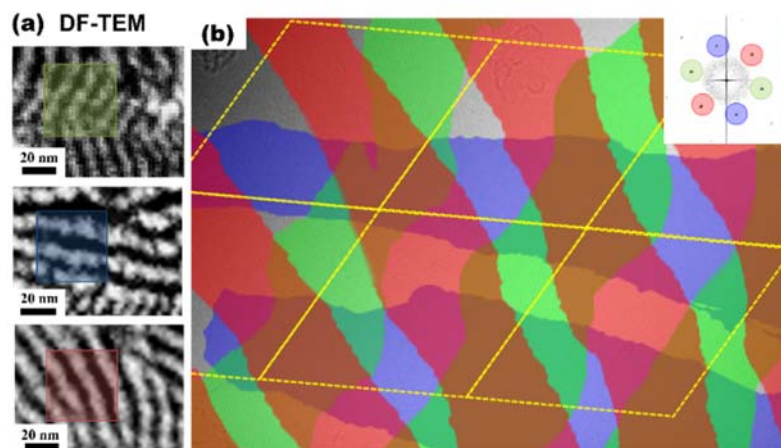
Figure 41. The moiré fringes in the DF-TEM images and ones in the masked AR-TEM image.[73]

Figure 41 represents high correlation between the moiré fringes in the DF-TEM images and ones in the masked AR-TEM image. Therefore, the masking technique on the AR-TEM image is appropriate to investigate the interlayer interaction by corelating with the moiré fringes in the DF-TEM image.
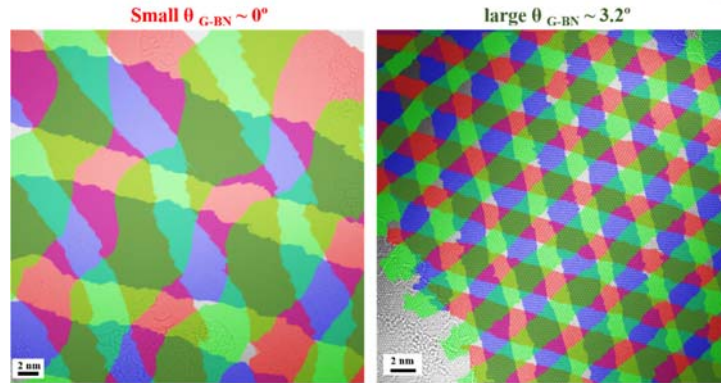
Figure 42. Comparison of the moiré fringes at between small and large θ_{G-BN} by masking on AR-TEM images.[73]

The **Figure 42** shows the different morphology of the moiré fringes at between small and large θ_{G-BN} when all lattice fringes are superimposed depending on the selected orientations. There are three types of the moiré fringes owing to hexagonal symmetry in G/hBN. The moiré fringes are periodically bent and widened little only at the small θ_{G-BN}. It appears that the periodic change is related with stacking configurations of graphene on hBN and it results from the different interlayer interaction depending on the stacking configurations.

3.5.2| Dependence of Stacking Structures

The contrast of moiré fringes results from interference between graphene and hBN lattice fringes as constructive (bright) and destructive (dark) interferences, respectively, which depends on difference in phase shift in accordance with stacking configuration (**Figure 43**).
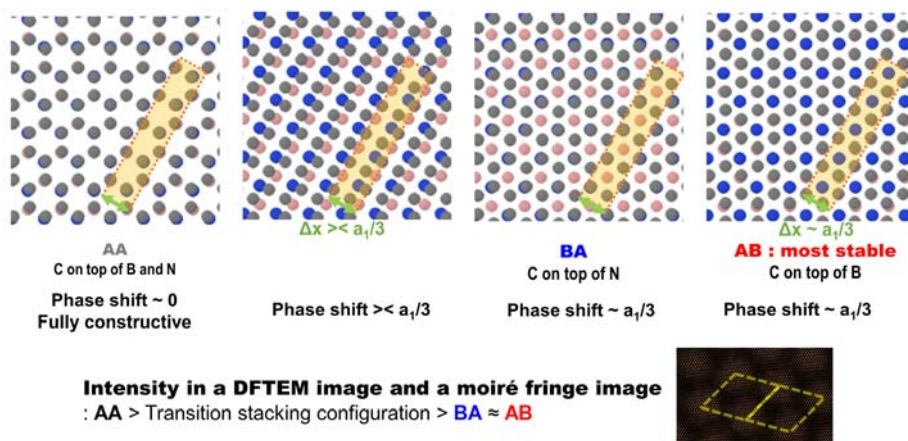
Figure 43. A schematic of contrast in the moiré fringes caused by interference between the lattice fringes of graphene and hBN in DF-TEM depending on the stacking configuration.[73]
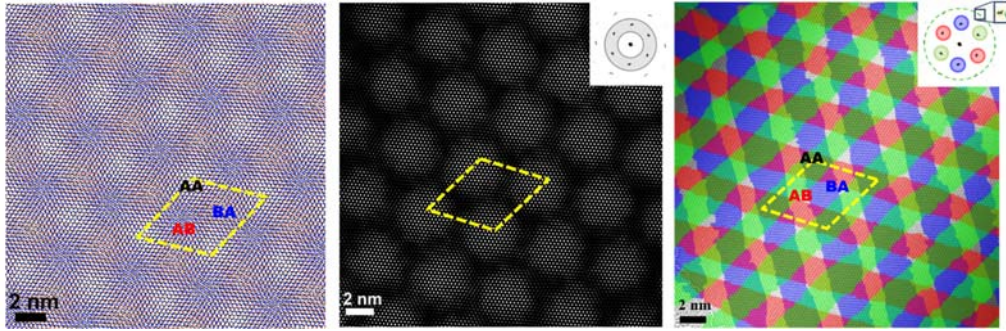
Figure 44. Schematic atomic model and lattice fringe images taken by masking on the 1st order diffraction reflections of AR-TEM images of G/hBN with two sets of hexagonal diffraction reflections in the corresponding FFTs at large $\theta_{\text{G-BN}}$ (3.2º).[73]

$\theta_{\text{G-BN}}$ in **Figure 44** is precisely acquired from the directionality of the moiré fringes and the distinguishable diffraction reflections for graphene and hBN in the FFTs, as a result, it is 3.2º. The lattice fringes on all first-order diffraction reflections are periodic, being brightest in the AA-stacked regions and darkest in the BA- and AB-stacked regions. The colorized lattice fringes in the AR-TEM images also show nearly parallel moiré fringes with unvarying morphology for each first-order diffraction reflection.
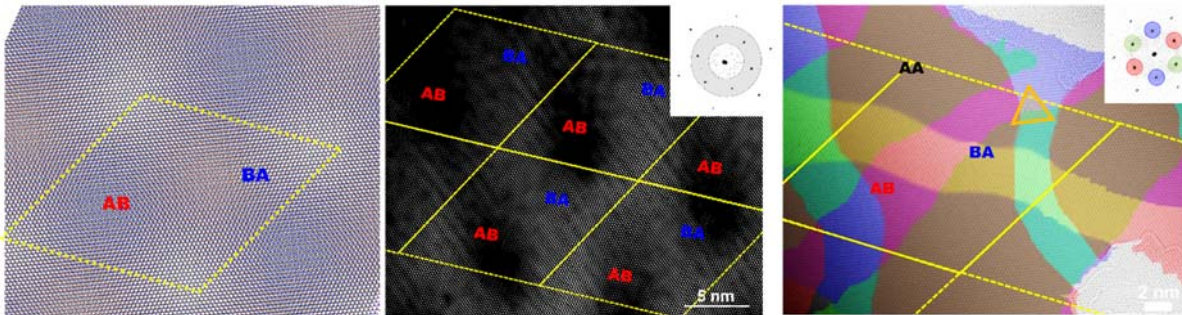
Figure 45. Schematic atomic model and lattice fringe images taken by masking on the 1st order diffraction reflections of AR-TEM images of G/hBN with overlapped one hexagonal diffraction reflection in the corresponding FFTs at large $\theta_{\text{G-BN}}$ (0º).[73]
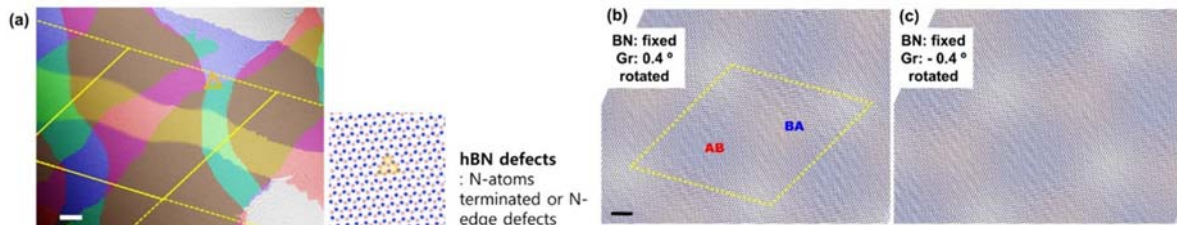
Figure 46. Schematic models for determining the stacking configuration of G/hBN.[73]

On the other hand, it is hard to clearly resolve $\theta_{G\text{-}BN}$ from the overlapped diffracted reflection in the FFT when graphene and hBN have same orientation. The unit size of the hexagonal moiré patterns (~13 nm) and α (~ 65º) with the directionality of the moiré fringes in **Figure 45** and **Figure 46** let us estimate that the hBN is twisted relative to graphene by approximately 0.4° along the counterclockwise direction. The hBN defect indicated by an orange triangle has nitrogen-terminated edges resulting from boron vacancies caused by knock-on damage during e-beam irradiation.[79] This defect stands for the orientation of the hBN, which determines the stacking configuration of G/hBN. The dark area is larger in the AB-stacked regions than in the BA-stacked regions in **Figure 45**, which indicates that AB stacking is energetically favorable stacking sequence. Colored moiré fringes superimposed on an AR-TEM image show widening and zigzagged morphology depending on the stacking configurations. This uneven contrast distribution indicates loss of periodic hexagonal symmetry of G/hBN. Moreover, the d_{gm} are non-uniform in different orientations, indicating uneven twist and strain in G/hBN.[29] The width of the moiré fringes also slightly varies. The periodically zigzagged morphology around 25º is related to the AA-stacked regions and reflects local changes in $\theta_{G\text{-}BN}$.
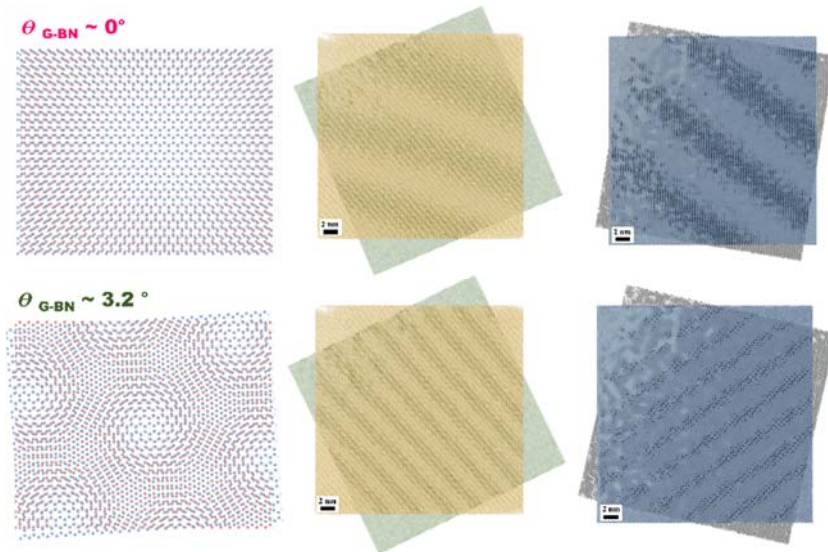
Figure 47. Lattice fringe images from deliberate stacking lattice fringe images of monolayer graphene on one of monolayer hBN.[73]

The lattice fringe images of monolayer graphene and monolayer hBN were deliberately stacked to demonstrate the relation between stacking configuration and the morphology of the moiré fringes (**Figure 47**). The moiré fringes by deliberate overlay are straight and constant in width when $\theta_{G\text{-}BN}$ equals 0º, which indicates that the moiré fringes are independent of the stacking configuration and morphological change in the moiré fringes arises from the interlayer interaction between the artificially stacked graphene and hBN.

3.5.3| Local Lattice Match of Graphene on hBN by Relaxing Graphene Lattices

Small $\theta_{G\text{-}BN}$ approaching to 0º yields distortion in the moiré fringes. The distortion appears to be periodic and to be related with the stacking configurations of G/hBN.
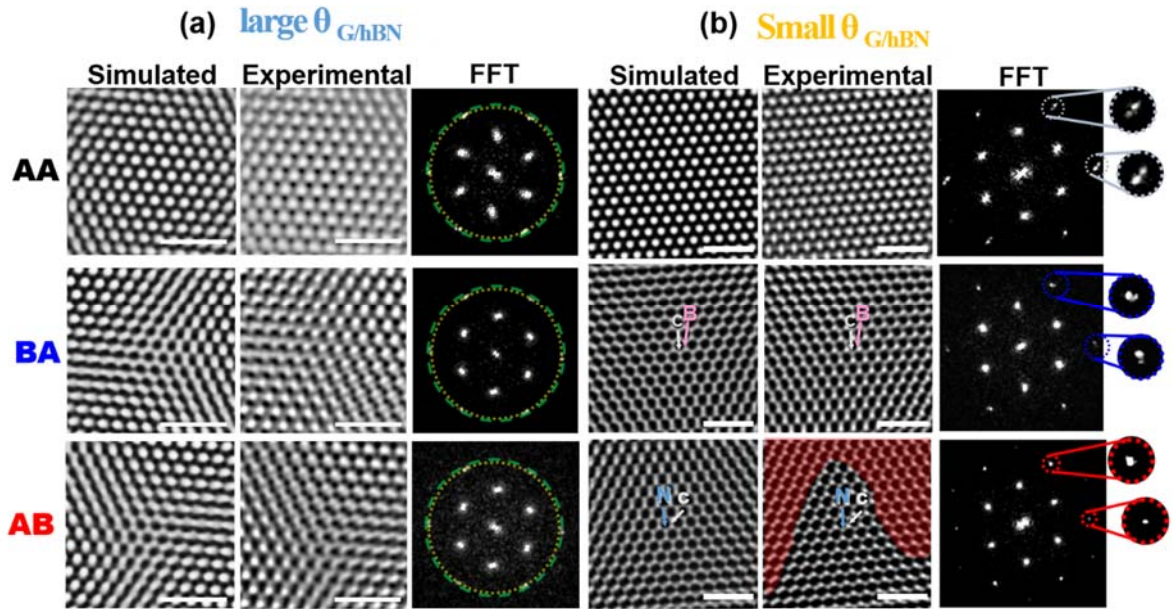
Figure 48. Simulated and experimental AR-TEM images of G/hBN depending on the stacking configuration when $\theta_{G\text{-}BN}$ equals (a) 3.2º and (b) 0º. All scale bars are 1 nm.[73]

Different stacking configurations yield different twisting and diffracted reflection distances of graphene and hBN only when $\theta_{G\text{-}BN}$ approaches to 0º. In the AA-stacked regions, two sets of diffracted reflections indicate twisting and different lengths along the $\{11\bar{2}0\}$ diffraction reflections. The BA-stacked regions also show two distinguishable sets of diffracted reflections, but with less twisting than in the AA-stacked regions. The simulated images are also consistent with the real images in both AA- and BA-stacked regions. In contrast, the AB-stacked region displays a single set of diffracted reflections. A real AR-TEM image shows that intensities of single atoms are much clearer and the areas enlarged where the atoms maintain their hexagonal structure particularly at the AB-stacked region compared to the simulated AR-TEM image. These phenomena denote that the two layers become commensurate states by decreasing their lattice mismatch and locally twisting. In particular, the diffraction patterns of graphene exhibit larger twisting and shrinking behavior than those of hBN; that is, the graphene lattices are transformed to become identical with hBN lattices.
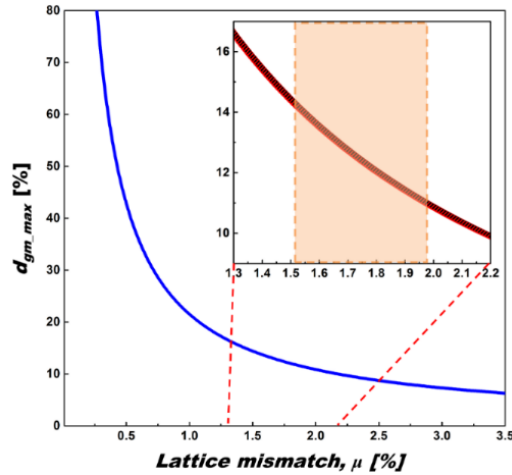
Figure 49. Maximum spacing between general moiré fringes (d_{gm_max}) as a function of lattice mismatch, μ.[73]

There are three factors for moiré fringes of G/hBN: $\theta_{G\text{-}BN}$, d_G, and d_{BN}. When $\theta_{G\text{-}BN}$ is zero for the maximum d_{gm} (d_{gm_max}) and d_{BN} is expressed in terms of d_G and μ, d_{gm_max} simplifies to $d_G\left(1+\frac{1}{\mu}\right)$. As μ increases, the d_{gm_max} drastically changes from infinite to a few nm. My experimental result is consistent with the generally accepted μ (1.8%), so the corresponding d_{gm_max} is 12.039 nm. When μ decreases to 1.4%, d_{gm_max} increases to 15.49 nm. The orange dotted box in **Figure 49** indicates the range of μ obtained from my experimental results. Increased d_{gm} widens the moiré fringes because this parameter affects the periodicity of the sinusoidal intensity oscillations of the lattice fringes.[80] Therefore, the contrast of the moiré fringes is dependent on d_{gm}, in other words, it is reciprocally related with μ.
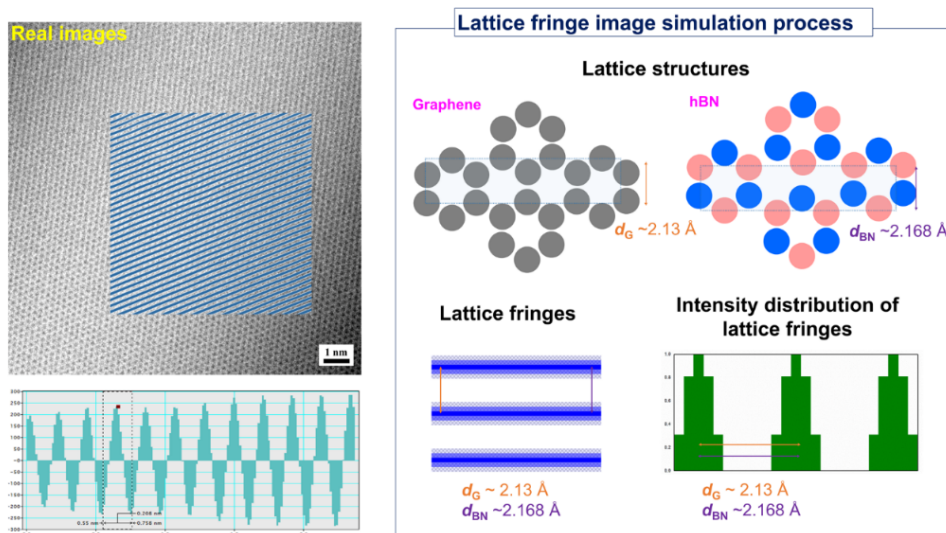
Figure 50. A schematic for lattice fringe image simulation.[73]

To determine whether the moiré fringes were varied by the commensurate state transition, the lattice fringe was imaged by Photoshop (**Figure 50**). The lattice fringe images taken by the masking technique show sinusoidal intensity distributions. This distribution of the lattice fringes was simulated in Photoshop. The intensity of each lattice fringe varies sinusoidally between dark and bright. The periodicity of the darkest fringes was determined from the length of the diffraction vectors along the $\{10\bar{1}0\}$ diffraction reflections.
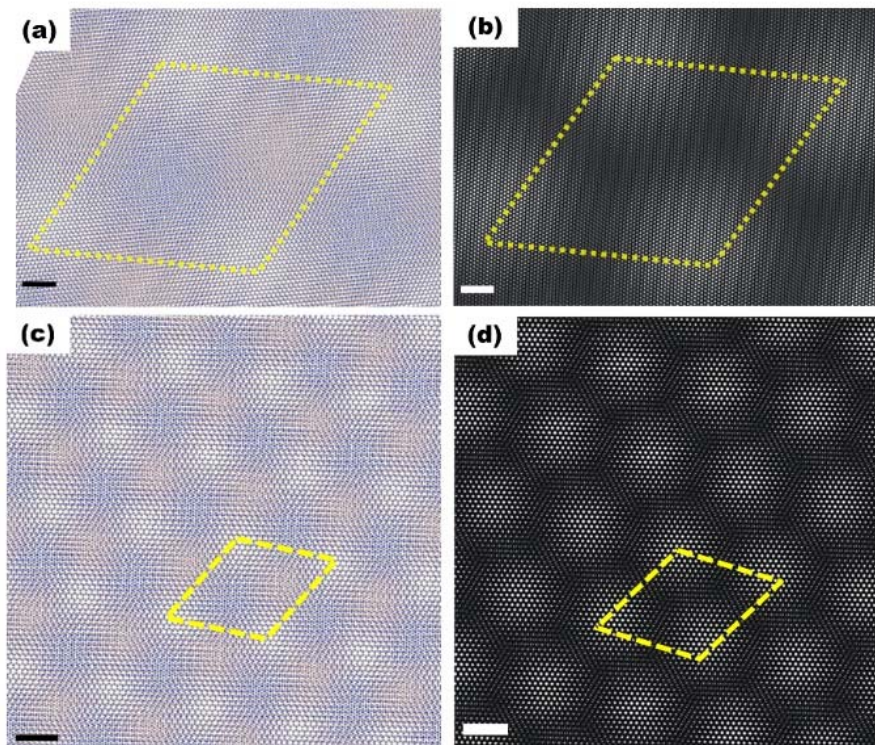
Figure 51. Schematics and moiré fringe images simulated by Photoshop at the $\theta_{g.-BN}$ of 0º and 3.2º.[73]

In the simulated fringe images in **Figure 51**, there is no distortion in the superimposed lattice fringe images, in other words, there is no variation in the intensity at the AB- and BA-stacked areas. The image simulated at 3.2º in **Figure 51(d)** is well consistent with **Figure 44**, which lets us know the high consistency between the simulated and real lattice fringe images.
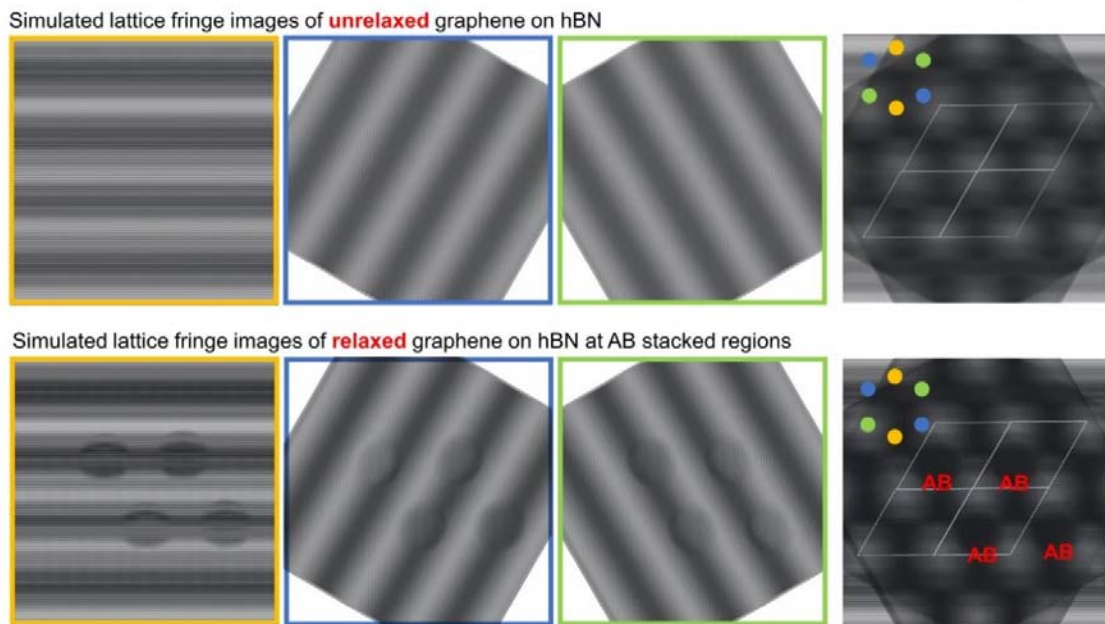
Figure 52. Simulation on the effect of local lattice relaxation on the moiré fringes using Photoshop.[73]

The first row of the **Figure 52** shows the moiré fringe images of unrelaxed graphene on hBN taken by Photoshop. The images shown are three reflections (yellow, blue, and green) and their overlay (fourth column). There is no distortion in the moiré fringes and the moiré patterns from superimposed moiré fringe images. The second row shows the moiré fringes of relaxed graphene on hBN when the graphene lattices are locally extended in the AB-stacked area. The local extension in graphene lattices also expands the distance between the lattice fringes with local corrugation around the AB-stacked areas. As a result, their surroundings change in contrast with local bending and widening, which leads to enlargement of dark contrast areas when superimposing all lattice fringe images in the fourth column.

This simple simulation shows that relaxation on the lattices enlarges the dark area and changes morphology and widths of moire fringes in DF-TEM in **Figure 38, 42, and 45**, which has a larger dark region at the AB-stacked region originated from stretching of the interatomic bond length of graphene.
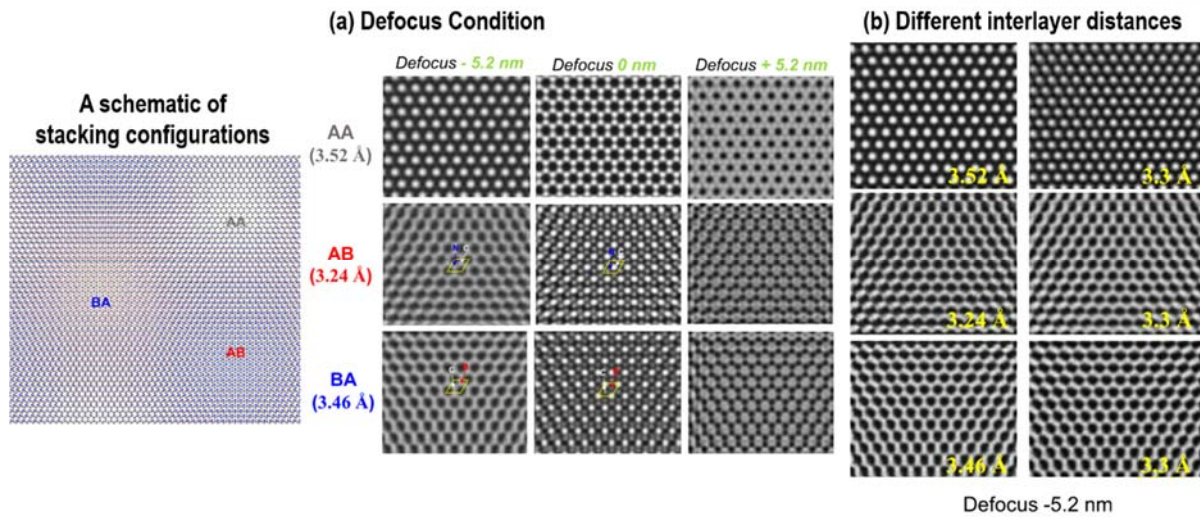
Figure 53. Simulated AR-TEM images of G/hBN for (a) defocused conditions and (b) interlayer distances depending on the stacking configurations.[73]

Atomic resolution TEM image simulation was conducted by the multislice method in MacTempas package to account for the local expansion of perpect AB-stacked area in **Figure 48(b)**. The simulated TEM images in **Figure 53(a)** well match TEM images in **Figure 48(b)** under the − 5.2 nm defocus condition. When considering interlayer distances at the − 5.2 nm defocus condition, it appears that there is no remarkable features like the expansion of pefectly stacked region, where single dots are cleary resolved. The interalayer distances at the first column refer to references.[54] Thus, the image simulation let us know that the local expansion of perpect AB-stacked area in **Figure 48(b)** doesn't result from the difference in the interlayer distance depending on the stacking configuration.
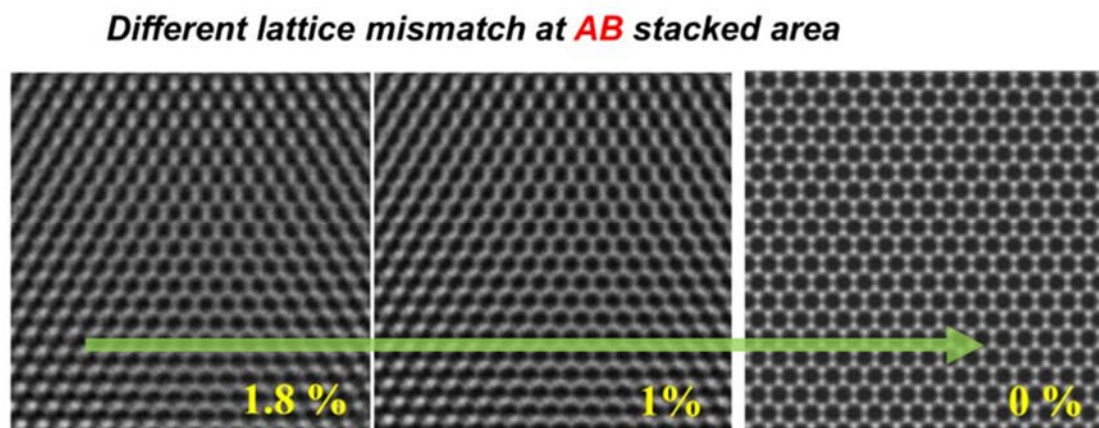
Figure 54. Simulated TEM images of G/hBN depending on the lattice mismatch.[73]

45

To account for the local expansion of perpect AB-stacked area, the lattice mismatch was considered as shown in **Figure 54**: the simulated TEM images in the AB-stacked area for $\mu = 1.8\%$, 1.0%, and 0.0% under the same defocus condition (-5.2 nm). As μ decreases, the intensity of single atoms become distinct, in other words, the hexagonally arrayed single atoms cover a larger area. Therefore, the increased intensity and hexagonal symmetry in red area of **Figure 48(b)** result from the decreased lattice mismatch.
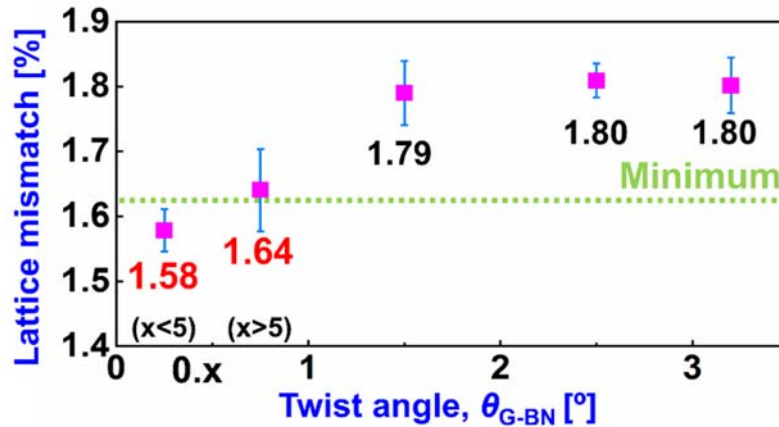
Figure 55. A graph of average lattice mismatch between graphene and hBN *versus* $\theta_{G\text{-}BN}$.[73]

The local commensurate transition in the AB-stacked regions reduces the average μ (**Figure 55**). The lowest average μ is 1.58% when $\theta_{G\text{-}BN}$ approaches 0º, below the minimum μ of 1.62% in monolayer graphene and hBN. As $\theta_{G\text{-}BN}$ increases from 0º to 1º, the average μ rises 1.64% but remains below 1.8%. When $\theta_{G\text{-}BN}$ exceeds 1º, the average μ reaches 1.8%, close to the average μ obtained from pristine monolayer graphene and hBN. In this scenario, the graphene and hBN lattices do not interact.

The difference in lattice constants between graphene and hBN is as low as 0.05 Å when μ is 1.8%. The transition on the graphene lattices is localized at the very small AB-stacked regions for decreased lattice mismatch. Moiré patterns take the role of magnification, which projects the interatomic interaction. Consequently, the image contrast slightly increases in regions of single atoms and decreases in the transition area between the AB- and BA- stacked regions. In other words, the area occupied by distinguishable single atoms increases, which provides evidence of decreased lattice mismatch from image simulations performed by MacTempas software (**Figure 54**).

As the lattice variation is too small to distinguish in the AR-TEM imaging, the corresponding AR-TEM images (**Figure 48(b)**) appear similar with the simulated images. However, small changes in μ become large morphological differences in the moiré fringes, which are reciprocally related to μ; thus, d_{gm} and the width of the moiré fringes also become noticeable.

Several calculation studies have sought the reason for the transition to a commensurate state. G/hBN has different interaction energy between the layers and the in-plane elastic energy depending on the stacking configurations.[57] These different energies alter the interlayer distances and strain distribution (**Figure 37**).[76, 77, 81] Moiré fringes in AA-stacked regions are considered as the pivot points of the moiré fringes because Young's modulus and adhesion energy are highest in these regions. Recently, moiré is twisted on a pivot around the AA-stacked regions in an analytical model of bilayer graphene at low twist angles.[82] On the other hand, moiré fringes of this model exhibit local variation on their widths and corrugation around the AB-stacked regions with the lowest in-plane elastic energy. The low elastic energy triggers transformation on graphene lattices by stretching and local twisting and provokes the transition to commensurate state.

The local morphology variation of the moiré fringes demonstrates that transition to the commensurate state occurs by decreasing lattice mismatch and twisting between the graphene and hBN in the AB-stacked regions. The transition loses the hexagonal symmetry of G/hBN superstructures, generating a graphene band gap.[83] Therefore, the moiré fringe TEM imaging analysis immediately reveals the relation between the local structural variation and electronic properties, even under low magnification. This provides an ingenious insight into the inconsistency between the experimental results and the theoretical research, namely the insufficient band gap opening on the graphene.[74, 84]

3.6| Conclusion

The moiré superstructures of G/hBN were comprehensively studied to demonstrate the relation between the stacking configurations and interlayer interactions through DF-TEM with SAED and lattice fringe analysis on the AR-TEM images. At low twist angles, uneven intensity between the AB and BA stacked regions provides evidence for losing their hexagonal symmetry on the moiré superstructures and moiré fringes depending on the stacking configurations such as widened and zigzagged morphology. These features present local twisting and decreasing of the lattice mismatch as the graphene lattices stretch in the AB-stacked regions; in other words, graphene lattices become similar to hBN lattices, and it indicates local transition from incommensurate to commensurate state at AB-stacked regions. Thus, this work provides insights into the spontaneous interactions between van der Waals 2D materials under free standing state, even under low magnification. To the best of my knowledge, my TEM work is the most comprehensive report to directly demonstrate the reduced lattice mismatch on G/hBN depending on the stacking configuration under not only microscale with moiré fringes but atomic scale with expansion of AB-stacked area. Furthermore, it can provide an inventive route to study van der Waals 2D structures for understanding the outstanding electronic properties in detail.

PART 2. DEGRADATION MECHANISM OF LAYERED CATHODE MATERIALS IN LITHIUM ION BATTERIES

Chapter 4: Cycling-Induced Microstructural Degradation on Cathode Materials

4.1| Introduction

Study on lithium ion batteries (LIBs) has been explosively intensive, which results from their high energy density and widespread applications.[85, 86] LIB is mainly composed of cathode, anode, electrolytes, separator, and current collector. Cathode is the primary factor to determine the capacity, so it is important to avoid detrimental aspects of cathode together with anode such as side reaction with electrolytes and structural disordering of electrode materials. Among the various cathode materials, lithium transition metal oxides have been considered as promising cathode materials on account of their high energy density, which is attributed to the types of transition metals (TMs). $LiNi_{1-x-y}Co_xMn_yO_2$ (NCM) is one candidate among the promising cathode materials due to its high capacity and cost effectiveness compared with $LiCoO_2$ and its potential to adjust capacity depending on the relative ratio of different TM ions.[87] Whereas, there still remain many issues for safety.[88] LIBs have complex degradation mechanism such as detachment of active materials from the metal electrodes, formation of surface reconstruction layer, phase transformation, etc.
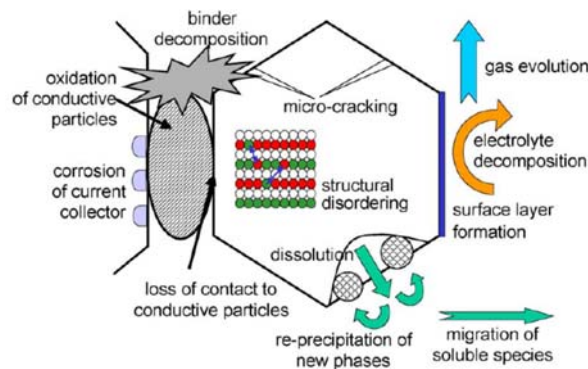
Figure 56. A schematic of deterioration factors on cathode materials.[89]

The microstructure of cathode materials is associated with capacity retention and cycle life of batteries significantly.[90, 91] The cathode materials are spherical few micrometer-sized secondary particles composed of agglomerated submicron primary particles. Surface of the secondary particles surrounded by electrolytes undergoes dissolution of electrode-active materials[92] and forms inert surface layer. Outermost areas of the primary particles are stoichiometrically instable owing to repeated diffusion of

lithium (Li) ions during the cycling. It provokes phase transformation [93-95] and pulverization [96, 97], which becomes exacerbated under accelerated C-rate [98] at elevated temperature owing to increase in extraction of Li from the structure.[99] The phase transformation additionally evokes release of oxygen[100], which leads to a reaction with flammable electrolytes and provokes swelling and explosion.

In the case of nickel(Ni)-rich cathode materials, as the nickel content rises, the capacity becomes higher while the structural stability worsens. It results in a capacity deterioration and poor cycleability and makes commercialization difficult. The structural instability is caused by a migration of TM ions, especially Ni ions to Li sites. This migration can trigger phase transformation from layered ($R\bar{3}m$) to spinel ($Fd\bar{3}m$) and rock-salt ($Fm\bar{3}m$) phase. [101-104] Manganese (Mn) and cobalt (Co) are added to improve the structural stability and cycleability. However, the inevitable lattice distortions at early electrochemical cycles and the oxidation state variation of TM ions have not been studied intensely with atomic resolution. A detailed investigation of the structural evolution at surface demonstrates the degradation mechanisms and provides insights into the surface modification such as coatings for enhancing the structural stability. Comprehensive TEM study can explain that the capacity fade and voltage decay are partially attributed to a structural reconstruction inducing a transition from the layered to spinel and/or rock-salt structures at the surface and/or in the bulk.

In this chapter, I investigate the structural deterioration of $LiNi_{0.6}Co_{0.2}Mn_{0.2}O_2$ (NCM622) layered cathode materials through microstructural imaging analyses with aberration-corrected TEM/STEM and electronic structure analyses with EELS during the repeated cycling.

4.2| TEM Specimen Preparation

Characterization of cathode materials is needed to correlate microstructural changes with electrochemical performance in cycling tests. To study the microstructural changes in cathode materials with TEM, I prepared thin cross-sectional TEM specimens whose thickness was below 100 nm with a focused ion beam (FIB), FEI Quanta 3D FEG. TEM specimens of powdery materials are conventionally prepared by mechanical grinding[105], dimpling[106], electropolishing and jet polishing[107]. However, those are not appropriate for the cathode materials owing to poor site-specific milling, reaction with dispersion solution and risk of separation in the agglomeration. On the other hand, FIB is capable of milling and deposition at specific regions under vacuum, which reduces preparation time and side reaction and leads to great utilization in the device industry.[108, 109] However, the porous materials with rough surfaces involve curtaining artifacts during milling owing to spatial variation of milling rates by gallium (Ga) ions.[110] The Ga ions also penetrate into the internal pores and etch open edges of the primary particles actively due to faster milling rate of Ga at the defective regions.[111]
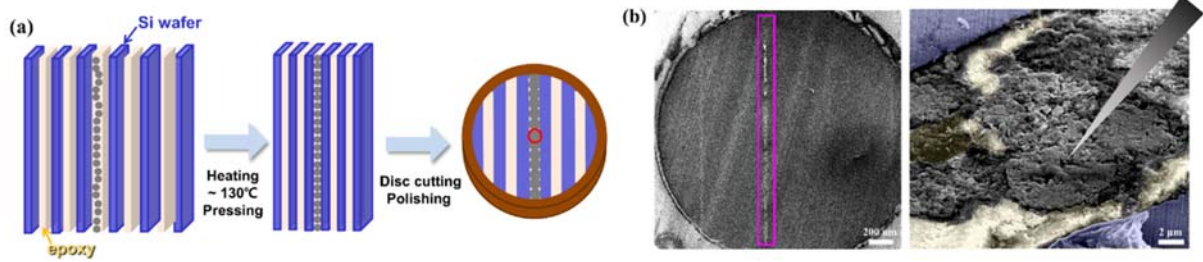
Figure 57. A schematic of specimen preparation procedure before FIB process.

Moreover, the agglomerated NCM cathode materials become less dense by enlarging the pores and fissures during the electrochemical cycling, which makes more difficult to prepare thin TEM specimens using FIB. I propose a noble specimen preparation for high resolution TEM by embedding epoxy to fill in the micro pores. The embedded epoxy is able to retain the internal morphology of the particles and avoid ion-beam damage and contamination by covering the reactive outermost areas where the phase transformation is dominantly occurred (**Figure 57**).
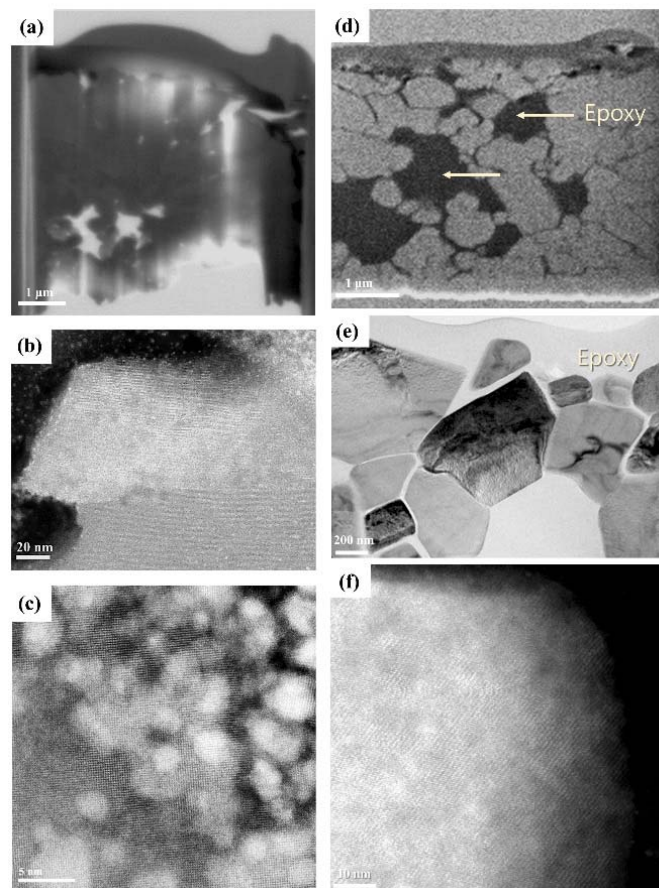
Figure 58. Cross sectional images of porous NCM prepared by FIB without epoxy from (a) to (c) and with epoxy from (d) to (f), respectively.

Figure 58(a) shows the dominantly damaged open edges and the etched active surfaces of the secondary particles during the FIB process. The open edges get larger and larger owing to the curtaining artifacts and they give rise to pores and fissures with serious bending and further perforation on the specimen even before performing fine thinning. A STEM HAADF images of in **Figure 58(b) and (c)** present the seriously contaminated NCM particles at the outermost areas, which hinders TEM investigation of the deteriorated NCM structures.

On the other hand, the cross-sectional image in **Figure 58(d)** shows that the epoxy permeates fully into the few-micrometer-sized pores and few-nanometer-sized fissures between the primary particles. Compared to **Figure 58(a)**, **Figure 58(d)** shows that the permeated epoxy retains the agglomeration of the primary particles without breaking of linkage and perforation between the particles during cross-sectioning with FIB. Furthermore, thin TEM specimen in **Figure 58(e)** shows epoxy-filled agglomerated primary NCM particles and clean NCM-epoxy interfaces. The epoxy can penetrate into not only few-hundred nanometer-sized fissures but also few nanometer-sized ones, which indicates that epoxy plays an appropriate role of passivation on the reactive outer regions of the primary particles and protects the linkages between the primary particles.

As a result, the prepared TEM specimens of NCM have clean interfaces with the permeated epoxy without contamination by Ga ions. It lets us observe readily gradual phase transformation from parent $R\overline{3}m$ to disordered cubic-like $Fm\overline{3}m$ phase at the outermost area ascribed to disordering between TM and Li slabs, which is a primary factor on the incremental irreversible capacity.

4.3| Electrochemical-cycling-induced Structural Transformation

In LIBs, overall cycling performance of the cell is gradually faded as increasing the number of electrochemical cycles. **Figure 59** shows the charge-discharge capacity profile and capacity retention of NCM622. As the number of cycles increases, charge-discharge capacities decrease and the degree of capacity decay at early cycles from 1 to 5 cycles is more severe than that at latter cycles from 5 to 10 cycles and from 10 to 50 cycles. In case of capacity retention, the degree of decrease at early cycles was also larger than that at the late cycles. To investigate the origin of capacity fade, the local structure variations were analyzed with STEM. At first, the primary particles at a low magnification were observed as shown in **Figure 60**. Continuous void expansion and generation of microcrack are evident along the boundaries between primary particles as the number of cycles increases. NCM622 underwent repeated anistropic expansion and contraction during the electrochemical cycles. During the charging process, Li ions are extracted from the lattices of layer-structured material accompanying with oxygen

by forming Li$_2$O phase. This loss of Li and oxygen results in the lattice distortion and breakdown of layered structure.[95, 104]
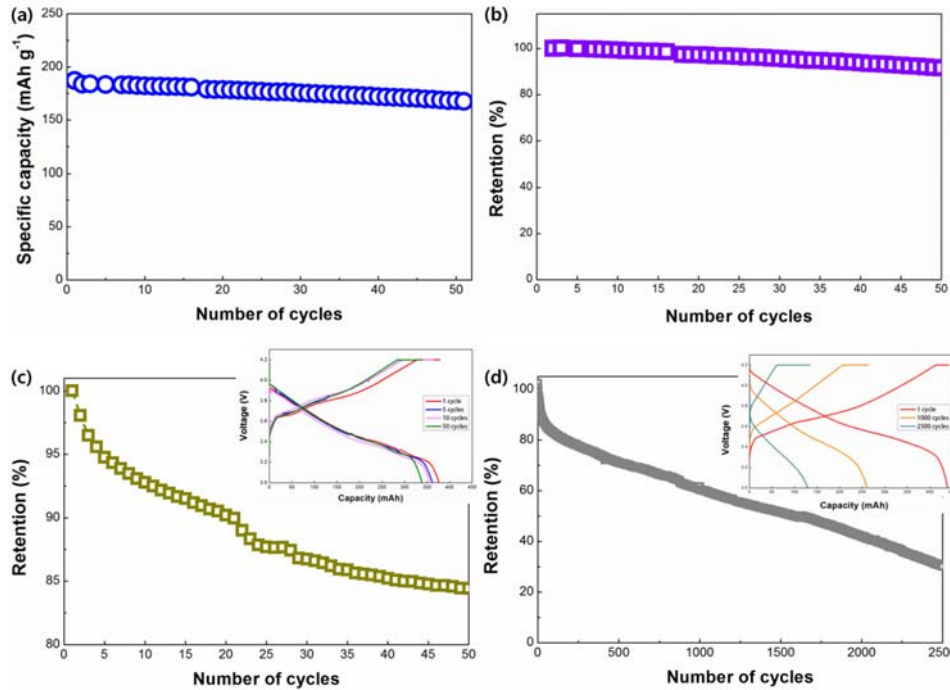
Figure 59. (a), (b) Electrochemical performance data of half cell as increase of the number of cycles. Capacity retention of full-cell for low cycles from 0 to 50 cycles at 0.5 C rate in (c) and for high cycles from 0 to 2500 cycles at 2 C rate in (d). Insets in (c) and (d) are corresponding charge-discharge capacities vs voltage profiles. All cycling performance was evaluated at 60 °C.[112]
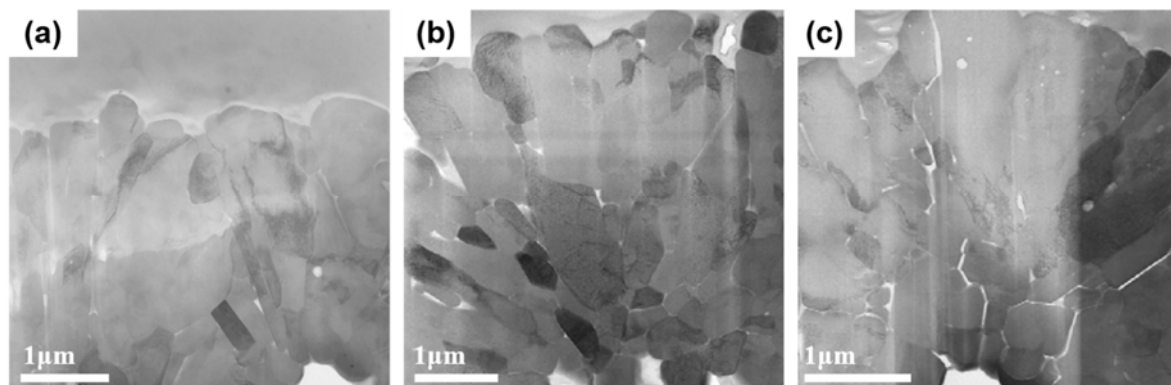
Figure 60. Low magnification cross-section images of LiNi$_{0.6}$Co$_{0.2}$Mn$_{0.2}$O$_2$ (NCM 622) cathode materials representing propagation of cracks and development of micro-sized voids between the primary particles as increase of the number of cycles (a) 0 cycle, (b) 10 cycles and (c) 2500 cycles.[112]

4.3.1| Structural Transformation by Cation Mixing

During the charging process (delithiation), Li ions are extracted from the layered structure and TM ions whose sizes are similar to Li ions can occupy the vacant Li sites to stabilize the structure. This phenomenon causes lattice distortion and nucleates phase transformation through growth of the spinel phase. During the discharge process (lithiation), the extracted Li ions return to their original sites, but partially migrated TM ions prevents Li ions from returning to their original positions. This phenomenon, cation mixing, increases the irreversible capacity and deteriorates the cycleability on account of the blocking of fast diffusion path of Li.[113] It can be considered as the primary factor of capacity fade and voltage decay in lithium ion batteries (**Figure 61**).
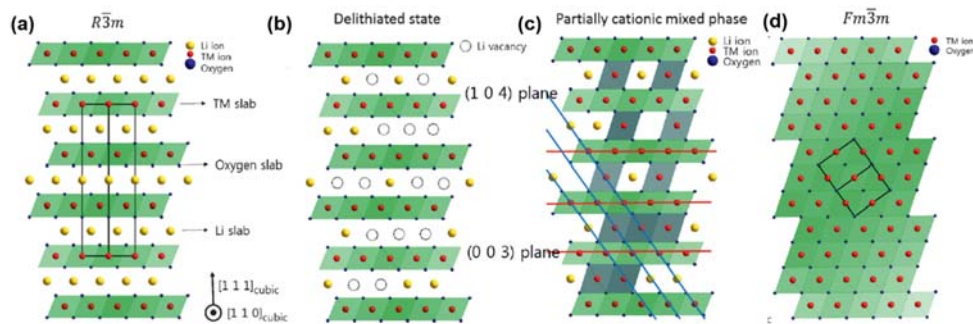
Figure 61. Structural transformation induced by cation mixing in nickel-rich cathode materials.[114]

4.3.2| Change in Electron Diffraction from Layered to Disordered Structure

For investigation on the structural evolution during electrochemical cycles, electron diffraction simulation was carried out with CrystalMaker and MacTempasX.
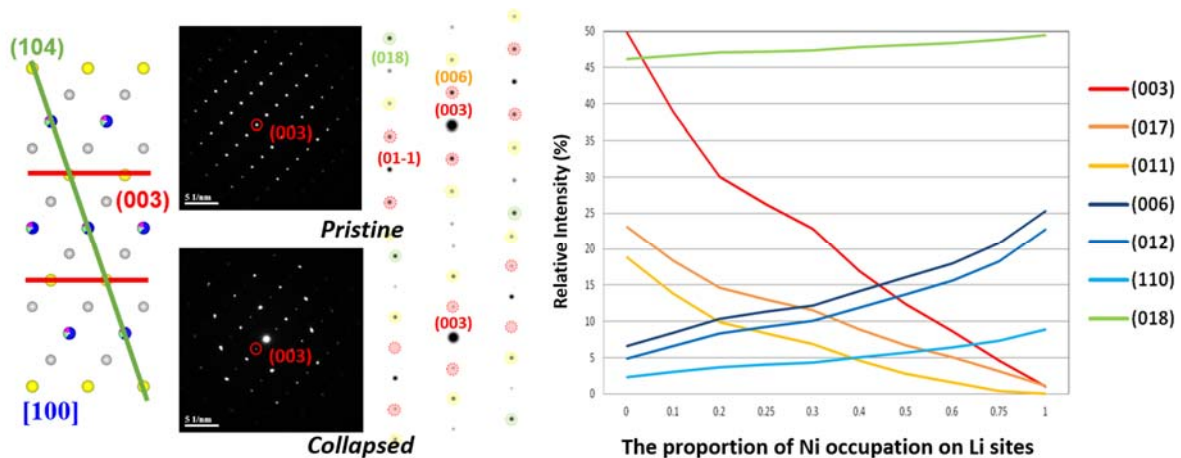
Figure 62. A schematic of variation in the electron diffraction pattern associated with the degree of disordering between Li and Ni slabs.[112]

Figure 62 shows a basic structure of NCM622 as $R\bar{3}m$ (α-NaFeO$_2$) in the repetitive order of TM (3b sites), O (6c sites), Li (3a sites), and O and corresponding experimental and simulated electron diffraction patterns for pristine and completely collapsed states at [100] zone axis. The meaning of the completely collapsed state is the fully delithiated condition in which the TM ions, especially Ni, whose ionic radius (+2 : 0.69 Å) is similar to that of Li (0.76 Å) occupy most of original Li sites. Other TM ions can also occupy Li sites, but the probability of occupancy for Ni ions is much larger than that for Mn and Co ions, so I only considered the case of occupancy for Ni ions. Recently, Yan et al. also confirmed that the cation mixing was mainly attributed to the migration of Ni ions through the EDX analysis. [115] As a result, the whole positions of diffraction spots were not changed, but the intensities of certain diffraction spots decreased and resulted in the decrease of the number of electron diffraction spots. The reduction in the number of diffraction spots is an indication of the formation of the high symmetry rock salt phase of Fm-3m.[101] The graph represent intensity variation of the electron diffraction spots related with that of (014) in accordance with the ratio that Ni^{2+} ions occupy the Li sites, which is simulated by CrystalMaker. It denotes significant decline of the (003) peak intensity, which means random distribution of cations on the 3a (Li) and 3b (Ni) sites of the R-3m. Therefore, the intensity variation of (003) diffraction peak is a characteristic of the cation ordering.[116] In XRD analysis, the value of I$_{003}$/I$_{104}$ corresponds to the degree of cation ordering, so its low value can be interpreted as a non-uniform cation ordering from high cation mixing between octahedral layers.[95, 116, 117]

(h k l)	Perfect [%]	Partial 10 nm [%]	Partial 30 nm [%]
(003)	100	68.53	19.11
(011)	100	8.34	15.59
(017)	100	30.34	51.66
(014)	100	126.96	87.28
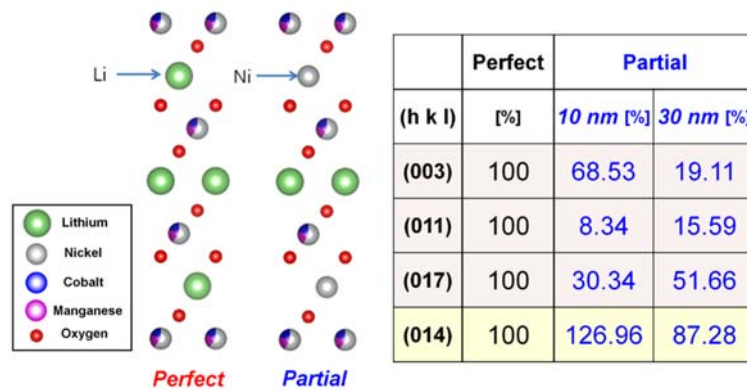
Figure 63. Simulated intensity variations of electron diffraction spots using MacTempasX.[112]

Another simulation was conducted to confirm that the change in (003) reflection sets' peak intensities resulted from the collapsed layered structure with MacTempasX (**Figure 63**). The above partially collapsed structure means that 2/3 Li sites are substituted with nickel (Ni). The table shows that the relative intensity ratio of partially collapsed structure to perfect structure. After (014) was set as standard intensity, I took the relative intensity ratio of electron diffraction spots like I$_{(003)}$/I$_{(014)}$ about each structure and thickness. And then, the relative ratio of partial to perfect structure was taken to represent the decrease in intensities of (003) reflection sets. For example, the ratio of (003) in partially collapsed

structure has 68.53 % in 10 nm and 19.11 % in 30 nm compared with 100 % in perfect structure. It means the intensity of (003) in partial decreases about 32 % in 10 nm and 81 % in 30 nm owing to the structural degradation. In order to rule out the change in the intensity of (104), I attached its variation in accordance with the structure at each thickness. In spite of increase in (014) intensity from perfect to partial structure, (003) reflection sets represented decrease of their intensities. Therefore, the tendency of decease in (003) reflection sets' intensities at 10 nm and 30 nm could proves that the intensity variation in (003) reflection sets is an evidence of the structural degradation.
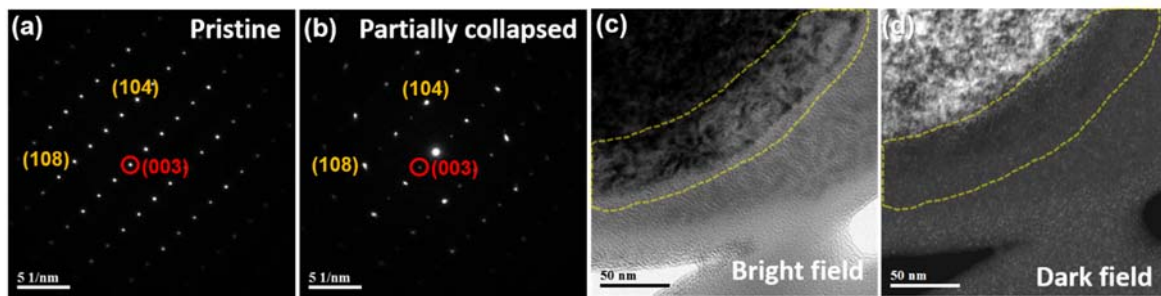
Figure 64. Electron diffraction patterns of NCM 622 (a) in interior and (b) in surface region of the primary particle. (c) Bright field TEM and (d) DF-TEM image corresponding to the (003) peak.[112]

In order to demonstrate that the (003) peak is crucial to do investigation of the structural degradation under not only simulation but also experimental analysis, selected area electron diffraction pattern (SAED) and DF-TEM technique were performed on NCM622 (**Figure 64**). There is a big difference in (003) peak between strong intensity of interior region and weak intensity of surface region. At the interior region, the electron diffraction pattern indicates rhombohedral structure (R$\bar{3}$m) at the [100] zone axis. The crucial (003) peak, which determines the cation ordering, shows strong intensity, which well matches with electron diffraction simulation. But in the vicinity of the surface region, it has much dimmer intensity. This can be interpreted as non-uniform cation ordering and the collapse of layered structure. To directly show that (003) peak is crucial for structural degradation in a real image, the DF-TEM technique was applied. DF-TEM images are mainly formed by the contribution of a selected diffracted beam, not by a directly transmitted beam, so its contrast has an inversion of the bright field TEM (BF-TEM) image. The dark intensity at the surface region indicated by the yellow dashed line in the BF-TEM image represents that the surface region is composed of cathode materials. Unlike the BF-TEM image, the DF-TEM image taken from the (003) diffraction does not have a bright intensity at the surface region marked as a yellow dashed line, which corresponds to the absence of (003) diffraction in **Figure 64(d)**. In other words, this indicates non-uniform cation ordering and the collapse of the layered structure at the surface region.
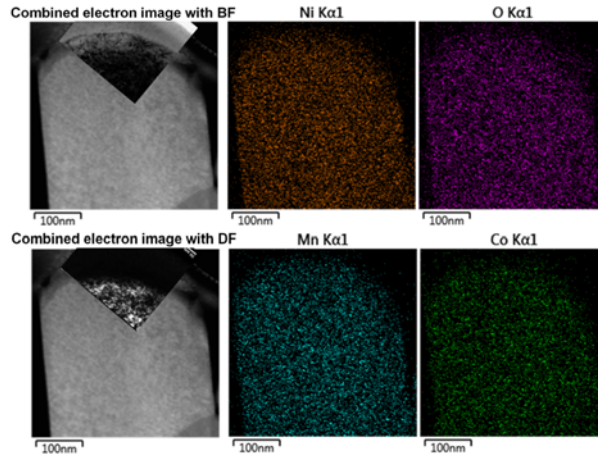
Figure 65. EDS elemental maps of Ni, Co, Mn, and O.[112]

Energy dispersive spectroscopy (EDS) elemental maps combined with BF & DFTEM images at a low magnification shows that the edge region is composed of NCM622 as shown in BF image and EDS map. But in the DF-TEM image taken at (003) peak, the edge region has no intensity, which can be interpreted as a collapse of cation ordering and layered structure at the surface region.
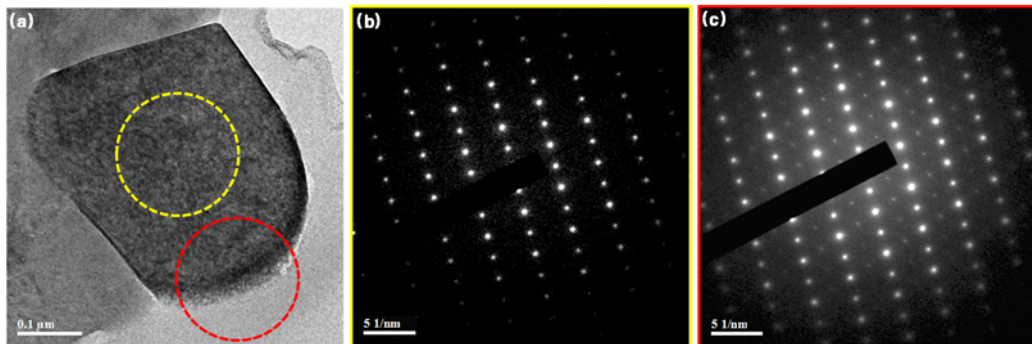
Figure 66. Electron diffraction patterns of NCM 622 after 10 cycles at (a) diffraction pattern survey image. (b) Well-ordered rhombohedral phase (c) Disordered structure toward spinel-like phase.[112]

It is known that the layered cathode materials are thermodynamically prone to transformation into the spinel phase when the Li content is reduced about 60% from the original Li content in the layered structure.[118] As the number of cycles increases, the Li content in surface region is reduced more and more and triggers phase transformation from the layered ($R\bar{3}m$) to the spinel structure ($Fd\bar{3}m$).[104] **Figure 66** represents coexistence of rhombohedral and spinel phase. There are additional spot arrays between rhombohedral electron diffraction coming from the phase transition to the spinel phase. Therefore, the DF-TEM technique can be utilized effectively to verify localized microstructural changes at the surface region even if a low magnification.

4.3.3| Dominant Microstructural Deterioration at the Interface with Electrolytes

To investigate microstructure in detail, HRTEM image analysis was performed. HRTEM/STEM imaging analyses and EELS were carried out using a probe Cs corrected JEM-2100F at 200kV. Among many of primary particles in cross section of secondary particles, I mainly chose ones at the outermost of secondary particles contacted with the electrolytes and participating in electrochemical performance during cycles. **Figure 67** shows an HRTEM image after 5 cycled at surface region where directly in contact with electrolytes. It is reseparated to three areas in accordance with structural degradation with the corresponding digital diffractograms (FFTs). It appears that the structural degradation is locally concentrated on the surface region and it is much more severe toward the interface with electrolytes. In the FFT results, both (003) and (006) reflections sets have bright intensities in the interior region, whereas only (006) reflection sets are bright at the surface region whose intensities change very little with microstructural changes. The (003) reflection sets which are indexed as red became dimmer from the interior to the near surface region. It indicates a random distribution in the 3a (Li) and 3b (TM) sites of the $LiTMO_2$ ($R\overline{3}m$) structure. The first FFT and corresponding region 1 (yellow region) represent well-ordering layered structure of R-3m. But the second FFT and corresponding region 2 (green region) show a coherent interface between the surface and the interior region, which indicates the presence of a partially collapsed structure resulted from the partial occupancy of Ni ions in Li sites. The last FFT in region 3 has no intensities of (003) reflection sets, so it can be interpreted as having a close to fully collapsed structure and a starting point for phase transformation from rhombohedral to spinel structure.
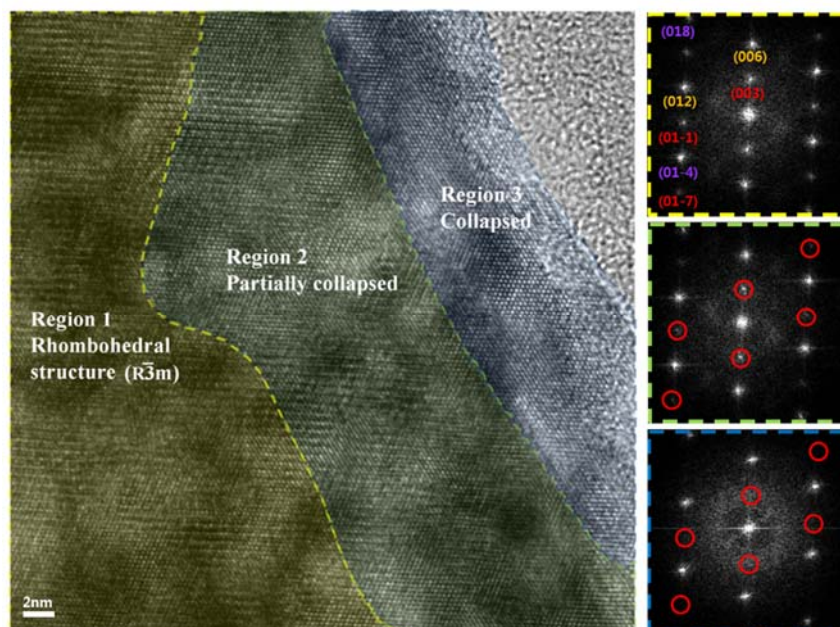
Figure 67. A HRTEM image with corresponding FFTs representing gradual structural degradation in NCM622 after 5 cycled.[112]
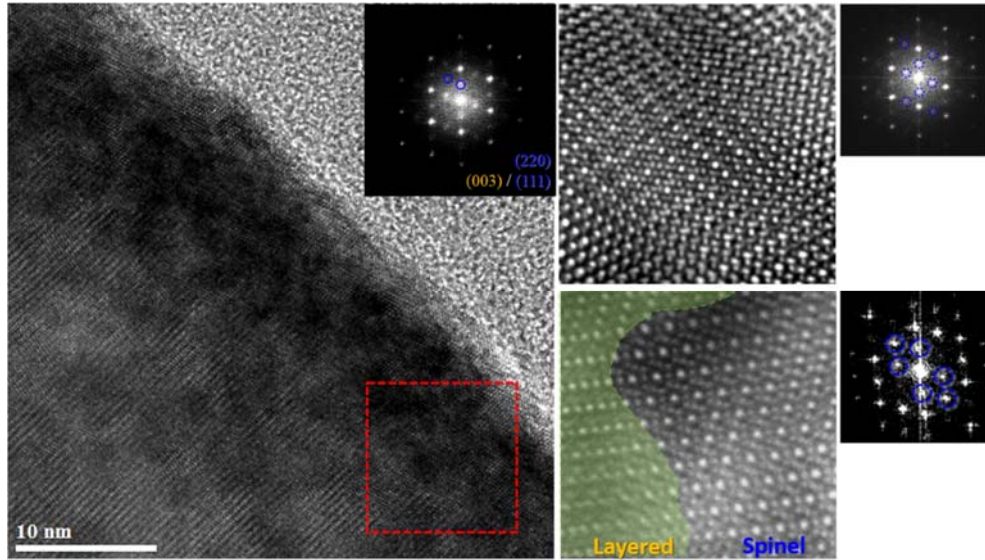
Figure 68. HRTEM images for phase transformation from rhombohedral to spinel phase in NCM622.

If phase transformation to spinel phase has occurred, new diffracted reflections appear, which indicated by blue circles (**Figure 68**). They are consistent with the SAED results in **Figure 66(c)**. Moreover, HRTEM/STEM images also represent coherent growth of the spinel on the layered structure by phase transformation due to repetition of electrochemical cycles.
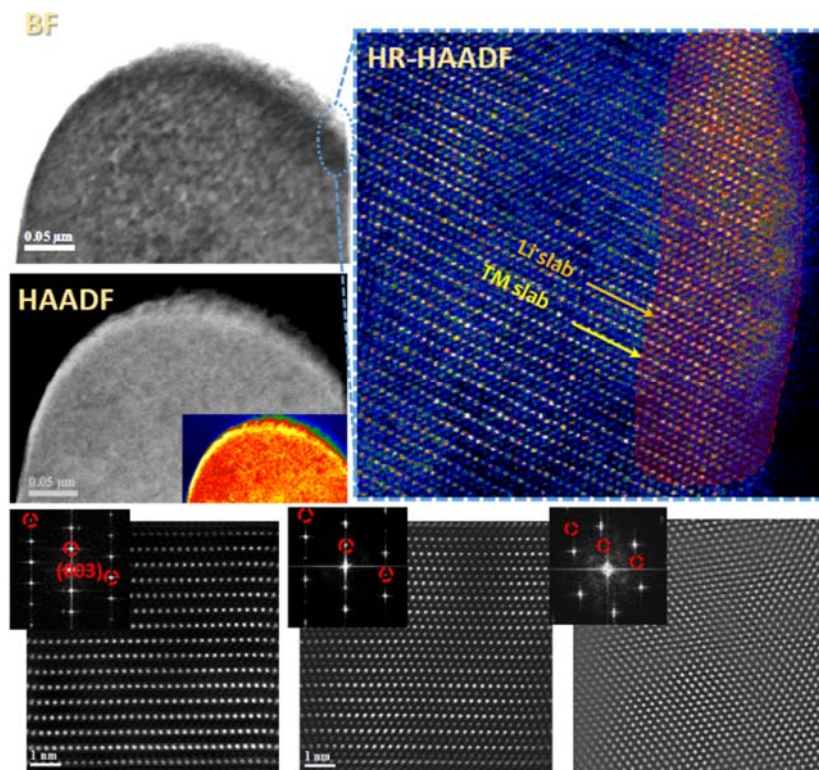
Figure 69. HRSTEM analysis of structural degradation of NCM622 after 10 cycled.[112]

While bright field imaging in STEM mode features dark contrast at the surface region caused possibly by small differences in crystallographic orientation or composition, HAADF imaging characterizes Z-contrast dependence (approximately Z^2 dependence, Z means the average atomic number of an atomic column), so the bright contrast in HAADF dominantly result from the heavier atomic columns (**Figure 69**).[119] HAADF image shows a much brighter intensity at the surface region. The inset is a colorized image to show clearly the contrast gradient, which means heavier atoms are segregated at the surface region.[120] The contrast difference at the surface region can be observed in a high resolution HAADF image. The red-overlaid atomic columns are of heavier atomic columns consisted of TM slabs. Since Li is a light element, its atomic columns have no visible contrast in the HAADF imaging. But at the surface region, the contrast between Li slabs becomes brighter, which can be interpreted as not from the Li, and instead from other heavier TM atoms. The below high-resolution images also show gradual structural degradation with their corresponding FFTs. This phenomenon results from selective disordering between Li and TM ions at certain surface regions and grain boundaries to stabilize the structure. It could increase the irreversible capacity and the capacity fade by blocking the fast diffusion path of Li ions, caused by the formation of insulating layers as transition metal oxide at the surface.

4.3.4| Determination of Structural Deterioration Induced by Repeated Electrochemical Cycling

Based on HRTEM/STEM imaging analysis, the microstructural degradation especially at the surface was analyzed further.
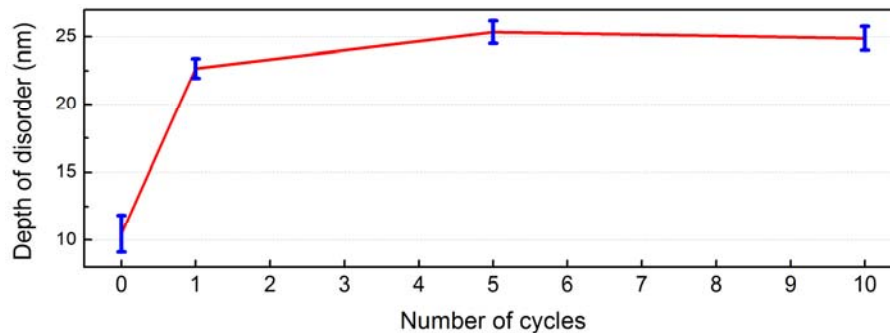
Figure 70. A graph of depth of disorder at the surface of the NCM 622 as a function of cycles.[112]

The degree of structural degradation is analyzed according to the number of cycles and correlated with the drastic decline of capacity retention and capacity fade (**Figure 59**). At the early cycling stage, the structural degradation is concentrated on the surface regions. Thus approximately 100 different surface regions per cycle were analyzed to get statistical results. For high reliability of statistic results, I only selected interface regions directly in contact with electrolytes where most primary particles participate in electrochemical performance, so it is appropriate to correlate structural degradation with

electrochemical performance at the early cycles. But, chemical reaction with electrolytes leads to formation of large inevitable degradation depth in non-cycled pristine cathode materials about 10 nm. As the number of cycles increases, the average depth of degraded structure increases. The large standard deviation results from anisotropic characteristic of surface reconstruction, which predominantly occurs along Li diffusion layers.[118] Judging from the results in the graph of **Figure 70**, the degree of disordering is especially severe at the early cycling state from pristine to 1 cycle. **Figure 59 (c) and (d)** also present that the capacity retention and charge - discharge capacity fade at the early charge - discharge process is more severe than that at latter cycling states. Thus, the degradation depth can be considered as one major factor on the capacity and voltage fade at early cycles.

4.4| EELS Analysis of Change in Oxidation States of Transition Metals Ions After 1st Electrochemical Cycling

Compositional analyses of EELS are sensitive to small change of 3d orbital occupancy of TM, so EELS can explain the alternation of electronic properties of NCM622 resulted from microstructural changes if it is difficult to be observed with imaging analysis at the early cycling stage. TM L-edge comes from the dipoles of allowed transitions from a 2p orbital to an unoccupied 3d orbital. The L_3/L_2 intensity ratio of the TMs increases between $3d^0$ and $3d^5$ and decreases between $3d^5$ and $3d^{10}$, so it can be utilized to estimate the oxidation state indirectly.[121-125] For example, in case of Fe whose 3d occupancy is $3d^6$, if the white line ratio increases, it can be described as that it is oxidized from large 3d occupancy as a low oxidation state like +2 to small 3d occupancy as a high state like +3. But the change of oxidation state accompanies a peak shift moving to higher energy loss if the oxidation state is changed to a higher state.[122, 126]

For EELS study, it is necessary to get the high energy resolution to resolve the O K-edge and TM (Ni, Mn, and Co) L-edges and to investigate the fine edge structures, which was about 0.9 eV in my experimental condition. The intensity of Mn L_3 edge decreased from the surface to the interior region and its peak showed blue shift as shown in **Figure 71 (b) and (d)**. The L_3/L_2 intensity ratio calculated by the Pearson method (*method 2*) increased from 2.41 at the interior (green) to 3.96 at the surface (red) region and the ratio calculated by the maximum intensity method (*method 1*) also represented an increase. The increase of the L_3/L_2 intensity ratio can be interpreted as having lower oxidation states at the surface region. The oxidation state of Mn can be estimated from the +2 at surface region to nearly +4 at the interior region.[127-129]

In contrast to Mn, intensity of Ni L_3 edge decreased from the interior to the surface, but there is no significant peak shift. But, the L_3/L_2 intensity ratio decreased from 3.88 in the interior to 3.0 in the

surface region. From the change of ratio, it appears that Ni oxidation state is reduced slightly from high valence to low valence state as close to surface region.[130]

The intensity of prepeak of O K-edge measures the transition from O 1s to O 2p - TM 3d hybridized state, so it is indicative of the number of unoccupied states projected at the O atom. The O-K onset energy also has a relationship with TM oxidation state like that it shifted to low energy as TM oxidation state increases.[122, 131] In other words, it is sensitive to the oxidation states of TM ions, so it can be used to estimate the average oxidation states of TM ions. In my results, intensity of this peak decreased by accompanying with the shift of the O-K onset energy to high energy loss toward surface region so the average oxidation states of TM decrease.[132]

(d)

Mn	L_3/L_2_1	L_3/L_2_2	L_3 (640eV)	L_2 (651eV)	L_3-L_2 (11eV)
🟥	1.604	3.958	640.3	651.4	11.1
🟦	1.380	3.816	640.9	652.6	11.7
🟩	1.209	2.405	642.1	654.1	12

Ni	L_3/L_2_1	L_3/L_2_2	L_3 (855eV)	L_2 (872eV)	L_3-L_2 (17eV)
🟥	1.28	3.0	853.9	871.6	17.7
🟦	1.481	4.73	853.9	871.6	17.7
🟩	1.458	3.88	854.2	871.9	17.7

(e) **Quantification Results**

	$O_\square/O_\blacksquare$ (529.8-553.8eV)	$Mn/O_\square$ (641.4-662.4eV)	$Ni/O_\square$ (854.1-881.1eV)
🟥	0.915	0.139	0.218
🟦	0.959	0.165	0.184
🟩	1.000	0.154	0.279
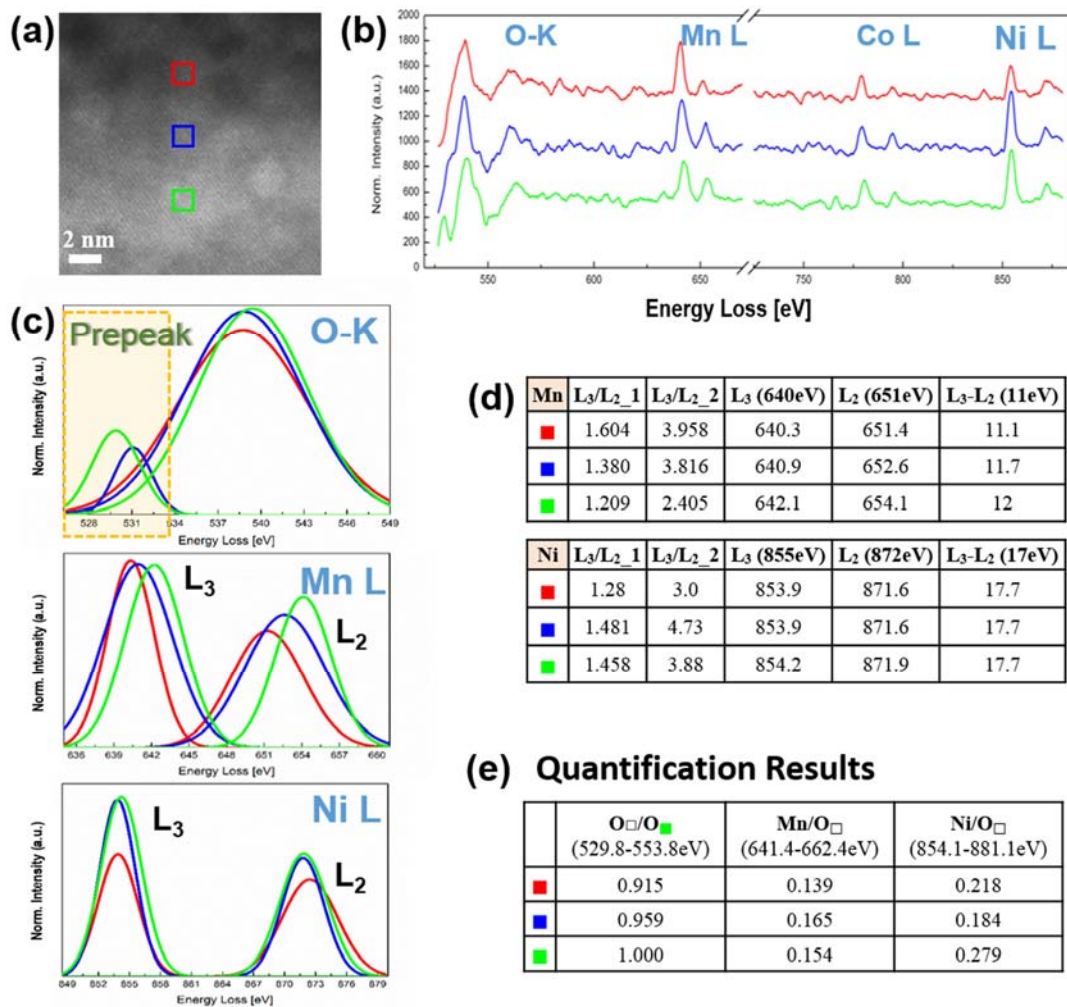
Figure 71. EELS analysis of NCM622 after 1st cycling. (a) A survey image indicating that direction from red to green rectangle is related with that from surface to interior region. (b) Stacked EEL spectra corresponding to the selected areas in (a). (c) Stacked EEL spectra of oxygen K edges and L_3 and L_2 edges of Mn and of Ni (d) Information on EEL spectra associated with L_3 and L_2 edges of TMs for Mn and Ni. (e) Quantification results of O, Mn, Co, and Ni as relative ratio.[112]

The general oxidation state of Ni is +2, that of Co is +3, and that of Mn is +4 with partial distributions of Ni^{3+} and Mn^{3+} ions in $LiNi_{1-x-y}Co_xMn_yO_2$ cathode materials.[133] The +2 oxidation state in Ni is very stable and it can cause cation mixing easily. To account for a relation of local stoichiometric instability with structural transformation after cycled, the EELS quantification was performed based on the Hartree-Slater cross-section model and the background subtraction was based on the power-law. It appears that the relative areal density of O K edges between selected areas and the relative ratio between Co and O increase from the surface to the interior region. This compositional variation appears to be from chemical reaction with electrolytes during electrochemical cycling. This chemical reaction at the interface can accelerate oxygen loss by forming Li_2O phase and develop delithiation at the surface region. This phenomenon leads to the migration of Ni^{+2} ions to vacant Li sites by forming more vacant Li sites. It could be clarified with that the relative composition between Ni and O. The red region (surface) was larger than the blue region in spite of less thick.

The increase in the degree of delithiation affects the 3d occupancy in lithium transition metal oxide.[103] Graetz et al. explained the relation that 3d occupancy decreases from 7 to nearly 6.7 as an increase of delithiation in $Li_{1-x}Ni_{0.8}Co_{0.2}O_2$.[124] In other words, the decrease of 3d occupancy makes an increase in the L_3/L_2 intensity ratio in case of Ni. In my results, there was the large change in the L_3/L_2 intensity ratio from 4.73 in blue to 3.0 in red region. The decrease of the ratio in Ni is described as the increase of 3d occupancy, which means reduction. But there is no significant peak shift closely related with change in chemical state. It appears that the reason is from the cation mixing. The cation mixing is mainly from the migration of Ni^{2+} ions to Li sites, not mainly from the change of oxidation states from oxidization or reduction.

Thus, the chemical state of Ni is not changed and maintain as +2 even though the composition and the white line ratio of Ni are changed due to cation mixing. To compensate the instability of stoichiometry due to the movement of Ni^{+2} ions, the oxidation states of Mn are changed; the increase of L_3/L_2 intensity ratio and the blue shift toward surface region are indicative to lower oxidation state as close to +2. The change of oxidation states of Mn is also supported by the change of prepeak of O-K edge. There are no evident intensities of prepeak of O-K edge at red and blue region. But green region represents striking intensity, which is interpreted as that this region has the higher oxidation states. Thus, the intensity of prepeak of O-K edge is much more correlated with Mn's oxidation state even though the proportion of Ni as 60% is much larger than that of Mn as 20%.

EELS results let us know that Li deficiency in surface region of NCM primary particles is not solely dependent on the Ni. Other TMs, especially Mn also have gradient of oxidation state, which is affected by the non-uniform Li distribution. Localized concentration of Ni^{2+} ions at the surface region makes 3d occupancy change and results in a change of the white line ratio in spite of no significant peak shift. This concentration causes a structural instability due to the increase of non-stoichiometry. To

compensate for it, Mn ions change their oxidation states and this can be observed by peak shift and the change of the L_3/L_2 intensity ratio. Therefore, the changes in electronic structures are largely associated with the lattice reconstruction which is from collapse of layered structure and transformation to the spinel structure.

4.5| Conclusion

In summary, the degradation mechanism of NCM622 cathode materials is investigated by electron diffraction simulation, microstructural imaging and spectroscopic analyses with aberration-corrected TEM/STEM. The (003) peak intensity decreases at the surface region where structural evolution is dominant. Larger Li vacancy formations at the surface promote movement of Ni ions, which occupies vacant Li sites and results in the disordering of layered structure. The structural degradation is accelerated with the increase of the number of cycles and triggers phase transformation from rhombohedral to spinel phase. The average degree of structural degradation at early cycling state is much more severe than that at latter cycling and it can be correlated with the rapid decline of charge - discharge capacity and of capacity retention. HAADF STEM images can show the selective segregation of TM ions at the surface region clearly and represent microstructural evolution from high resolution lattice imaging. Through the spectroscopic analyses with EELS, the local microstructural change leads to alternation of the oxidation states of TMs. Local enrichment of Ni^{2+} ions at the surface region develops the stoichiometric instability, so as to compensate for it, the oxidation states of Mn is changed from +4 to near to +2. The present microstructural study of TEM analysis provides a fundamental understanding of structural and chemical evolution affecting the electrochemical behavior of LIB cathodes as well as an insight to surface engineering.

Chapter 5: Reaction Between Electrode Materials and Electrolytes

5.1| Introduction

Electrolytes take a role of medium for Li diffusion mostly as a liquid phase. It is potentially flammable under certain abuse conditions.[134] Parasitic reaction with electrolytes leads to inferior surface stability of the electrode by structural transformation in conjunction with loss of oxygen and volumetric expansion, which is particularly severe at elevated temperatures. Oxidative decomposition of electrolytes on the surface of electrode brings about high capacity loss and poor cycling ability. The surface reconstruction, on the other hand, suppresses further structural degradation and hinders electrolytes decomposition.[135] In this chapter, I study the reaction between electrolytes and cathode materials and also the effect of the types of electrolyte additives on microstructural transformation of cathode materials using TEM/STEM.

5.2| Reaction Between Electrolytes and Cathode Materials

In LIBs, Li ions move between cathode and anode through the ionic liquid-based electrolytes during electrochemical cycling. There are parasitic reactions between the electrode and the electrolytes inevitably, which is responsible for ageing in LIBs. For example, solid electrolyte interphase (SEI) and solid permeable interface (SPI) is formed on the surface of the anode and cathode by the side reaction with electrolytes, respectively. They take a role of protecting electrode decomposition, whereas, they bring about high capacity loss and deteriorating long-term cyclability. In order to overcome drawbacks for safety and irreversible capacity, electrolyte additives are currently suggested and become an important research owing to high economic efficiency.[136]
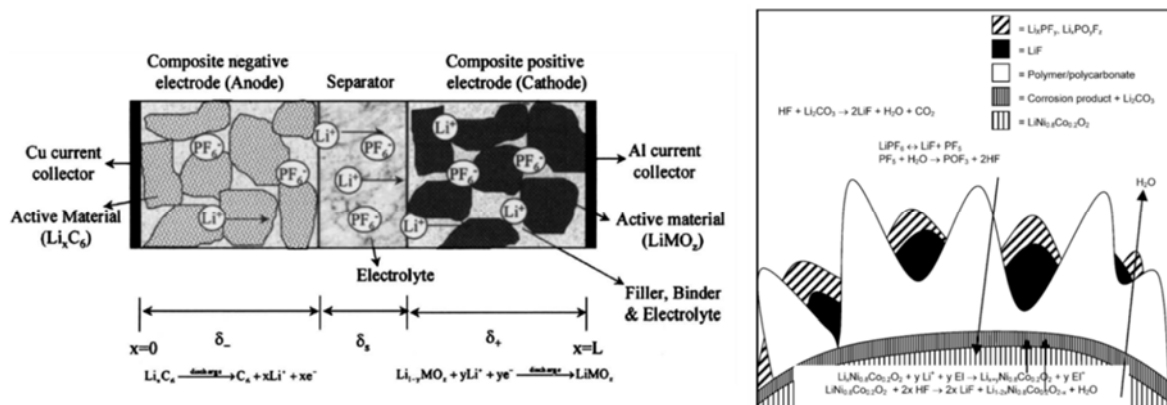
Figure 72. Parasitic reactions between electrode and electrolytes for ageing in LIBs.[91]

Among the various electrolyte additives, propane sultone (PS) is a well-known additive that improves the long-term cycling performance of Li-rich cathode materials. Another additive as vinylene carbonate (VC) forms a very thin film on the electrode's surface to inhibit solvent decomposition and reduce the resistance of the battery cell. On the other hand, it has not been intensively established to investigate how to deteriorate the microstructure of cathode materials depending on the types of the electrolyte additives. The purpose of this chapter is to examine and compare the electrolyte additives in terms of the structural transformation of cathode materials.

5.3| Dependence of Additives in Electrolytes on Microstructural Deterioration of Cathode Materials
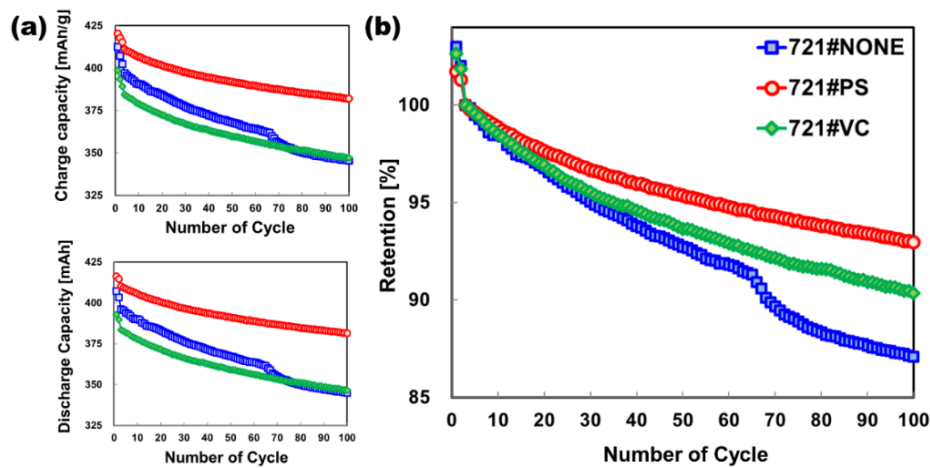
Figure 73. (a) The charge and discharge capacities and (b) capacity retention of $LiNi_{0.7}Co_{0.2}Mn_{0.1}O_2$ (NCM 721) in accordance with the electrolyte additives; blue, red and green is for without additives, 2% PS and 2% VC, respectively.

Figure 73 shows different electrochemical performances of NCM 721/graphite full cell system, depending on the types of the electrolyte additives as a function of the number of charge-discharge cycling. $LiNi_{0.7}Co_{0.2}Mn_{0.1}O_2$ (NCM 721) with 2% propane sultone (*PS*) shows the highest charge and discharge capacity and the best capacity retention; 382.05 mAh, 381.40 mAh, and 93 % respectively (red lines). On the other hand, NCM 721 with 2% VC (*VC*) shows inferior ones; 347.08 mAh, 346.42 mAh, 90% respectively (green lines). NCM 721 without the additives (*None*) shows the most inferior cycling performances; 345.45 mAh, 344.89 mAh, and 87% respectively (blue lines). The present electrochemical performances of NCM 721/graphite full cell system are in good agreement with the NCM 622/graphite full cell system depending on the types of the electrolyte additives.[137] Sulfone-type additives enhance surface stability by forming a passivation film on the surface of the Ni-rich cathode

materials, as a result, they suppress swelling and metal dissolution in conjunction with a loss of oxygen. It means that PS is appropriate to control the surface properties of NCM-based cathode materials by inhibiting electrolyte decomposition and improving the surface stability, which directly influences the interface characteristics of the battery system.

To examine the impact of the electrolyte additives on the morphology and microstructure of the NCM 721, the cycled NCM 721/graphite pouch cells were dismantled and washed, and then, cross-sectioning was carried out using FIB.
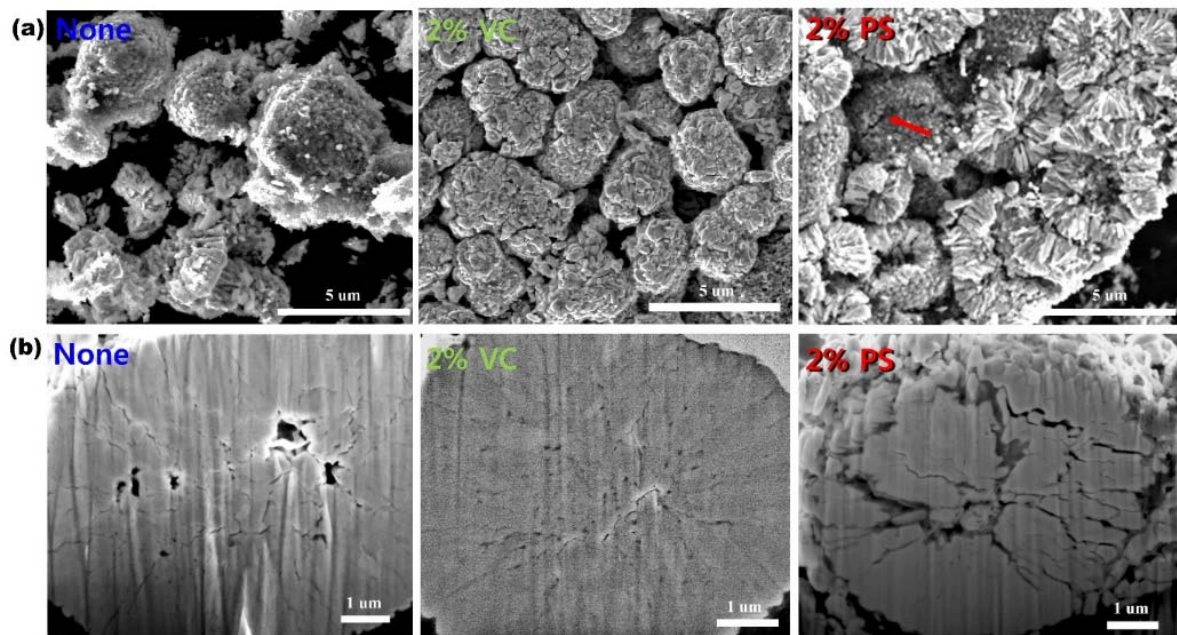
Figure 74. The different morphologies and cross-section of the secondary particles of NCM 721 depending on the types of electrolyte additives after 100th cycled.

Figure 74 represents different morphologies of NCM 721 depending on the types of the electrolyte additives after 100th cycled. *None* shows fragmented secondary particles in part, but some of them maintains their spherical morphology. The cross-sectioned image shows submicron pores and few-nanometer-sized fissures between the primary particles and outward propagation of the fissures.

In the case of *VC*, fragmentation is significantly suppressed without exposing the inner secondary particles. The cross-section of the *VC* displays the low density of the fissures and cracks, whereas, high density of the nano- pores between primary particles, which indicates weak volumetric changes in the primary particles.

PS experiences serious morphological changes in the primary and secondary particles, whereas, it has the best capacity retention and the highest charge-discharge capacities. Most of the secondary particles lose their spherical morphology and agglomeration are significantly collapsed with severe fragmentation, which leads to exposing the primary particles resided in the interior of the secondary particles to reactive electrolytes. Even though the secondary particles keep their spherical morphology, there are micro-cracks on the surface and also on the cross-section of the secondary particles. The high density of the cracks in the secondary particles indicates that the cracks have synergistic effects on the fragmentation of the primary particles.[138]

Crack generation and fragmentation have been intensively attracted to demonstrate the degradation mechanism with respect to capacity fading and irreversible capacity during repeated electrochemical cycling. Fragmentation has been considered as a primary factor by disconnecting the Li paths between the primary particles. It leads to increases in the rate of heat generation, the irreversible capacity and thermal instability, and a decrease in the rate capability.[138] Interestingly, this approach is in contrast to my experimental results. HR-TEM is appropriate to investigate the microstructural phase transformation and the mechanism of crack formation.
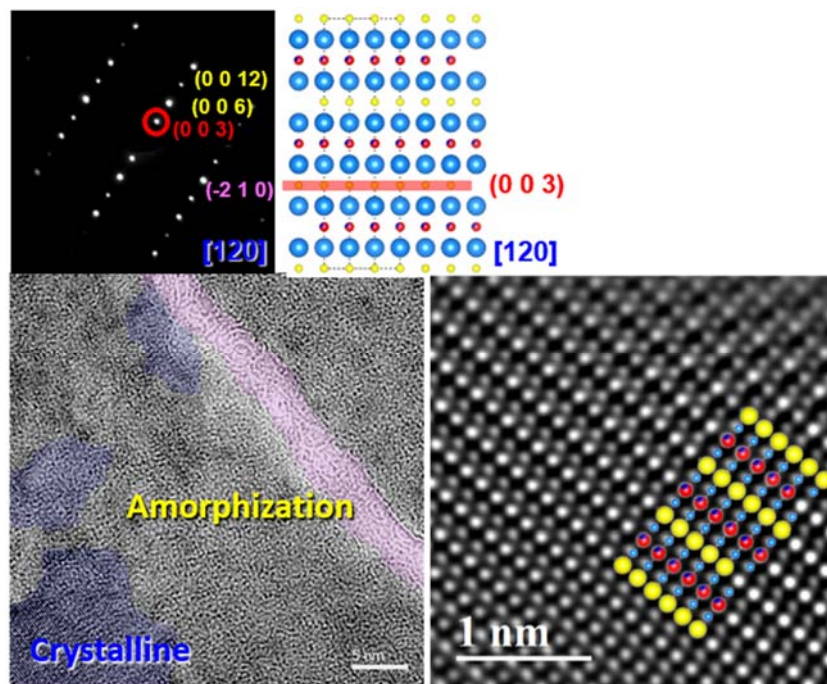
Figure 75. HRTEM characterization of NCM 721 with VC in electrolytes.

In the case of *VC*, there are few fissures and cracks between primary particles caused by lattice breathing and electrochemical fatigue below 500 nm (**Figure 74**). The SAED pattern analysis was conducted at the outermost of the primary particle (**Figure 75**). As microstructural ordering is

deteriorated, the (003) diffracted reflection becomes dimmer which is indicative of structural disordering.[112] *VC* shows the bright intensity of the (003) diffracted reflection, which indicates well-ordered layered structure along the [210] zone axis. On the other hand, a HRTEM image of primary particles shows coherent interface between crystalline and severely amorphous area. The magenta line is grain boundaries where the electrolyte could permeate and react with inside primary particles by forming reactive surface area. The dominant amorphization at the grain boundaries appears to result from the reaction with electrolytes. The crystalline area also shows seriously deteriorated phase by intermixing between Li and TM ions.
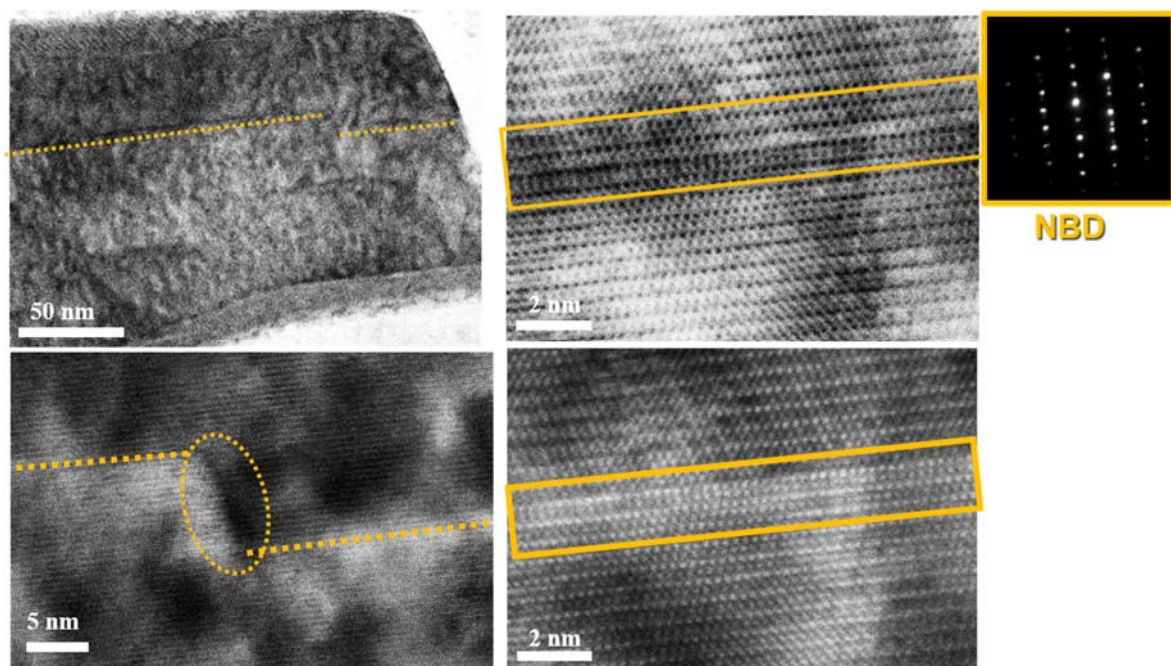
Figure 76. Generated intragranular cracks in NCM 721 with PS and *none*.

PS shows many fissures and cracks between primary particles and so do *none* at some regions (**Figure 74**). The cracks disconnect the Li paths and exert a synergistic effect on fragmentation of the secondary particles. On the contrary, it could give a direct path where the electrolytes react with the active NCM 721, in other words, it expands the reactive surface area.[139] To account for the origin of the cracks in terms of electrochemical-cycling induced microstructural transformation, crack characterization was conducted using HRSTEM.

Interestingly, intragranular cracks appear from the outside region in the primary particles and there is no amorphous region. It appears that the cracks are similar to twin boundaries with incoherent mirror planes. In addition, the primary particle maintains rhombohedral structures as R$\bar{3}m$ even at the

primary particles resided on the outermost of the secondary particles with weak lattice breathing. If the strain generated during repeated charge-discharge process cannot be compensated through the structural transformation from $R\bar{3}m$ to spinel-like and cubic, the links between primary particles are weakened, which should expand the gaps between primary particles and generate intragranular cracks, then, it leads to fragmentation of secondary particles.

In the case of olivine structure of the LiFePO$_4$, twin-like phase boundaries are generated at the interface LiFePO$_4$/FePO$_4$ caused by the internal high strain due to lattice breathing, in other words, inhomogeneous volumetric change during lithium extraction/insertion process in the particles[140]. Dislocations generated during synthesis also become active and take a role of a premature crack during cycling.

5.4| Conclusion

The additives in electrolyte impact microstructural transformation of NCM 721 cathode materials significantly. After 100th electrochemical cycling, PS seriously fragments the secondary particles and generates serious fissures and cracks between primary particles, on the other hand, it shows the best cycling performance. PS maintains rhombohedral structures as $R\bar{3}m$ even at the primary particles resided on the outermost of the secondary particles. Whereas, VC shows less fissures, on the other hand, serious amorphization caused by a reaction with electrolytes. Although it is needed to study on the unique feature of intragranular crack further, in view of the results so far, it is deduced in a straightforward manner that maintaining original layered structure is much important in the aspect of electrochemical performance, even though the cracks are generated inside and they lead to fragmentation of agglomerated cathode secondary particles. If the fragmented particles maintain their original structure, it could take part in electrochemical cycling and leads to better performance.

Chapter 6. Concluding Remarks

This thesis aims to study the local structural transformation in layered materials from low-dimensional to bulk materials through TEM based analyses. The layered materials compacted by weak van der Waals interaction are easy to interact with other elements by intercalation and to experience the structural transformation. In addition, the periodic layer-by-layer assembly makes the locally transformed structure light up, which facilitates TEM characterization. A classical analytic TEM technique of dark-field imaging enables the investigation on structural and chemical evolution, the local structural transformation of low dimensional materials, and the local phase transformation on bulk layered materials, from a few nanometers to micrometer scale. The development of aberration correctors with monochromator enhances imaging resolution and energy resolution respectively at the low accelerating voltage below 80 kV. It makes it possible to study the local structural transformation at the few-nm region.
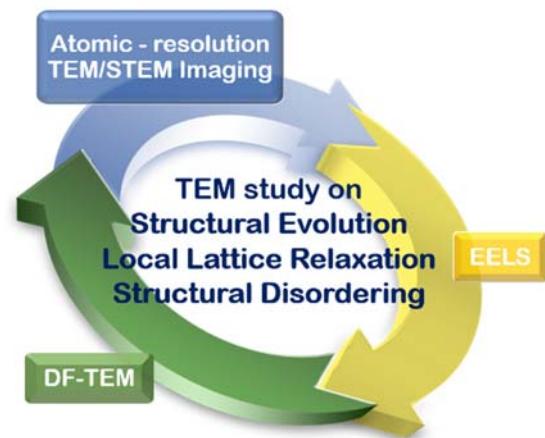
In the field of low-dimensional layered materials in part 1, I provided studies on the structural evolution of graphene oxides and a multilayer graphene system by heat treatment at first. The imaging analyses of DF-TEM and AR-TEM with spectroscopic analysis of EELS demonstrate that they experienced the carbonization and graphitization and transformed into well-compacted hexagonal-lattice-layer stacking by reorganizing their lattices and bonding configurations. The transformed materials are composed of stacked homogeneous layers. On the other hand, the heterostructure of stacked different layers produces extraordinary properties far beyond individual layers owing to the different interatomic interaction between stacked layers, which leads the study on the local transition to the commensurate state through the moiré structure analysis on a two-dimensional van der Waals superstructure of graphene on hBN. The moiré fringes exhibit local structural variation, suggesting that the interaction between graphene and hBN depends on the stacking configuration and twist angle between stacked graphene and hBN. The different interaction leads to the local transition to the commensurate state through the reduced crystalline mismatch by lattice stretching and twisting on the graphene lattices.

In the field of bulk layered materials in part 2, I have studied on the degradation mechanism of cathode

materials depending on the repeated electrochemical cycling and the types of electrolyte additives with developing a method of TEM specimen preparation. Deficient lithium in the outermost regions of cathode materials provokes the cation mixing during the delithiation, which is serious at initial cycling. The induced stoichiometric instability changes manganese's oxidation states significantly despite its low proportion in comparison with nickel. In addition, the electrolyte additives make a huge difference in structural deterioration of cathode materials. In the view of the crack formation, if the fragmented agglomeration of cathode particles maintains its original structure, it should take part in electrochemical cycling and lead to better the cycling performance, when comparing non-fragmented one with thick surface layers formed by structural transformation.

To sum up, the framework provided by this thesis suggests how to apply the conventional and state-of-the-art analytic TEM techniques to the study on fundamental understanding on structural transformation and invents a method how to explore the interaction between stacked van der Waals layers, which results in intriguing properties far beyond individual layers.

CURRICULUM VITAE

PERSONAL INFORMATION

NAME	Na Yeon Kim
	Ph.D. Candidate
INSTITUTION	Atomic-Scale Electron Microscopy (ASEM) Lab
	Materials Science and Engineering, UNIST (Ulsan
	National Institute of Science and Technology)
ADDRESS	UNIST, 44919, Ulsan, S. Korea
PHONE	+82-52-217-2390
MOBILE	+82-10-4029-9068
EMAIL	nayeon418@unist.ac.kr, nayeon418@gmail.com
Google Scholar	https://scholar.google.co.kr/citations?hl=ko&user=LG0P7kcAAAAJ
ResearchGate	https://www.researchgate.net/profile/Na_Yeon_Kim

RESEARCH INTEREST

<u>Study on Atomic Structure and Interatomic Interaction of Layered Materials Using Aberration-corrected Advanced Transmission Electron Microscopy (TEM/STEM)</u>

- Graphene & Functionalized Graphene-based Two-dimensional (2D) Materials

- Superstructure Analysis of 2D Heterostructures

- Microstructural Degradation Mechanism on Ni-rich Layered Cathode Materials in Lithium Ion Batteries

- Spectroscopic Analysis of Electron Energy Loss Spectroscopy (EELS)

- Aberration-corrected Scanning and Transmission Electron Microscopy for Atomic Resolution Imaging Analysis

RESERCH OBJECTIVE

I am interested in scientific investigation of local structural transition of the layered materials with aberration-corrected transmission electron microscopy (TEM). The structural transition by inter-atomic interaction influences material's property significantly, but, it is localized at the very few regions, which make it difficult to confirm correlation with its peculiar property. I have investigated the degree of the local structural transition such as lattice distortion by using dark-field TEM and atomic resolution TEM imaging analysis and transition of chemical states with spectroscopic analysis of EELS.

EDUCATION

Combined M.S. & Ph.D. Course	Materials Science and Engineering, UNIST
2013 ~ Present	*[Advisor: Prof. Zonghoon Lee]*
B.S.	Materials Science Engineering & Energy Conversion and
2009-2013	Storage (Multi-disciplinary Major), UNIST

RESEARCH EXPERIENCE

March 2013 - Present	**Ph.D. Candidate** in Materials Science and Engineering, UNIST • Study and training on aberration-corrected TEM/STEM • Comprehensive EELS analysis • Investigation of stacking configuration and atomic structures with defects in graphene-based materials • Moiré superstructure analysis on 2D heterostructures of graphene on hexagonal boron nitride (hBN) for transition to commensurate state • Analysis on the microstructural degradation mechanism of Ni-rich NCM cathode materials in LIB • Development of graphene synthesis by chemical vapor deposition (CVD) with inductively coupled plasma
June 2018 - Present	**Student Research Assistant** Project: Charge transport and nano phase-transform characterization of materials for energy generation and storage Nano. Material technology development project in Korea Ministry of Science and ICT • Microstructural degradation at the interfaces of NCM cathode materials depending on the additives in the electrolyte • Mechanism of cracks and pores
June 2015 - Present	**Student Research Assistant** Project: Design, Synthesis, and Characterization of New Carbon Allotropes IBS Center for Multidimensional Carbon Materials • Structural analysis of carbon materials with spectroscopic analysis using advanced TEM/STEM
June 2012 – May 2015	**Student Research Assistant** Project: Technology development for life improvement of high Ni composition cathode at high temperature (>60 °C) IT R&D Program of MKE/KEIT (No. 10041856) • Investigation on the microstructures of Ni-rich NCM cathode materials with TEM/STEM
October 2011 - February 2013	**Undergraduate Research Internship** in Materials Science and Engineering, UNIST [*Advisor: Prof. Zonghoon Lee*] • Graphene synthesis by CVD and transfer • Study and training on TEM/STEM • Development on TEM specimen preparation using focused ion beam (FIB) • Analysis on the Ni-rich NCM cathode materials in LIB

TEACHING EXPERIENCE

2rd quarter 2013	**Teaching assistant** in Materials Science and Engineering, UNIST Course title: Introduction of Crystallography • Prepared course materials for classes of approximately 100 students • Held office hours and provided support for classes • Graded assignments, examinations, and participation
3rd quarter 2013	**Teaching assistant** in Materials Science and Engineering, UNIST Course title: Introduction of Transmission Electron Microscopy • Prepared lectures and class activities • Graded assignments and examinations

PROFESSIONAL TRAINING

March 2014	**Korean EELS and EFTEM Analysis Training School 2014** by Gatan, Inc. • Fundamental principles of EELS/EFTEM • Analysis guide and practical techniques for EELS/EFTEM using DigitalMicrograph
February 2014	**Titan Materials Science Course of FEI Academy** by FEI, Eindhoven, The Netherlands • Training on an image/probe corrector with a monochromator system • Graphene high resolution TEM/STEM imaging analysis • Atomic resolution mapping with EELS/EDX
August 2013	**20th Korean TEM Workshop** by Korean Society of Microscopy • Fundamentals of TEM/STEM • Preparation of TEM specimen • Principles of electron diffraction pattern • High resolution imaging analysis • Basic of spectroscopic analysis of EELS/EDS

PROFESSIONAL SKILLS & EQUIPMENTS

Synthesis	• CVD with inductively coupled plasma : Synthesis of monolayer graphene : Plasma treatment for manipulating the graphene's properties • Mechanical exfoliation for thinning of 2D materials
Characterization Tools	• Raman Spectroscopy [*alpha 300R, WITec*] : Characterization of graphene • Cold FE-SEM [*S-4800, Hitach High-Technologies*] : Material surface characterization
Specimen Preparation	• Dual-beam FIB [*Quanta 3D FEG, FEI*] : Proficient in cross-sectioning • Precision etching and coating system [*Gatan 682, Gatan, Inc*]
TEM/STEM	• **Probe-corrected field transmission emission microscope** [*JEM-2100F, JEOL*] with EELS system [*Enfina, Gatan, Inc.*] : Experienced in high-resolution TEM/STEM imaging analysis : Proficient in EELS to investigate the chemical states and quantification of transition metals at the core loss region • **Titan equipped with Cs image & probe – correctors with an electron monochromator** [*Titan (3) G2 cube 60-300, FEI*] with Dual EELS system [*GIF Quantum 965, Gatan, Inc.*] : Competent to image 2D materials on atomic scale resolution : Experienced in dark-field TEM analysis for interlayer stacking structures and defects such as grain boundaries and wrinkles for 2D materials : Proficient in EELS to investigate the crystallinity and bonding states of carbon-based materials at the core/low loss regions
Simulation Tools	• VESTA with Jmol • CrystalMaker : Making a crystal model and simulating electron diffraction patterns for the structural transition • MactempasX : Simulation for atomic-resolution TEM/STEM imaging analysis

AWARDS

2018   *Excellent Poster Award*

"Local Lattice Match for Commensurate State of Graphene/h-BN van der Waals Heterostructure with TEM Analysis"

The 5th Korean Graphene Symposium, Buyeo, S. Korea

2017   *Excellent Poster Award*

"Distribution of Superlattice Domains in Stacked Graphene on hBN"

The 4th Korean Graphene Symposium, Buyeo, S. Korea

2015   *Best Image in Art in Science*

"Bilayer Graphene TEM World"

2015 IBS Research Conference, Ulsan, S. Korea.

2012   *Best Paper Award*

"Atomic Resolution Imaging of Rotated Bilayer Graphene Sheets using a Low kV Aberration-corrected TEM"

Korean Society of Microscopy, S. Korea

PUBLICATIONS   *[* equally contributed]*

PEER-REVIEWED JOURNAL ARTICLES

<u>- Two-dimensional Carbon-based Materials -</u>

- ■   H. Hong*, **N.Y. Kim***, A. Yoon, S. W. Lee, J. Park, J. Yoo, Z. Lee, "Synthesis of High-Quality Monolayer Graphene by Low-Power Plasma" *Curr. Appl. Phys*., 19(1), 44-49, 2019. <u>(IF: 2.058)</u>

- ■   **N.Y. Kim**, H.Y. Jeong, J.H. Kim, G. Kim, H.S. Shin and Z. Lee, "Evidence of Local Commensurate State with Lattice Match of Graphene on Hexagonal Boron Nitride" *ACS Nano*, 11(7), 7084-7090, 2017. <u>(IF: 13.709 Times Cited: 1 in Web of Science)</u>

- ■   B. Wang, B. V. Cunning, **N.Y. Kim**, S.Y. Park, Z. Li, L. Peng, V. Modepalli, X. Chen, Y. Shen, W.K. Seong, Y. Kwon, J. Jang, T. Kim, H. Shi, C. Gao, A.J. Minnich, T.J. Shin, K. Kim, J,.Y. Kim, Z. Lee and R.S. Ruoff, "Ultra-stiff and strong centimeter-scale synthetic crystals of 100 graphene layers" *Submitted*.

- ■   J. Kwak, S.Y. Kim, Y. Jo, **N.Y. Kim**, S.Y. Kim, Z. Lee and S.Y. Kwon, "Unraveling the water impermeability discrepancy in CVD-grown graphene" *Advanced Materials*, 30, 1800022, 2018. (IF = 21.950)

- ■   X. Chen, X. Deng, **N.Y. Kim**, Y. Wang, Y. Huang, L. Peng, M. Huang, X. Zhang, X. Chen, D. Luo, B. Wang, X. Wu, Y. Ma, Z. Lee and R. S. Ruoff, "Graphitization of graphene oxide films under pressure" *Carbon*, 132, 294-303, 2018. (IF: 7.082)

- ■   J. Kwak, Y. Jo, S. D. Park, **N.Y. Kim**, S.Y. Kim, H.J. Shin, Z. Lee, S.Y. Kim and S.Y. Kwon, "Oxidation behavior of graphene-coated copper at intrinsic graphene defects of different origins" *Nature communications*, 8(1), 1549, 2017. (IF: 12.353)

- ■   B. Wang, M. Huang, **N.Y. Kim**, B.V. Cunning, Y. Huang, D. Qu, X. Chen, S. Jin, M. Biswal, X. Zhang, S.H. Lee, H. Lim, J. Yoo, Z. Lee and R.S. Ruoff, "Controlled Folding of Single Crystal Graphene" *Nano Letters*, 17(3), 1467-1473, 2017. (IF: 12.080)

- H. Hong*, J. Jo*, D. Hwang, J. Lee, **N.Y. Kim**, S. Son, J.H. Kim, M.J. Jin, Y.C. Jun, R. Erni, S. K. Kwak, J.W. Yoo and Z. Lee, "Atomic Scale Study on Growth and Heteroepitaxy of ZnO Monolayer on Graphene" *Nano Letters*, 17(1), 120-127, 2017. (IF: 12.080)

- D.W. Jeong*, G.H. Kim*, **N.Y. Kim**, Z. Lee, S.D. Jung and J.O. Lee, "A high-performance transparent graphene/vertically aligned carbon nanotube (VACNT) hybrid electrode for neural interfacing" *RSC Advances*, 7(6), 3273-3281, 2017. (IF:2.936)

- X. Zhang, Y. Huang, S. Chen, **N.Y. Kim**, W. Kim, D. Schilter, M. Biswal, B. Li, Z. Lee, S. Ryu, C.W. Bielawski, W.S. Bacsa and R.S. Ruoff, "Birch-Type Hydrogenation of Few-Layer Graphenes: Products and Mechanistic Implications" *Journal of the American Chemical Society*, 138, 14980-14986, 2016. (IF: 14.357)

- S. Wu, G. Chen, **N.Y. Kim**, K. Ni, W. Zeng, Y. Zhao, Z. Tao, H. Jia, Z. Lee and Y. Zhu, "Creating Pores on Graphene Platelets by Low-Temperature KOH Activation for Enhanced Electrochemical Performance" *Small*, 12, 2376-84, 2016. (IF: 9.598)

  - Listed in Hot Topics - carbon section by Wiley-VCH publisher

- G.H. Ryu, J. Lee, **N.Y. Kim**, Y.D. Lee, Y. Kim, M.J. Kim, C. Lee and Z. Lee, "Line-defect mediated formation of hole and Mo clusters in monolayer molybdenum disulfide" *2D Materials*, 3(1), 014004, 2016. (IF: 7.042)

- G. Chen, Z. Zhuo, K. Ni, **N.Y. Kim**, Y. Zhao, Z. Chen, B. Xiang, L. Yang, Q. Zhang, Z. Lee, X. Wu, R.S. Ruoff and Y. Zhu, " Rupturing C60 molecules into graphene-oxide-like quantum dots: structure, photoluminescence and catalytic application" *Small*, 11, 5296-5304, 2015 (IF: 9.598)

- J.M. Yuk, H.Y. Jeong, **N.Y. Kim**, H.J. Park, G. Kim, H.S. Shin, R.S. Ruoff, J.Y. Lee, and Z. Lee, "Superstructural defects and superlattice domains in stacked graphene" *Carbon*, 80, 755-761, 2014 (IF: 7.082)

- G.H. Ryu, H.J. Park, **N.Y. Kim** and Z. Lee, "Atomic Resolution Imaging of Rotated Bilayer Graphene Sheets using a Low kV Aberration-corrected TEM" *Applied Microscopy*, 42(4), 218-222, 2012.

  - Selected as the Journal Cover of December 2012

- Layered Cathode Materials in LIB -

- **N.Y. Kim**, T. Yim and Z. Lee, "Impact of the Types of the Electrolyte Additives on the Microstructural Degradation of Ni-rich Cathode Materials in Lithium-ion Batteries" to be submitted.

- **N.Y. Kim**, T. Yim and Z. Lee, "A Novel Specimen Preparation for of Clean Surfaces of Porous Cathode Materials in Lithium-ion Batteries for High Resolution Transmission Electron Microscopy" to be submitted.

- **N.Y. Kim**, T. Yim, J.H. Song, J.S. Yoo and Z. Lee, " Microstructural Study on Degradation Mechanism of Layered $LiNi_{0.6}Co_{0.2}Mn_{0.2}O_2$ Cathode Materials during Cycling by High Resolution TEM/STEM" *Journal of Power Sources*, 307, 641-648, 2016 (IF: 6.945, Times Cited: 34 in Web of Science)

-

PATENT

Z. Lee, **N.Y. Kim**, 투과전자현미경용 시편 제작방법 및 장치 (Method and apparatus for producing samples for transmission electron microscopy), Korea Patent No.101494334, October 14, 2013. (PCT)

CONFERENCE ABSTRACTS

- **N.Y. Kim**, J.H. Kim, Z. Lee, "Local Lattice Match for Commensurate State of Graphene/h-BN van der Waals Heterostructure with TEM Analysis", *Microscopy & Microanalysis 2018*, August 5-9, 2018, Baltimore, MD, USA.

- **N.Y. Kim**, Z. Lee, "Microstructural Investigation on Degradation Mechanism of Layered $LiNi_{0.6}Co_{0.2}Mn_{0.2}O_2$ Cathode Materials by Analytical TEM/STEM", *Microscopy & Microanalysis 2016*, 15, July 25-28, 2016, Columbus, OH, USA, pp.1366-1367.

- **N.Y. Kim**, G.H. Ryu, H.J. Park, Z. Lee, "An Improved Specimen Preparation of Porous Powder Materials for Transmission Electron Microscopy", *Microscopy & Microanalysis 2014*, 15, August 3-7, 2014, Hartford, CT, USA, pp.366-367.

- H. Hong, J. Lee, **N.Y. Kim**, S. Son, J.H. Kim, R. Erni, Z. Lee, " Epitaxial Growth of ZnO Monolayer on Graphene: The Thinnest Metal Oxide Semiconductor", *Microscopy & Microanalysis 2017*, August 6-10, 2017, St. Louis, MO, USA, pp.1434-1435.

- G.H. Ryu, H.J. Park, J.H. Kim, **N.Y. Kim**, Z. Lee, "Characterization of Defects in 2D Materials at Atomic Scale using Aberration Corrected Transmission Electron Microscopy", *International Symposium on Microscopy & Microanalysis of Materials 2015*, November 11-14, 2015, Changwon, Korea, pp.17

- G.H. Ryu, H.J. Park, **N.Y. Kim**, J.H. Kim, K. Kim, M.J. Lee, S.W. Son, H. Hong, Z. Lee, "Investigation of stacking structure and defects of bilayer graphene using aberration corrected TEM", *International Conference of Surface Engineering 2013*, November 18-21, 2013, Busan, Korea.

- J.M. Yuk, H.Y. Jeong, **N.Y. Kim**, M.J. Lee, J.Y. Lee, Z. Lee, "Direct Mapping of Stacking Structure in Rotated Bilayer Graphene Using Aberration-corrected Transmission Electron Microscopy", *Microscopy & Microanalysis 2013*, August 4-8, 2013, Indianapolis, IN, USA, pp.1226-1227.

- J.M. Yuk, H.Y. Jeong, **N.Y. Kim**, M.J. Lee, J.Y. Lee, Z. Lee, "Microstructural Characterization in Rotated Double-Layer Graphene Using Transmission Electron Microscopy", *2013 Materials Research Society Spring Meeting*, April 1-5, 2013, San Francisco, CA, USA

PRESENTATIONS (including involved presentations)

- Low-dimensional Carbon-based Materials -

- **N.Y. Kim**, H.Y. Jeong, J. H. Kim, G. Kim, H. S. Shin, Z. Lee, "Local Lattice Match for Commensurate State Transition of Graphene/hBN van der Waals Heterostructure", The 5th International Conference on Electronic Materials and nanotechnology for Green Environment (ENGE 2018), 2018.11.11-14, Jeju, Korea. **(Oral)**

- **N.Y. Kim**, J.H. Kim, Z. Lee, "Local Lattice Match for Commensurate State of Graphene/h-BN van der Waals Heterostructure with TEM Analysis", Microscopy & Microanalysis 2018, 2018. 08.05-09, Baltimore, MD, USA. **(Poster)**

- **N.Y. Kim**, J. H. Kim, Z. Lee, "Evidence of Local Lattice Match for Commensurate State of Graphene/hBN van der Waals Heterostructure with TEM Analysis, 춘계현미경학회, 2018.06.20-22, Jeju, Korea. **(Poster)**

- **N.Y. Kim**, H.Y. Jeong, J. H. Kim, G. Kim, H. S. Shin, Z. Lee, "Evidence of local lattice match of graphene on hexagonal boron nitride", The 10th International Conference on Advanced Materials and Devices, 2017.12.05-08, Jeju, Korea. **(Poster)**

- **N.Y. Kim**, J. H. Kim, Z. Lee, "Evidence of Local Lattice Match for Commensurate State of Graphene on Hexagonal Boron Nitride, The 3rd East-Asia Microscopy Conference, 2017.11.07-10, Busan, Korea. **(Oral)**

- H. Hong, J. Lee, **N.Y. Kim**, S. Son, J. H. Kim, R. Erni, Z. Lee, "Atomic Scale Study on Growth and Heteroepitaxy of ZnO Monolayer on Graphene", The 3rd East-Asia Microscopy Conference, 2017.11.07-10, Busan, Korea.

- Y. Lee, H. S. Kim, J. Lee, S. Ramzan, S. Son, J. H. Kim, **N.Y. Kim**, Y. Kim, and Z. Lee, "Surface Oxidation of Atomically Thin MoS2 by UVO treatment", The 3rd East-Asia Microscopy Conference, 2017.11.07-10, Busan, Korea.

- H. Hong, J. Lee, **N.Y. Kim**, S. Son, J. H. Kim, R. Erni, Z. Lee, "Atomic Scale Study on Growth and Heteroepitaxy of ZnO Monolayer on Graphene", European Microbeam Analysis Society & International Union of Microbeam Analysis Societies, 2017.05.07-11, Konstanz, Germany.

- **N.Y. Kim**, J. H. Kim, Z. Lee, "Distribution of superlattice domains in stacked graphene on hBN", 4th Korea graphene symposium, 2017.04.06-07, Buyeo, Korea. **(Poster)**

- Y.D. Lee, S. Son, J.H. Kim, **N.Y. Kim**, Z. Lee, "Surface Oxidation of Atomically Thin MoS2 by UVO treatment", 4th Korea graphene symposium, 2017.04.06-07, Buyeo, Korea.

- H. Hong, J. Jo, D. Hwang, J. Lee, **N.Y. Kim**, S. Son, J. H. Kim, M. Jin, Y. C. Jun, R. Erni, S. K. Kwak, J.W. Yoo, Z. Lee, "Epitaxial Grown Monolayer ZnO on Grapehene", International Symposium on microscopy and microanalysis of materials, 2016.09.23-26, Nanjing, China.

- **N.Y. Kim**, G. Chen, S. Wu, R.S. Ruoff, Y. Zhu, Z. Lee, "Microtructural investigation of functionalized graphene oxides materials with advanced TEM", 8th International Conference on Recent Progress in Graphene/2D Research, 2016.08.25-29, Seoul, Korea. **(Poster)**

- G.H. Ryu, J. Lee, **N.Y. Kim**, Y. Lee, Z. Lee, "Line-defect mediated formation of hole and Mo clusters in single layer molybdenum disulfide", 8th International Conference on Recent Progress in Graphene/2D Research, 2016.08.25-29, Seoul, Korea.

- X. Zhang, Y. Huang, S. Chen, **N.Y. Kim**, W. Kim, D. Schilter, M. Biswal, B. Li, Z. Lee, S. Ryu, C.W. Bielawski, W.S. Bacsa, R.S. Ruoff, "Birch-Type Hydrogenation of Few-Layer Graphenes: Products and Mechanistic Implications", Korean Chemical Society fall meeting, 2016.08.12-14, Busan, Korea.

- **N.Y. Kim**, G. Chen, S. Wu, R.S. Ruoff, Y. Zhu, Z. Lee, "Structural investigation of functionalized graphene oxides – based materials with advanced TEM", 47 차 춘계현미경학회, 2016.06.02-03, Gumi, Korea. **(Poster)**

- H. Hong, J. Jo, D. Hwang, J. Lee, **N.Y. Kim**, S. Son, J. H. Kim, M. Jin, Y. C. Jun, R. Erni, S.K. Kwak, J.W. Yoo, Z. Lee, "Epitaxially Grown Single-atom-thick Layer of ZnO on Graphene", 47 차 춘계현미경학회, 2016.06.02-03, Gumi, Korea.

- G.H. Ryu, J. Lee, **N.Y. Kim**, Y. Lee, Z. Lee, "Line-defect mediated formation of hole and Mo clusters in single layer molybdenum disulfide", 47 차 춘계현미경학회, 2016.06.02-03, Gumi, Korea.

- **N.Y. Kim**, G. Chen, S. Wu, R.S. Ruoff, Y. Zhu, Z. Lee, "Microstructural investigation of functionalized graphene oxides materials with advanced TEM", 3th Korea graphene symposium, 2016.04.14-15, Buyeo, Korea. **(Poster)**

- G.H. Ryu, J. Lee, **N.Y. Kim**, Y. Lee, Z. Lee, "Line-defect mediated formation of hole and Mo clusters in single layer molybdenum disulfide", 3th Korea graphene symposium, 2016.04.14-15, Buyeo, Korea.

- H. Hong, J. Jo, D. Hwang, J. Lee, **N.Y. Kim**, S. Son, J. H. Kim, M. Jin, Y. C. Jun, R. Erni, S. K. Kwak, J.W. Yoo, Z. Lee, "Epitaxially Grown Monolayer ZnO on Graphene", 3th Korea graphene symposium, 2016.04.14-15, Buyeo, Korea.

- G. H. Ryu, H. J. Park, J. H. Kim, **N.Y. Kim**, Z. Lee, "Characterization of Defects in 2D Materials at Atomic Scale using Aberration Corrected Transmission Electron Microscopy", International Symposium on Microscopy & Microanalysis of Materials 2015, 2015.11-14, 2015, Changwon, Korea.

- G. H. Ryu, H. J. Park, J. H. Kim, **N. Y. Kim**, Z. Lee, "Characterization of Defects in 2D Materials at Atomic Scale using Aberration Corrected Transmission Electron Microscopy", Dasan Conference, 2015.11.02-04, Jeju, Korea.

- G.H. Ryu, H.J. Park, **N.Y. Kim**, J.H. Kim, H.K. Hong, Z. Lee, "Atomic-scale Research on 2D Materials using Aberration-corrected TEM", 2015 Collaborative Conference on 3D and Materials Research, 2015.06.15-19, Jeju, Korea.

- X. Zhang, B. Li, M. Biswal, **N.Y. Kim**, X. Chen, Z. Lee, S. Chen, C.W. Bielawski, R.S. Ruoff, "Hydrogenation of Single- and Few-Layer Graphene through Birch-type Reduction", International Conference on New Diamond and Nano Carbons, 2015.05.24-28, Shizuoka, Japan.

- G.H. Ryu, H.J. Park, **N.Y. Kim**, J.H. Kim, K. Kim, M.J. Lee, Z. Lee, " Investigation of stacking structure and defects of bilayer graphene using aberration corrected TEM", International Conference of Surface Engineering 2013, 2013.11.18-21, Busan, Korea.

- J.M. Yuk, H.Y. Jeong, **N.Y. Kim**, M.J. Lee, J.Y. Lee, Z. Lee, "Direct Mapping of Stacking Structure in Rotated Bilayer Graphene Using Aberration-corrected Transmission Electron Microscopy", Microscopy & Microanalysis 2013, 2013.08.04-08, Indianapolis, USA.

- Layered Cathode Materials in LIB -

- **N.Y. Kim**, Z. Lee, "Degradation Mechanism of Layered $LiNi_{0.6}Co_{0.2}Mn_{0.2}O_2$ During Early Electrochemical Cycling by Analytical TEM and STEM", The 3rd East-Asia Microscopy Conference, 2017.11.07-10, Busan, Korea. **(Poster)**

- **N.Y. Kim**, Z. Lee, "Microstructural Investigation on Degradation Mechanism of Layered $LiNi_{0.6}Co_{0.2}Mn_{0.2}O_2$ Cathode Materials by Analytical TEM/STEM", Microscopy & Microanalysis 2016, 15, 2016.07.25-28, Columbus, USA. **(Poster)**

- **N.Y. Kim**, Z. Lee, "Microstructural Investigation of a Degradation Mechanism in Layered Cathode Materials for Lithium Ion Batteries with HRTEM and HRSTEM", 46 차 춘계현미경학회, 2015.05.28-29, Seoul, Korea. **(Oral)**

- **N.Y. Kim**, Z. Lee, "An innovative Specimen Preparation of Porous Powder Materials for Transmission Electron Microscopy", 45 차 추계현미경학회, 2014.11.13-14, Seoul, Korea. **(Poster)**

- **N.Y. Kim**, G.H. Ryu, H.J. Park, Z. Lee, "An Improved Specimen Preparation of Porous Powder Materials for Transmission Electron Microscopy", Microscopy & Microanalysis 2014, 2014.08.03-07, Hartford, USA. **(Poster)**

REFERENCES

1. Mokaya, R. Ion Exchange | Novel Layered Materials: Non-Phosphates; In *Encyclopedia of Separation Science*, Wilson, I. D., Ed. Academic Press: Oxford, **2000**; pp 1610-1617.

2. McKinney, Robert W.*, et al.* Ionic Vs. Van Der Waals Layered Materials: Identification and Comparison of Elastic Anisotropy. *J. Mater. Chem. A* **2018**, *6*, 15828-15838

3. Van Tendeloo, G.*, et al.* Advanced Electron Microscopy for Advanced Materials. *Adv. Mater.* **2012**, *24*, 5655-5675

4. Muller, D. A. Structure and Bonding at the Atomic Scale by Scanning Transmission Electron Microscopy. *Nat. Mater.* **2009**, *8*, 263-270

5. Kimoto, K. Practical Aspects of Monochromators Developed for Transmission Electron Microscopy. *Microscopy (Oxf)* **2014**, *63*, 337-344

6. Klein, N. D.*, et al.* Dark Field Transmission Electron Microscopy as a Tool for Identifying Inorganic Nanoparticles in Biological Matrices. *Anal Chem* **2015**, *87*, 4356-4362

7. Brown, L.*, et al.* Twinning and Twisting of Tri- and Bilayer Graphene. *Nano Lett.* **2012**, *12*, 1609-1615

8. Föll, H. Basics of Tem and the Contrast of Dislocations. https://www.tf.uni-kiel.de/matwis/amat/def_en/kap_6/backbone/r6_3_1.html.

9. Wang, Z. L. Dislocation Contrast in High-Angle Hollow-Cone Dark-Field Tem. *Ultramicroscopy* **1994**, *53*, 73-90

10. Smith, D. J. Progress & Perspectives for Atomic-Resolution Electron Microscopy. *Materials Today* **2010**, *12*, 10-16

11. Egerton, R. F. An Introduction to Eels; In *Electron Energy-Loss Spectroscopy in the Electron Microscope*, Springer US: Boston, MA, **2011**; pp 1-28.

12. Electron Energy Loss Spectrometry and Energy Dispersive X-Ray Analysis; In *Aberration Corrected Analytical Transmission Electron Microscopy*.

13. *Aberration-Corrected Analytical Transmission Electron Microscopy*; John Wiley & Sons, Ltd, **2011**.

14. Williams, D. B.; Carter, C. B. *Transmission Electron Microscopy*; 2 ed., Springer US, New York, **2009**.

15. Krueger, A. Carbon – Element of Many Faces; In *Carbon Materials and Nanotechnology*, Wiley-VCH: Weinheim, **2010**.

16. Schäffel, F. Chapter 2 - the Atomic Structure of Graphene and Its Few-Layer Counterparts; In *Graphene*, Warner, J. H.; Schäffel, F.; Bachmatiuk, A.; Rümmeli, M. H., Eds. Elsevier: **2013**; pp 5-59.

17. Castro Neto, A. H.*, et al.* The Electronic Properties of Graphene. *Reviews of Modern Physics* **2009**, *81*, 109-162

18. Bodenmann, A. K.; MacDonald, A. H. Graphene: Exploring Carbon Flatland. *Physics Today* **2007**, *60*, 35-41

19. Lee, J. K.*, et al.* The Nature of Metastable Aa' Graphite: Low Dimensional Nano- and Single-Crystalline Forms. *Sci. Rep.* **2016**, *6*, 39624

20. Nguyen, V. L.; Lee, Y. H. Towards Wafer-Scale Monocrystalline Graphene Growth and Characterization. *Small* **2015**, *11*, 3512-3528

21. Regan, W.*, et al.* A Direct Transfer of Layer-Area Graphene. *Appl. Phys. Lett.* **2010**, *96*, 113102

22. Daniels, H.*, et al.* Investigating Carbonization and Graphitization Using Electron Energy Loss Spectroscopy (Eels) in the Transmission Electron Microscope (Tem). *Philosophical Magazine* **2007**, *87*, 4073-4092

23. Inagaki, M.; Kang, F. Chapter 2 - Fundamental Science of Carbon Materials; In *Materials Science and Engineering of Carbon: Fundamentals (Second Edition)*, Butterworth-Heinemann: Oxford, **2014**; pp 17-217.

24. Chen, X.*, et al.* Graphitization of Graphene Oxide Films under Pressure. *Carbon* **2018**, *132*, 294-303

25.   Şahin, H*., et al.* Structures of Fluorinated Graphene and Their Signatures. *Phys. Rev. B: Condens. Matter Mater. Phys.* **2011**, *83*, 115432

26.   Mkhoyan, K. A*., et al.* Atomic and Electronic Structure of Graphene-Oxide. *Nano Lett.* **2009**, *9*, 1058-1063

27.   Johns, J. E.; Hersam, M. C. Atomic Covalent Functionalization of Graphene. *Acc. Chem. Res.* **2012**, *46*, 77-86

28.   Qi, Z. J*., et al.* Correlating Atomic Structure and Transport in Suspended Graphene Nanoribbons. *Nano Lett.* **2014**,

29.   Nair, R. R*., et al.* Fluorographene: A Two-Dimensional Counterpart of Teflon. *Small* **2010**, *6*, 2877-2884

30.   Pumera, M.; Wong, C. H. Graphane and Hydrogenated Graphene. *Chemical Society reviews* **2013**, *42*, 5987-5995

31.   Sofo, J*., et al.* Graphane: A Two-Dimensional Hydrocarbon. *Phys. Rev. B: Condens. Matter Mater. Phys.* **2007**, *75*,

32.   Son, J*., et al.* Hydrogenated Monolayer Graphene with Reversible and Tunable Wide Band Gap and Its Field-Effect Transistor. *Nat. Commun.* **2016**, *7*, 13261

33.   Sofo, J. O*., et al.* Graphane: A Two-Dimensional Hydrocarbon. *Phys. Rev. B* **2007**, *75*, 153401

34.   Boukhvalov, D. W*., et al.* Hydrogen on Graphene: Electronic Structure, Total Energy, Structural Distortions and Magnetism from First-Principles Calculations. *Phys. Rev. B* **2008**, *77*, 035427

35.   Zhang, X*., et al.* Birch-Type Hydrogenation of Few-Layer Graphenes: Products and Mechanistic Implications. *J. Am. Chem. Soc.* **2016**, *138*, 14980-14986

36.   Li, Y. F*., et al.* Surface Hydrogenation Regulated Wrinkling and Torque Capability of Hydrogenated Graphene Annulus under Circular Shearing. *Sci. Rep.* **2015**, *5*, 16556

37.   Bangert, U*., et al.* Structure of Hydrogen-Dosed Graphene Deduced from Low Electron Energy Loss Characteristics and Density Functional Calculations. *Appl. Phys. Lett.* **2010**, *97*, 253118

38.   Nelson, F. J*., et al.* Electronic Excitations in Graphene in the 1–50 Ev Range: The Π and $\Pi + \Sigma$ Peaks Are Not Plasmons. *Nano Lett.* **2014**, *14*, 3827-3831

39.   Kapetanakis, M. D*., et al.* Low-Loss Electron Energy Loss Spectroscopy: An Atomic-Resolution Complement to Optical Spectroscopies and Application to Graphene. *Phys. Rev. B: Condens. Matter Mater. Phys.* **2015**, *92*, 125147

40.   Carbone, F*., et al.* Dynamics of Chemical Bonding Mapped by Energy-Resolved 4d Electron Microscopy. *Science* **2009**, *325*, 181-184

41.   Nejati, H.; Dadsetani, M. Electron Energy Loss Spectrum of Graphane from First-Principles Calculations. *Micron* **2014**, *67*, 30-36

42.   Eberlein, T*., et al.* Plasmon Spectroscopy of Free-Standing Graphene Films. *Phys. Rev. B: Condens. Matter Mater. Phys.* **2008**, *77*,

43.   Kushita, K. N.; Hojou, K. In Situ Eels Observation of Graphite Structure Modification Due to Hydrogen Ion Irradiation. *Ultramicroscopy* **1991**, *35*, 289-293

44.   Bernier, N*., et al.* A Methodology to Optimize the Quantification of Sp2 Carbon Fraction from K Edge Eels Spectra. *J. Electron. Spectrosc. Relat. Phenom.* **2008**, *164*, 34-43

45.   Geim, A. K.; Grigorieva, I. V. Van Der Waals Heterostructures. *Nature* **2013**, *499*, 419-425

46.   Dean, C. R*., et al.* Boron Nitride Substrates for High-Quality Graphene Electronics. *Nat. Nanotechnol.* **2010**, *5*, 722-726

47.   Xue, J*., et al.* Scanning Tunnelling Microscopy and Spectroscopy of Ultra-Flat Graphene on Hexagonal Boron Nitride. *Nat. Mater.* **2011**, *10*, 282-285

48.   Brar, V. W*., et al.* Hybrid Surface-Phonon-Plasmon Polariton Modes in Graphene/Monolayer H-Bn Heterostructures. *Nano Lett.* **2014**, *14*, 3876-3880

49.   Yan, Z*., et al.* Phonon Transport at the Interfaces of Vertically Stacked Graphene and Hexagonal Boron Nitride Heterostructures. *Nanoscale* **2016**, *8*, 4037-4046

50.   Yan, Z*., et al.* Heterostructural Bilayers of Graphene and Molybdenum Disulfide: Configuration Types, Band Opening and Enhanced Light Response. *Superlattices Microstruct.* **2014**, *68*, 56-65

51. Azizi, A*., et al.* Freestanding Van Der Waals Heterostructures of Graphene and Transition Metal Dichalcogenides. *ACS Nano* **2015**, *9*, 4882-4890

52. Aubry, S. The Twist Map, the Extended Frenkel-Kontorova Model and the Devil's Staircase. *Physica D* **1983**, *7*, 240-258

53. Braun, O. M.; Kivshar, Y. S. *The Frenkel-Kontorova Model: Concepts, Methods, and Applications*; Springer, **2004**.

54. Sakai, Y*., et al.* Electronic Structure and Stability of Layered Superlattice Composed of Graphene and Boron Nitride Monolayer. *Phys. Rev. B: Condens. Matter Mater. Phys.* **2011**, *83*, 205434

55. Neek-Amal, M.; Peeters, F. M. Graphene on Hexagonal Lattice Substrate: Stress and Pseudo-Magnetic Field. *Appl. Phys. Lett.* **2014**, *104*, 173106

56. Tang, S*., et al.* Precisely Aligned Graphene Grown on Hexagonal Boron Nitride by Catalyst Free Chemical Vapor Deposition. *Sci. Rep.* **2013**, *3*, 2666

57. Neek-Amal, M.; Peeters, F. M. Graphene on Boron-Nitride: Moiré Pattern in the Van Der Waals Energy. *Appl. Phys. Lett.* **2014**, *104*, 041909

58. Sachs, B*., et al.* Adhesion and Electronic Structure of Graphene on Hexagonal Boron Nitride Substrates. *Phys. Rev. B: Condens. Matter Mater. Phys.* **2011**, *84*, 195414

59. Li, X*., et al.* Large-Area Synthesis of High-Quality and Uniform Graphene Films on Copper Foils. *Science* **2009**, *324*, 1312-1314

60. Kim, G*., et al.* Growth of High-Crystalline, Single-Layer Hexagonal Boron Nitride on Recyclable Platinum Foil. *Nano Lett.* **2013**, *13*, 1834-1839

61. Decker, R*., et al.* Local Electronic Properties of Graphene on a Bn Substrate *Via* Scanning Tunneling Microscopy. *Nano Lett.* **2011**, *11*, 2291-2295

62. Liao, Y*., et al.* Evolution of Moire Profiles from Van Der Waals Superstructures of Boron Nitride Nanosheets. *Sci. Rep.* **2016**, *6*, 26084

63. Warner, J. H*., et al.* Direct Imaging of Rotational Stacking Faults in Few Layer Graphene. *Nano Lett.* **2009**, *9*, 102-106

64. Miller, D. L*., et al.* Structural Analysis of Multilayer Graphene *Via* Atomic Moiré Interferometry. *Phys. Rev. B: Condens. Matter Mater. Phys.* **2010**, *81*, 125427

65. Wang, Q*., et al.* Formation of Secondary Moire Patterns for Characterization of Nanoporous Alumina Structures in Multiple Domains with Different Orientations. *Nanoscale* **2013**, *5*, 2285-2289

66. Lin, J*., et al.* Ac/Ab Stacking Boundaries in Bilayer Graphene. *Nano Lett.* **2013**, *13*, 3262-3268

67. Kim, K*., et al.* Grain Boundary Mapping in Polycrystalline Graphene. *ACS Nano* **2011**, *5*, 2142-2146

68. Tsen, A. W*., et al.* Tailoring Electrical Transport across Grain Boundaries in Polycrystalline Graphene. *Science* **2012**, *336*, 1143-1146

69. Butz, B*., et al.* Dislocations in Bilayer Graphene. *Nature* **2014**, *505*, 533-537

70. Kim, J. H*., et al.* The Hide-and-Seek of Grain Boundaries from Moire Pattern Fringe of Two-Dimensional Graphene. *Sci. Rep.* **2015**, *5*, 12508

71. Yuk, J. M*., et al.* Superstructural Defects and Superlattice Domains in Stacked Graphene. *Carbon* **2014**, *80*, 755-761

72. Ping, J.; Fuhrer, M. S. Layer Number and Stacking Sequence Imaging of Few-Layer Graphene by Transmission Electron Microscopy. *Nano Lett.* **2012**, *12*, 4635-4641

73. Kim, N. Y*., et al.* Evidence of Local Commensurate State with Lattice Match of Graphene on Hexagonal Boron Nitride. *ACS Nano* **2017**, *11*, 7084-7090

74. Hunt, B*., et al.* Massive Dirac Fermions and Hofstadter Butterfly in a Van Der Waals Heterostructure. *Science* **2013**, *340*, 1427-1430

75. Woods, C. R*., et al.* Commensurate–Incommensurate Transition in Graphene on Hexagonal Boron Nitride. *Nat. Phys.* **2014**, *10*, 451-456

76. San-Jose, P*., et al.* Spontaneous Strains and Gap in Graphene on Boron Nitride. *Phys. Rev. B: Condens. Matter Mater. Phys.* **2014**, *90*, 075428

77. Leven, I., *et al.* Interlayer Potential for Graphene/H-Bn Heterostructures. *J. Chem. Theory Comput.* **2016**, *12*, 2896-2905

78. van Wijk, M. M., *et al.* Moiré Patterns as a Probe of Interplanar Interactions for Graphene on H-Bn. *Phys. Rev. Lett.* **2014**, *113*, 135504

79. Ryu, G. H., *et al.* Atomic-Scale Dynamics of Triangular Hole Growth in Monolayer Hexagonal Boron Nitride under Electron Irradiation. *Nanoscale* **2015**, *7*, 10600-10605

80. Carter, C. B.; Williams, D. B. *Transmission Electron Microscopy: Diffraction, Imaging, and Spectrometry*; Springer International Publishing, **2016**.

81. Yankowitz, M., *et al.* Pressure-Induced Commensurate Stacking of Graphene on Boron Nitride. *Nat. Commun.* **2016**, *7*, 13168

82. Dai, S., *et al.* Twisted Bilayer Graphene: Moire with a Twist. *Nano Lett.* **2016**, *16*, 5923-5927

83. Zhao, X., *et al.* Lattice Match and Lattice Mismatch Models of Graphene on Hexagonal Boron Nitride from First Principles. *J. Phys.: Condens. Matter* **2014**, *26*, 095002

84. Sakai, Y., *et al.* Lattice Matching and Electronic Structure of Finite-Layer Graphene-Bn Thin Films. *Phys. Rev. B: Condens. Matter Mater. Phys.* **2014**, *89*, 115424

85. Fergus, J. W. Recent Developments in Cathode Materials for Lithium Ion Batteries. *J. Power Sources* **2010**, *195*, 939-954

86. Myung, S.-T., *et al.* Nickel-Rich Layered Cathode Materials for Automotive Lithium-Ion Batteries: Achievements and Perspectives. *ACS Energy Lett.* **2016**, 196-223

87. Wu, S.-L., *et al.* High Rate Capability of Li(Ni1⁄3mn1⁄3co1⁄3)O2 Electrode for Li-Ion Batteries. *J. Electrochem. Soc.* **2012**, *159*, A438

88. Vetter, J., *et al.* Ageing Mechanisms in Lithium-Ion Batteries. *J. Power Sources* **2005**, *147*, 269-281

89. Palacin, M. R.; de Guibert, A. Why Do Batteries Fail? *Science* **2016**, *351*, 1253292

90. Liao, P. Y., *et al.* Microstructure and Electrochemical Performance of Lini0.6co0.4−Xmnxo2 Cathode Materials. *J. Power Sources* **2005**, *143*, 212-218

91. Arora, P., *et al.* Capacity Fade Mechanisms and Side Reactions in Lithium-Ion Batteries. *J. Electrochem. Soc.* **1998**, *145*, 3647-3667

92. Gilbert, J. A., *et al.* Transition Metal Dissolution, Ion Migration, Electrocatalytic Reduction and Capacity Loss in Lithium-Ion Full Cells. *J. Electrochem. Soc.* **2017**, *164*, A389-A399

93. Gu, M., *et al.* Conflicting Roles of Nickel in Controlling Cathode Performance in Lithium Ion Batteries. *Nano Lett.* **2012**, *12*, 5186-5191

94. Yan, P., *et al.* Evolution of Lattice Structure and Chemical Composition of the Surface Reconstruction Layer in Li1.2ni0.2mn0.6o2 Cathode Material for Lithium Ion Batteries. *Nano Lett.* **2015**, *15*, 514-522

95. Abraham, D. P., *et al.* Surface Changes on Lini0.8co0.2o2 Particles During Testing of High-Power Lithium-Ion Cells. *Electrochem. Commun.* **2002**, *4*, 620-625

96. Sun, G., *et al.* On the Fragmentation of Active Material Secondary Particles in Lithium Ion Battery Cathodes Induced by Charge Cycling. *Extreme Mech. Lett.* **2016**, *9*, 449-458

97. Hu, Y., *et al.* Averting Cracks Caused by Insertion Reaction in Lithium–Ion Batteries. *J. Mater. Res.* **2011**, *25*, 1007-1010

98. Ates, M. N., *et al.* A High Rate Li-Rich Layered Mnc Cathode Material for Lithium-Ion Batteries. *RSC Adv.* **2015**, *5*, 27375-27386

99. Cho, Y.-H., *et al.* Thermal Stability of Charged Lini0.5co0.2mn0.3o2 Cathode for Li-Ion Batteries Investigated by Synchrotron Based in Situ X-Ray Diffraction. *J. Alloys Compd.* **2013**, *562*, 219-223

100. Armstrong, A. R., *et al.* Demonstrating Oxygen Loss and Associated Structural Reorganization in the Lithium Battery Cathode Li[Ni0.2li0.2mn0.6]O2. *J. Am. Chem. Soc.* **2006**, *128*, 8694-8698

101. Jung, S.-K., *et al.* Understanding the Degradation Mechanisms of Lini0.5co0.2mn0.3o2cathode Material in Lithium Ion Batteries. *Adv. Energy Mater.* **2014**, *4*, 1300787

102. Lin, F., *et al.* Phase Evolution for Conversion Reaction Electrodes in Lithium-Ion Batteries.

Nat. Commun. **2014**, *5*, 3358

103. Kojima, Y*., et al.* Degradation Analysis of a Ni-Based Layered Positive-Electrode Active Material Cycled at Elevated Temperatures Studied by Scanning Transmission Electron Microscopy and Electron Energy-Loss Spectroscopy. *J. Power Sources* **2011**, *196*, 7721-7727

104. Boulineau, A*., et al.* First Evidence of Manganese-Nickel Segregation and Densification Upon Cycling in Li-Rich Layered Oxides for Lithium Batteries. *Nano Lett.* **2013**, *13*, 3857-3863

105. Klepeis, S. J*., et al.* In *A Grinding/Polishing Tool for Tem Sample Preparation*, MRS Proceedings, Cambridge University Press: 2011; p 179.

106. Romano, A*., et al.* A Fast Preparation Technique for High-Quality Plan View and Cross-Section Tem Specimens of Semiconducting Materials. *Ultramicroscopy* **1989**, *31*, 183-192

107. Rao, D. S*., et al.* Tem Specimen Preparation Techniques; In *Microscopy: Science, Technology, Applications and Education*, **2010**; pp 1232-1244.

108. Mayer, J*., et al.* Tem Sample Preparation and Fib-Induced Damage. *MRS Bulletin* **2011**, *32*, 400-407

109. Giannuzzi, L. A.; Stevie, F. A. A Review of Focused Ion Beam Milling Techniques for Tem Specimen Preparation. *Micron* **1999**, *30*, 197-204

110. Munroe, P. R. The Application of Focused Ion Beam Microscopy in the Material Sciences. *Mater. Charact.* **2009**, *60*, 2-13

111. Unocic, K. A*., et al.* Effect of Gallium Focused Ion Beam Milling on Preparation of Aluminium Thin Foils. *J Microsc* **2010**, *240*, 227-238

112. Kim, N. Y*., et al.* Microstructural Study on Degradation Mechanism of Layered Lini0.6co0.2mn0.2o2 Cathode Materials by Analytical Transmission Electron Microscopy. *J. Power Sources* **2016**, *307*, 641-648

113. Gu, M*., et al.* Formation of the Spinel Phase in the Layered Composite Cathode Used in Li-Ion Batteries. *ACS Nano* **2012**, *7*, 760-767

114. Liu, W*., et al.* Nickel-Rich Layered Lithium Transition-Metal Oxide for High-Energy Lithium-Ion Batteries. *Angew. Chemi.* **2015**, *54*, 4440-4457

115. Yan, P*., et al.* Atomic-Resolution Visualization of Distinctive Chemical Mixing Behavior of Ni, Co, and Mn with Li in Layered Lithium Transition-Metal Oxide Cathode Materials. *Chem. Mater.* **2015**, *27*, 5393-5401

116. Wang, H. F*., et al.* Tem Study of Electrochemical Cycling-Induced Damage and Disorder in Licoo2 Cathodes for Rechargeable Lithium Batteries. *J. Electrochem. Soc.* **1999**, *146*, 473-480

117. Zhang, Y*., et al.* Synthesis of Lini0.6co0.2mn0.2o2 Cathode Material by a Carbonate Co-Precipitation Method and Its Electrochemical Characterization. *Solid State Ionics* **2006**, *177*, 3303-3307

118. Lin, F*., et al.* Surface Reconstruction and Chemical Evolution of Stoichiometric Layered Cathode Materials for Lithium-Ion Batteries. *Nat. Commun.* **2014**, *5*, 3529

119. Pennycook, S. J. Z-Contrast Stem for Materials Science. *Ultramicroscopy* **1989**, *30*, 58-69

120. Zheng, S*., et al.* Microstructural Changes in Lini0.8co0.15al0.05o2 Positive Electrode Material During the First Cycle. *J. Electrochem. Soc.* **2011**, *158*, A357

121. Zheng, J*., et al.* Corrosion/Fragmentation of Layered Composite Cathode and Related Capacity/Voltage Fading During Cycling Process. *Nano Lett.* **2013**, *13*, 3824-3830

122. Tan, H*., et al.* Oxidation State and Chemical Shift Investigation in Transition Metal Oxides by Eels. *Ultramicroscopy* **2012**, *116*, 24-33

123. Sparrow, T. G*., et al.* L3/L2 White-Line Intensity Ratios in the Electron Energy-Loss Spectra of 3d Transition-Metal Oxides. *Chem. Phys. Lett.* **1984**, *108*, 547-550

124. Graetz, J*., et al.* White Lines and D-Band Occupancy for the 3d Transition-Metal Oxides and Lithium Transition-Metal Oxides. *Phys. Rev. B: Condens. Matter Mater. Phys.* **2004**, *69*, 235103

125. Pearson, D. H*., et al.* White Lines and D-Electron Occupancies for the 3dand 4dtransition Metals. *Phys. Rev. B: Condens. Matter Mater. Phys.* **1993**, *47*, 8471-8478

126. van Aken, P. A.; Liebscher, B. Quantification of Ferrous/Ferric Ratios in Minerals: New

Evaluation Schemes of Fe L 23 Electron Energy-Loss near-Edge Spectra. *Phys Chem Min* **2002**, *29*, 188-200

127. Rask, J. H*., et al.* Determination of Maganese Oxidation States in Solids by Electron Energy-Loss Spectroscopy. *Ultramicroscopy* **1987**, *21*, 321-326
128. Riedl, T*., et al.* Extraction of Eels White-Line Intensities of Manganese Compounds: Methods, Accuracy, and Valence Sensitivity. *Ultramicroscopy* **2006**, *106*, 284-291
129. Paterson, J. H.; Krivanek, O. L. Elnes of 3d Transition-Metal Oxides Ii. Variations with Oxidation State and Crystal Structure. *Ultramicroscopy* **1990**, *32*, 319-325
130. Koyama, Y*., et al.* Electronic Structure of Lithium Nickel Oxides by Electron Energy Loss Spectroscopy. *J. Phys. Chem. B.* **2005**, *109*, 10749-10755
131. Gu, M*., et al.* Nanoscale Phase Separation, Cation Ordering, and Surface Chemistry in Pristine Li1.2ni0.2mn0.6o2for Li-Ion Batteries. *Chem. Mater.* **2013**, *25*, 2319-2326
132. Yoon, W.-S*., et al.* Investigation of the Charge Compensation Mechanism on the Electrochemically Li-Ion Deintercalated Li1-Xco1/3ni1/3mn1/3o2 Electrode System by Combination of Soft and Hard X-Ray Absorption Spectroscopy. *J. Am. Chem. Soc.* **2005**, *127*, 17479-17487
133. Shaju, K. M*., et al.* Performance of Layered Li(Ni1/3co1/3mn1/3)O2 as Cathode for Li-Ion Batteries. *Electrochim. Acta* **2002**, *48*, 145-151
134. Wang, Q*., et al.* A Multi-Component Additive to Improve the Thermal Stability of Li(Ni1/3co1/3mn1/3)O2-Based Lithium Ion Batteries. *Energies* **2016**, *9*, 424
135. Li, J*., et al.* The Impact of Electrolyte Additives and Upper Cut-Off Voltage on the Formation of a Rocksalt Surface Layer in Lini 0.8 Mn 0.1 Co 0.1 O 2 Electrodes. *J. Electrochem. Soc.* **2017**, *164*, A655-A665
136. Haregewoin, A. M*., et al.* Electrolyte Additives for Lithium Ion Battery Electrodes: Progress and Perspectives. *Energy Environ. Sci.* **2016**, *9*, 1955-1988
137. Kang, K. S*., et al.* Effect of Additives on Electrochemical Performance of Lithium Nickel Cobalt Manganese Oxide at High Temperature. *J. Power Sources* **2014**, *253*, 48-54
138. Song, B*., et al.* Nano-Structural Changes in Li-Ion Battery Cathodes During Cycling Revealed by Fib-Sem Serial Sectioning Tomography. *J. Mater. Chem. A* **2015**, *3*, 18171-18179
139. Yan, P*., et al.* Intragranular Cracking as a Critical Barrier for High-Voltage Usage of Layer-Structured Cathode for Lithium-Ion Batteries. *Nat. Commun.* **2017**, *8*, 14101
140. Wang, D*., et al.* Cracking Causing Cyclic Instability of Lifepo4 Cathode Material. *J. Power Sources* **2005**, *140*, 125-128